DOE/ID/13363-3

Relationship between Casting Distortion, Mold Filling, and Interfacial Heat Transfer

K.A. Woodbury, J.K. Parker and T.S. Piwonka
Metal Casting Technology Center
The University of Alabama

Y. Owusu
Florida A&M University/Florida State University
Tallahassee, FL

Annual Technical Report
September 1997 – September 1998

Cooperative Agreement DE-FC07-95ID13363

October 22, 1998

Metal Casting Technology Center
The University of Alabama
Tuscaloosa, AL 35487-0201

DISCLAIMER

Table of Contents

continued Table of Contents

Executive Summary

In the third year of this program, the final castings necessary to evaluate the effect of casting orientation and gating in silica sand lost foam were poured and measured using a CMM machine. Interfacial heat transfer and gap formation measurements continued. However, significant problems were encountered in making accurate measurements. No consistent evidence of gap formation was found in aluminum sand casting. Initial analysis yields heat transfer values below those previously reported in the literature. The program is continuing.

1.0 Introduction

Dimensional accuracy in metal castings has taken on increased importance in the last decade, as methods of controlling cast structure have improved. There is an emphasis on molding accuracy, and, today, on understanding the way alloy solidification affects casting accuracy.

At the same time, the use of solidification simulation programs is expanding rapidly in the metalcasting industry. Well over half of the castings produced in the United States are produced in foundries that routinely use commercial solidification simulation programs today. As the use of these programs has proliferated, there has been an increased emphasis in making them as accurate as possible. Ten years ago foundrymen were satisfied to have approximate solutions to casting solidification problems; today accuracy is required. This means using accurate values of thermal parameters involved in metal casting.

Dimensional accuracy and accurate values of thermal parameters are linked in the establishment of interfacial heat transfer coefficients. There is indirect evidence of this[1] in evidence from actual castings, and foundrymen the world over know that dimensions vary when the casting orientation or gating is changed. The reason that varying the gating or the orientation of the casting in the mold affects dimensions was explained by Campbell[2], who pointed out that rapid heat transfer between the metal and mold (as would be the case in the first part of the casting to fill) would cause the metal there to solidify sooner than metal that filled later. The metal that solidifies sooner is stronger sooner, and thus will pull on the later-solidifying metal, causing it to distort.

In the same way, parts of the mold that have a higher interfacial heat transfer coefficient than other parts of the mold will cause the metal there to solidify sooner, and will similarly affect the casting dimensions.

1.1 Theoretical Underpinnings

A fairly impressive number of studies of interfacial heat transfer have been carried out. Most, however, have looked at interfacial heat transfer coefficients in permanent molds. In these studies a gap is found to form between the metal and the mold

during solidification. This occurs when the metal begins to solidify; as it solidifies it contracts. The mold, however, is still hot from the heat transferred from the solidifying casting, and it does not contract. The formation of the gap is accompanied by a ten-fold decrease in the value of the interfacial heat transfer coefficient.

Most also deal with aluminum alloys, to avoid the problems caused by cast iron when the graphite in the metal expands at the end of solidification and causes the metal to push against the mold wall; this prevents a gap from forming between the metal and the mold.

The experimental program we proposed consisted of two parts:

1) Determination of interfacial heat transfer coefficients and gap formation in aluminum alloy/sand mold systems.
2) Determination of the effect of molding media, gating, casting thickness and casting orientation on the dimensional accuracy of sand castings.

In the first part of the program, plate castings 12" x 12" were poured in the Foundry Laboratory at The University of Alabama. These castings varied in thickness, from ¼" to 1", and they were poured in the horizontal, 30, 45, and 60° to the horizontal, and the vertical position. Thermal measurements were made and eddy current detectors were used to measure the formation of a gap between the metal and the mold material. These experiments were described fully in the previous annual reports.[3]

In the second part of the program a casting was designed that had a number of features that would easily demonstrate the effects of varying gating, orientation in the mold, casting thickness, and mold material. These castings were to be poured in green sand, resin-bonded sand, and the lost foam process using both silica sand and low-expansion sand at commercial foundries. Each casting was then to be dimensionally inspected using a coordinate measuring machine at another commercial foundry. Unfortunately, no foundry was able to pour the green sand castings, and, as of the end of the second year of the project, no source of lost foam castings using silica sand had been found.

1.2 Progress during the Third Year

During the third year of the project experiments continued on measuring the interfacial heat transfer coefficients and gap formation. During the third year we added a series of ½" plates to our series, as we had discovered in the second year that the amount of heat transferred is a function of the thickness of the plates. The dependence of interfacial heat transfer on casting thickness is a fact well-known to heat transfer experts, but few foundrymen are familiar with it. We also were able to find a source for lost foam castings poured in silica sand. However, no commercial source was found to pour green sand castings. This is less surprising than it might be, as the pattern equipment was built for loose-piece molding, and few commercial foundries that do such molding have the financial resources to contribute castings to this program.

Because of delays in scheduling the pouring of the lost foam castings, we did not receive the results of the casting measurements until after the end of the reporting period; they will not be included in this report. Also, our attempts to measure interfacial heat transfer coefficients and gap formation did not appear to be completely successful. Our gap formation measurements were ambiguous, suggesting either that a gap does not form reproducibly in resin-bonded or green sand molds and aluminum, or that our method of measurement was inadequate. We also had problems in gathering accurate thermal data from our plate castings, especially those that were ¼" thick. These problems led to a complete review of the methods of temperature measurement used to determine temperatures in thin wall castings.

As a result of the problems we faced in the third year of the project we have requested a no-cost time extension to complete the project.

Details of progress on the three parts of the program (interfacial heat transfer measurements, gap measurements, and casting measurements and analysis) will be presented in separate sections.

2.0 Heat Transfer Measurements

2.1 Synopsis

In year three of this project we identified an important instrumentation principle for measuring temperature responses in sand molds during casting. This led to a second sequence of castings poured with resin-bonded sand that was completed during the summer of 1998. Appended to this report are the results for surface heat flux obtained from these plate castings.

The algorithm for the analysis to determine heat fluxes during casting with green sand was developed and tested numerically. Several castings were also poured in green sand.

We prepared and delivered two conference papers during the third year. The first[4] was delivered at the American Foundrymen's Society 101st Annual Congress in May of 1998. This paper reported on the technique and general findings from the first sequence of plate castings in resin sand. The second paper[5] was prepared for the American Society of Mechanical Engineers' 1998 International Mechanical Engineering Congress and Exposition. This paper reported on the general technique and considered in detail the question of experimental error propagation into the computed results for heat flux.

2.2 Technical Background

The general approach taken to make the heat transfer measurements is based on an inverse heat conduction solution[6] for the surrounding mold medium. Figure 1 depicts a section of a casting, showing the metal (below) the sand (above), and several indicated temperature measurement points. Also suggested by the schematic is the existence of a gap between the metal and the mold, and the heat transfer across that gap. Using temperature measurements in the sand and assuming the thermal properties of the sand are completely known, inverse heat conduction methods are used to find the heat transfer $q(t)$ at the interface. If the surface temperature of the solidifying metal is also measured, then the interfacial heat transfer coefficient can also be determined.

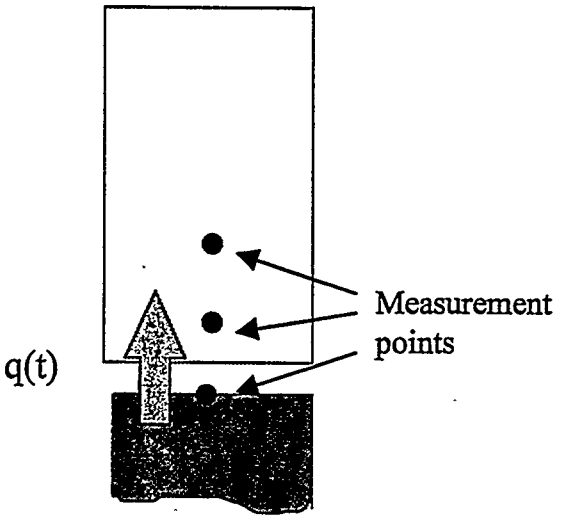

Figure 1. Schematic of Casting Section

2.3 Plate Castings

Plate castings of varying thicknesses were poured in resin-bonded sand and green sand. The Industrial Steering Committee expressed concern about the mixing of resin on a volumetric basis. This practice has continued, but has been augmented by recording the mass of each volumetrically measured quantity, with a goal of quantifying the error resulting deviation. November, Table 1 summarizes these measurements. Part III for the resin was always metered gravimetrically. The last column is a computation of the percentage resin, assuming a 200 lb. batch of sand (the sand is always weighed and in 50 lb increments).

The averages and standard deviations of all of the measurements are shown in the table. The last line of the table indicates the percentage scatter in the portions. Assuming a normal distribution of errors, there is 95% confidence that the amount of Part I added was 749.3 g ± 5.4%, Part II was 584.9 g± 8.1%, and Part III was 15.2 g± 2.5%. This in turn suggests that the total amount of resin added in each batch was between 1.40% and 1.56% (again using 95% confidence intervals).

A similar statistical analysis has been conducted on all resin-bonded molds to determine the overall bulk density of the molds. Based on 68 mold halves, the average density was found to be 1566 kg/m^3, with a standard deviation of 77 kg/m^3. This corresponds to a 95% confidence interval of density between 1411 kg/m^3 and 1721 kg/m^3.

Table 1 – Mass of Resin Mixes

Date	Mold	Part I (g)	Part II (g)	Part III (g)	% Resin
11/12/97	1" Bot.	776.0	596.0	15.2	1.53%
11/12/97	0.25" Bot.	751.0	612.0	15.3	1.52%
11/12/97	1" Top	750.0	607.0	15.3	1.51%
11/12/97	0.25" Top	780.0	600.0	15.4	1.53%

11/21/97	1" Bot.	741.1	565.6	14.8	1.45%
11/21/97	0.25" Bot.	740.5	575.9	15.4	1.46%
11/21/97	1" Top	758.1	567.7	15.1	1.47%
11/21/97	0.25" Top	738.5	614.2	15.4	1.50%
12/2/97	1" Bot.	737.8	558.6	15.0	1.44%
12/2/97	0.25" Bot.	746.4	527.0	15.1	1.42%
12/2/97	1" Top	725.5	567.3	15.1	1.44%
12/2/97	0.25" Top	746.2	564.4	15.0	1.46%
12/8/97	1" Bot.	719.8	591.8	15.0	1.46%
12/8/97	0.25" Bot.	727.0	555.8		1.41%
12/8/97	1" Top	730.9	571.8	15.0	1.45%
12/8/97	0.25" Top	754.7	561.5	15.1	1.46%
12/15/97	1" Bot.	748.3	563.7	15.0	1.46%
12/15/97	0.25" Bot.	709.2	571.2	15.0	1.42%
12/15/97	1" Top	768.9	605.1	15.0	1.53%
12/15/97	0.25" Top	711.2	587.9	15.5	1.45%
	Average	743.1	578.2	15.1	1.47%
	St Dev	19.4	22.6	0.2	0.038%
	2*sigma	5.2%	7.8%	2.5%	

Our practice for green sand is 6% Western Bentonite clay in 94% silica sand. This dry mixture is bonded with 4% moisture before molding.

Table 2 gives a summary of the first sequence of plates poured in resin-bonded sand. The table is presented to indicate the data acquired during these tests. A second series of tests were poured later in the year, including ½" plates in green and resin-bonded sand.

Table 2 - Summary of Pours (First Sequence)

Date	Description	Pour Temp(C)	Filling time (s)	Max Sur Temp(C)	Peak Flux (W/m^2)	Interfacial h_c W/m^2-C
5/12/97	1" Plate Pour	673		582	65000	60-200
5/15/97	1" Plate Pour	673		591	51000	150-400
5/15/97	0.25" Plate	672		596	45000	75-150
5/23/97	0.25" Plate	722		593	58000	50-150
5/23/97	1" Plate Pour	672		595	48900	
5/29/97	0.25" Plate	742		596	60000	70-190
5/29/97	1" Plate Pour	672		617	72000	100-200
6/03/97	0.25" Plate	737		648	64000	50-160
6/03/97	1" Plate	669		609	65000	100-250
6/05/97	0.25" Plate	740		599	64000	50-140
6/05/97	1" Plate	674		609	82000	70-250
6/12/97	0.25" Plate	737		594	54000	60-130
6/12/97	1" Plate	672		607	70000	150-200
7/08/97	0.25" Plate	737		588	57000	20-150
7/08/97	1" Plate	673		612	76000	100-200
7/10/97	0.25" Plate	743		614	60000	60-120
7/10/97	1" Plate	673		631	67000	100-200

7/15/97	0.25"–30 deg.	738		n/a[1]	50000	n/a[1]
7/15/97	1" Plate	672		632	55000	50-150
7/17/97	0.25" Plate	720		Problem with Data Acquisition		
7/17/97	1" Plate	673		Problem with Data Acquisition		
7/24/97	0.25" Plate	741		580	400000	50-170
7/24/97	1" Plate	670		590	160000	230-300
8/05/97	0.25"-30 deg.	741		Problem with Data Acquisition		
8/05/97	1" - 30 deg.	665		634	450000	200-700
8/07/97	0.25"-30 deg.	742		Problem with pour – bleed out		
8/07/97	1" - 30 deg.	671				
8/12/97	0.25"-30 deg.	??*		560	350000	75-250
8/12/97	1" - 30 deg.	??*		605	180000	150-300
8/19/97	0.25"-30 deg.	738		584	90000	75-250
8/19/97	1" - 30 deg.	667		584	250000	300-2000
8/27/97	0.25"-45 deg.	733		600	300000	75-250
8/27/97	1" - 45 deg.	670		593	350000	n/a[2]
9/03/97	0.25"-45 deg.	740		636	300000	50-250
9/03/97	1" - 45 deg.	672		627	100000	150-300
9/10/97	0.25"-45 deg.	742		582	250000	50-200
9/10/97	1" - 45 deg.	672		604	500000	100-300
9/17/97	0.25"-45 deg.	??*		591	300000	80-150
9/17/97	1" - 45 deg.	??*		618	350000	n/a[2]
9/24/97	0.25"-60 deg.	738		616	250000	50-150
9/24/97	1" - 60 deg.	667		596	280000	n/a[2]
10/01/97	0.25"-60 deg.	744		603	350000	70-175
10/01/97	1" - 60 deg.	668		560	300000	n/a[2]
10/10/97	0.25"-60 deg.	742		591	280000	50-250
10/10/97	1" - 60 deg.	663		602	350000	n/a[2]
10/22/97	0.25"-60 deg.	742		588	300000	50-200
10/22/97	1" - 60 deg.	672		560	n/a[2]	n/a[2]
11/05/97	1" - vertical	666	12	595	135000	50-175
11/12/97	0.25" – vertical	739	11.6	587	n/a[2]	n/a[2]
11/12/97	1" – vertical	672	18.7	601	400000	125
11/21/97	0.25" – vertical	731	6.2	596	225000	70-200
11/21/97	1" – vertical	668	8.3	585	130000	130-200
12/03/97	0.25" – vertical	743	5.7	587	100000	100-150
12/03/97	1" – vertical	670	6.6	601	100000	50-200
12/08/97	0.25" – vertical	743	5.9	579	100000	100-150
12/08/97	1" – vertical	670	7.6	593	120000	50-150
12/15/97	0.25" – vertical	743	--	Problem with pour – bleed out		
12/15/97	1" – vertical	670	12.3	588	250000	150-225

Notes:
*Actual values not recorded.
[1]No surface temperatures recorded – sensor failure
[2]Poor x1 and Sur data precluded computation

The summer pouring schedule was completed on August 25. Table 3 shows the index of this schedule.

Table 3 – Pouring Schedule (Second Sequence)

Date	Plate	Thickness	Orientation	Status
17-Jun-98	1	0.25"	45 degrees	Complete
17-Jun-98	2	0.50"	45 degrees	Complete
18-Jun-98	3	0.25"	45 degrees	Complete
18-Jun-98	4	0.50"	45 degrees	Complete
24-Jun-98	5	0.25"	45 degrees	Complete
24-Jun-98	6	0.50"	45 degrees	Complete
25-Jun-98	7	0.25"	45 degrees	Complete
25-Jun-98	8	0.50"	45 degrees	Complete
01-Jul-98	9	1.00"	45 degrees	Complete
01-Jul-98	10	1.00"	45 degrees	Complete
02-Jul-98	11	1.00"	45 degrees	Complete
02-Jul-98	12	1.00"	45 degrees	Complete
08-Jul-98	13	0.25"	Vertical	Complete
08-Jul-98	14	0.50"	Vertical	Complete
09-Jul-98	15	0.25"	Vertical	Complete
09-Jul-98	16	0.50"	Vertical	Complete
15-Jul-98	17	0.25"	Vertical	Complete
15-Jul-98	18	0.50"	Vertical	Complete
16-Jul-98	19	0.25"	Vertical	Complete
16-Jul-98	20	0.50"	Vertical	Complete
22-Jul-98	21	1.00"	Vertical	Complete
22-Jul-98	22	1.00"	Vertical	Complete
23-Jul-98	23	1.00"	Vertical	Complete
23-Jul-98	24	1.00"	Vertical	Complete
29-Jul-98	25	0.25"	Horizontal	Complete
29-Jul-98	26	0.50"	Horizontal	Complete
30-Jul-98	27	0.25"	Horizontal	Complete
30-Jul-98	28	0.50"	Horizontal	Complete
05-Aug-98	29	0.25"	Horizontal	Complete
05-Aug-98	30	0.50"	Horizontal	Complete
06-Aug-98	31	0.25"	Horizontal	Complete
06-Aug-98	32	0.50"	Horizontal	Complete
12-Aug-98	33	1.00"	Horizontal	Complete
12-Aug-98	34	1.00"	Horizontal	Complete
13-Aug-98	35	1.00"	Horizontal	Complete
13-Aug-98	36	1.00"	Horizontal	Complete

2.4 Heat Transfer Results

Because we were experiencing difficulties with the subsurface thermocouples, especially on the 1" plate, we tried using "L"-shaped and straight thermocouples imbedded in each mold at a 5 mm nominal depth in a casting early in the year. This depth is the same as that used in the early pours, while the later pours have used a 0-0.5 mm depth. Figure 2 shows the temperature traces for each of these thermocouples. The actual depths were measured for each of the thermocouples; only the approximate average value for each pair is indicated on the chart.

Figure 3 shows the temperature traces obtained on the "A" plate poured on 02/13/98. This case is especially significant since the thermocouple depths are nearly all equal at a nominal depth of 5 mm. The actual depth for each sensor, which is measured after the mold is cooled using a micrometer depth probe, are shown in the figure. Note that the two "L" thermocouples (top and bottom) are virtually coincident up until a time of about 250 seconds. Also note that the two "straight" thermocouples have a shape similar to each other (but different from the "L" TCs) during this time. The two straight TCs' responses are not as identical, as they differ by about 0.5 mm in depth from the heated surface.

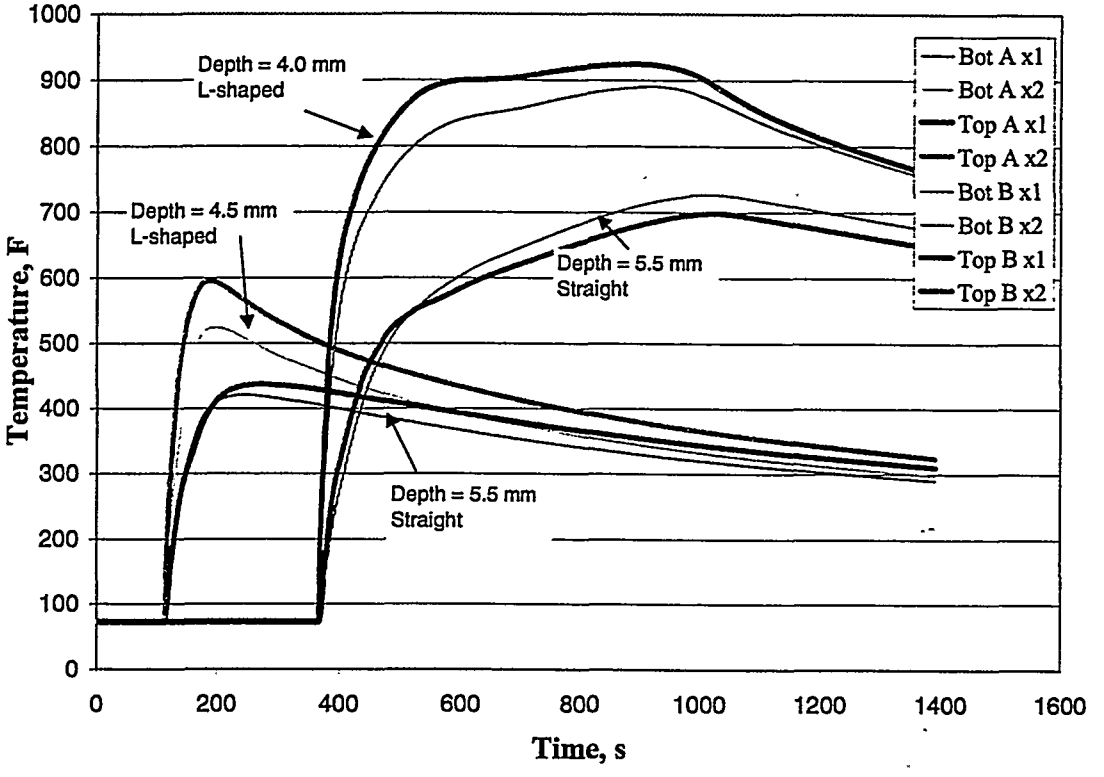

Figure 2. Response of "Bent" versus "Straight" thermocouples.

The difference in the initial (up to 250 secs) response of the "straight" versus the "L" thermocouples is believed to be due to a deterministic thermocouple error in the "straight" sensor. The rationalization for this can be explained as follows. Figure 4a depicts the "straight" installation. The conductivity of the thermocouple wire is much greater than that of the surrounding sand (about 20 W/m-C for the metal and about 1 W/m-C for the sand), and the thermal capacitance of the wire is also greater (about 3.8 MW/m^3-C for the metal versus 1.2 MW/m^3-C for the sand). Therefore the thermocouple extension wire provides a preferentially conductive path for heat flow and storage from the region near the heated surface. This heat loss along the thermocouple wire is in turn conducted from the sand near the tip of the thermocouple, resulting in a depression in the temperature in the vicinity of the thermocouple tip. This depression is shown schematically in Figure 4a, and can be seen in Figure 3 as the difference between the "L" and "straight" thermocouple readings. The idea of the "L" bend is to project the

thermocouple bead out into the medium, away from the temperature depression. This is shown schematically in Figure 4b, where the bead of the thermocouple is in a region of undisturbed temperature field.

Another important observation can be made in consideration of Figure 3. At about 250 seconds, the top and bottom thermocouples (both the "straight" and the "L" variants) begin to depart. The effect is most marked in the "L" shaped thermocouples. But in both instances, the thermocouple on the bottom continues heating at a higher rate than its mate on the top. This is due to a decrease in the heat transfer coefficient on the upper surface

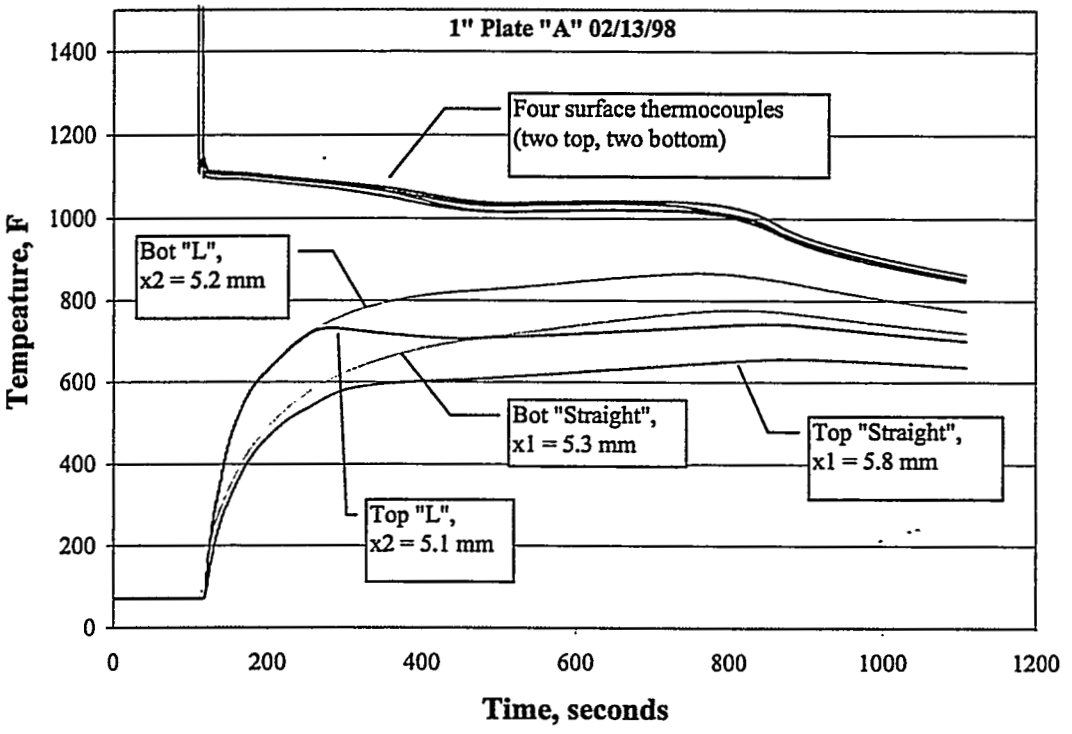

Figure 3. Temperature Histories from Pour0213

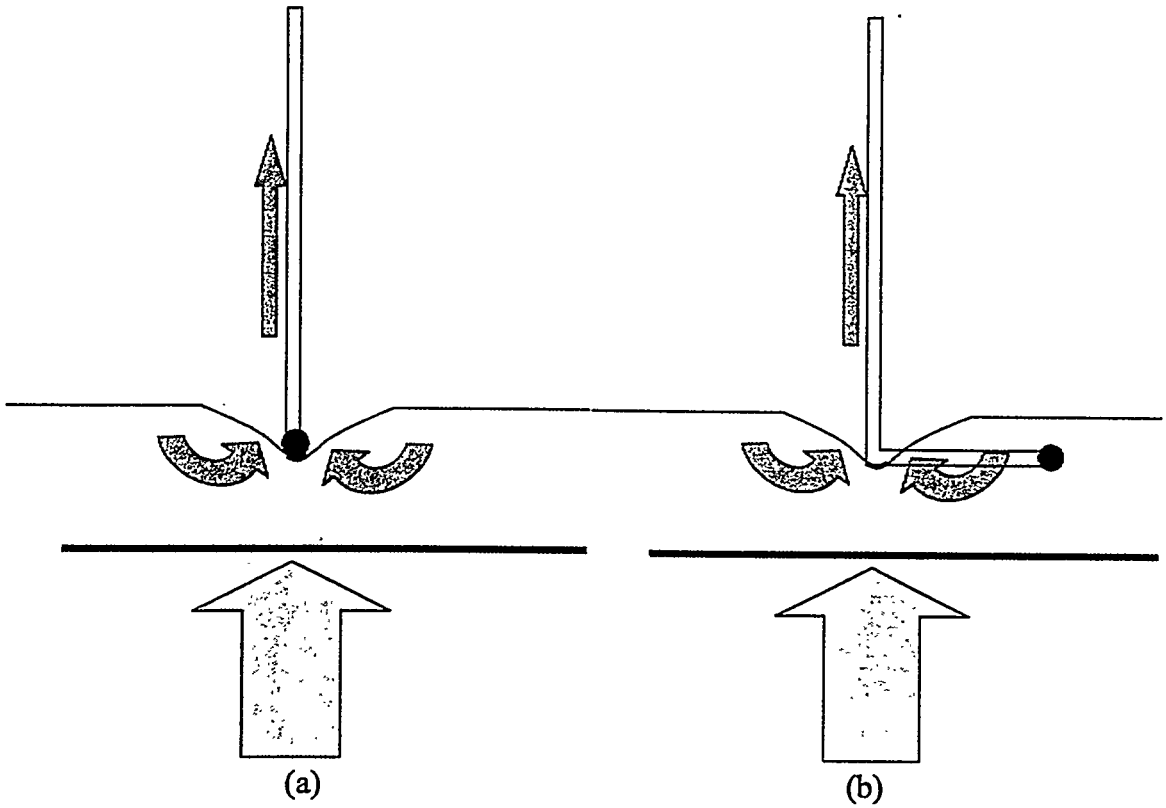

Figure 4. "Straight" (a) and "L" (b) thermocouple installations

associated with the first stages of solidification. The concomitant measured value of the temperature of the surface of the metal at this instant is about 1089 F (587 C).

Concerns were raised by the Monitoring Committee about the two styles of thermocouple installations. We conducted tests to investigate this issue. Three tests were run with thermocouples in both configurations, but the results were inconclusive. A typical experiment and result will be described here.

Two thermocouples, one bent and one straight, were tested by imbedding them in a resin bonded sand cube and heating them on a stainless steel plate. The stainless steel plate was heated from below by a 1000W electric heater. The stainless steel heating plate had been previously calibrated with a hand-held thermocouple probe. This procedure revealed non-uniformity on the heated surface, due entirely to variations in the underlying heater's construction. A portion of the calibration data is shown in Table 3. Figure 5 shows the layout of the heater plate and the location of the imbedded thermocouples. The "+" thermocouples are on the bottom of the stainless steel plate, and the "x" thermocouples are on the upper surface. The labels "TC1", "TC2", etc. are associated with upper surface thermocouples and correspond to the entries listed in Table 4. The data shown in Table 4 are the temperatures observed with the hand-held probe at the EDGE, the TC ("x" in Figure 1), and the middle (center) of the plate along a radius through each upper surface thermocouple at different stages during heating of the plate. As can be seen by the data in Table 4, there is both a peripheral and a radial variation in the surface temperature. The data from Table 4, along with the independently measured

temperatures of TC1, TC2, TC3, and TC4, allow the actual surface temperature on the plate to be calculated based on the measurements at the TCs.

Also shown in Figure 5 and marked by a diamond are the x-y locations of the straight ("x1") and bent ("x2") thermocouples for this test (these were determined after the fact by measurement). The dotted line in Figure 5 shows the outline of the resin bonded sand pack.

The two thermocouples, one straight and one bent, were installed into a 3x3x3 inch cube of resin bonded sand. The thermocouples were placed nominally 1/4" from the bottom surface with the aid of a shim while packing the cube. The cube was then placed on the stainless steel plate. Heating was applied in stages, and temperatures were recorded continuously at 1 s intervals using a data acquisition system.

Figure 6 shows the temperatures obtained for x1 and x2 thermocouples (lower curves). The upper curves are the temperature histories in the region below the x1 and x2 thermocouples (in Figure 5). These temperature histories were obtained with the measured TC data (TC1, TC2, etc.) and by making use of the correction data in Table 3. Specifically, the surface temperature below x1 was taken to be the temperature at the TC2, while the surface temperature below x2 was taken to be that at the MIDDLE for TC3. Note that the surface temperature below x1 is greater than that below x2 (Figure 6).

The depths of the thermocouples from the heated surface were obtained after the experiment using a micrometer depth probe. This measurements revealed that x1 was 6.6 mm from the heated surface while x2 was 6.2 mm. Thus, x2 was 0.4 mm closer (0.016") to the surface than x1. Figure 6 reveals that x2 did in fact have a higher temperature response than x1, but recall that the surface temperature below x1 is greater than that below x2. Thus, the results are inconclusive.

As part of our investigation, one member of the Monitoring Committee (Tony Midea of Foseco, Inc.) ran solidification simulations to mimic our test. The result of his simulations suggested that sensor position is the primary source of variability, but our foundry tests showed a consistent difference in the responses observed with bent versus straight thermocouples.

Figure 7 shows the two thermocouple traces from the 02/13/98 pour which precipitated the debate. The upper curve is the "bent" thermocouple ("x_2"), which was measured at a 5.2 mm depth below the mold surface. The lower curve is a "straight" thermocouple ("x_1") measured at a 5.3 mm depth. To test the consistency of these measurements, the heat flux results based on the upper curve were modeled (as a piecewise linear function) and used to simulate the temperature history through the entire mold thickness (using a one-dimensional conduction analysis). From this simulation, the temperature histories at 10 locations at 1 mm depth increments were obtained. These histories are seen as the darker lines in Figure 8. No attempt has been made to key these to the legend; the upper curve is the 1mm depth, and the lower curve is the 10 mm depth. All of these computed histories are truncated at 1000 seconds; the other two traces which extend to about 1100 seconds are the experimental values from Figure 7.

Table 4 Calibration data for the steel plate

TC	EDGE(°F)	TC(°F)	MIDDLE(°F)
T1	70	69	69
T2	69	69	69
T3	69	69	69
T4	69	69	69
T1	292	293	283
T2	266	294	285
T3	286	283	288
T4	264	273	274
T1	441	449	430
T2	449	446	445
T3	435	441	442
T4	425	429	422
T1	526	528	516
T2	525	520	518
T3	513	520	512
T4	501	514	514
T1	675	672	666
T2	664	666	663
T3	652	651	636
T4	648	641	652
T1	795	796	765
T2	796	770	777
T3	760	762	763
T4	748	751	762
T1	850	856	810
T2	834	841	844
T3	821	838	847
T4	823	824	845

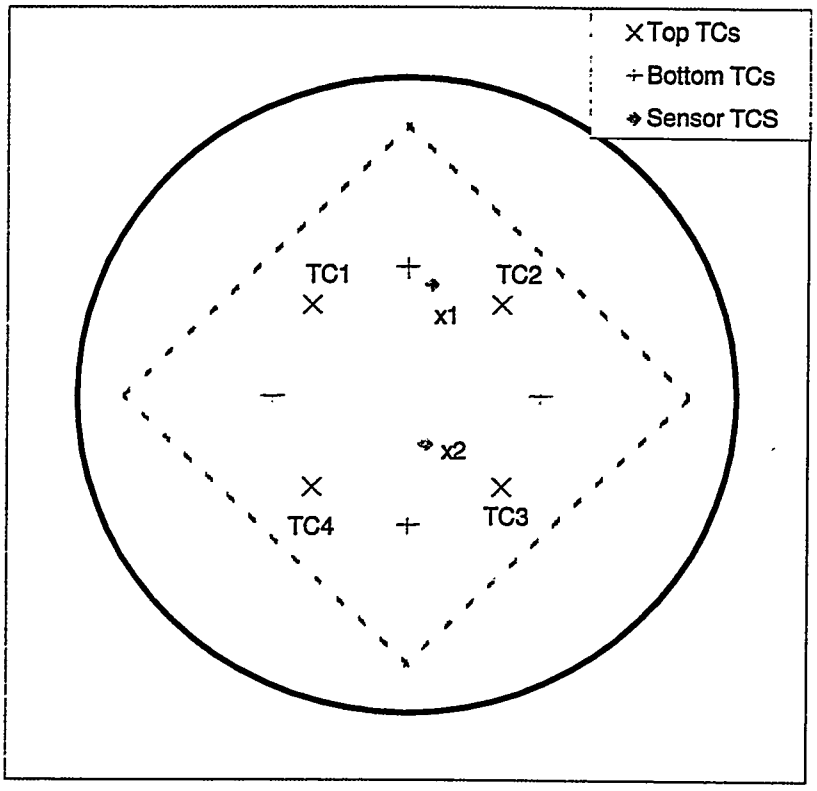

Figure 5. Plan View showing location of thermocouples

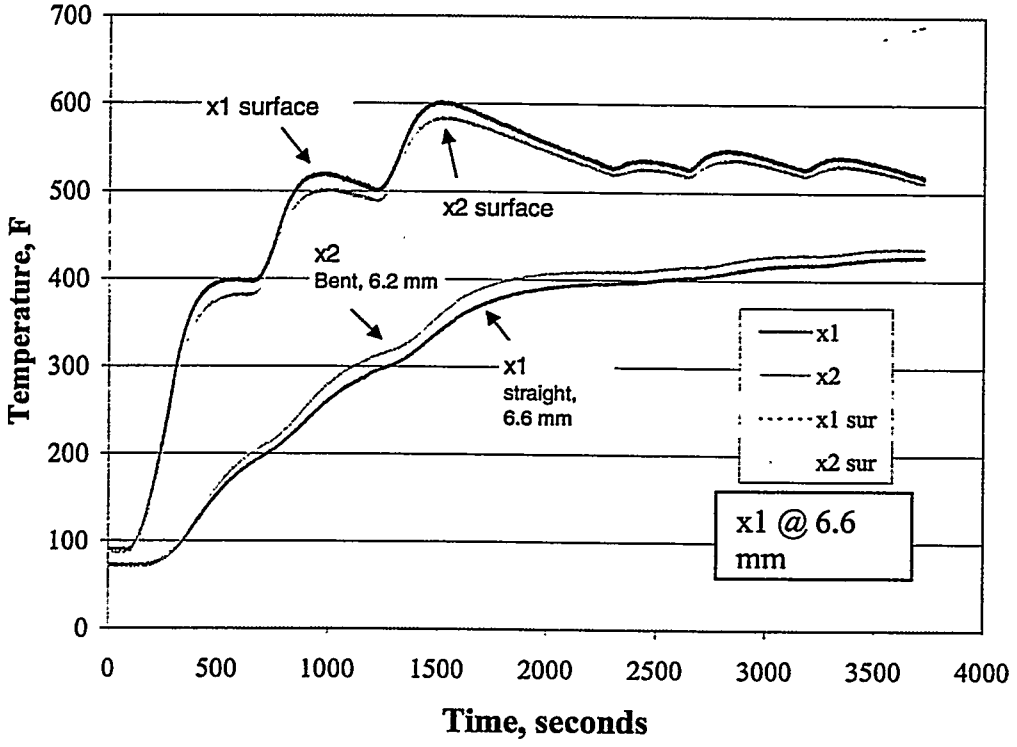

Figure 6. Temperatures for the Thermocouple test

In Figure 8, the upper experimental curve is the "bent" thermocouple and the lower thicker line is the straight one. The bent TC follows between the 5mm and 6 mm computed traces, as it should, although it meanders a bit. This is due to the imperfection in the model of the surface heat flux – the straight-line segments used did not follow the heat flux exactly. Note, however, that the "straight" thermocouple deviates significantly from the 5-6mm range, and the character of the response is significantly different from the computed responses (it does not parallel the other curves but rather intersects several of them). Thus, it seems that the response of the straight thermocouple is inconsistent with that of the bent thermocouple in a manner that suggests something more than a simple difference in depth.

The simulations heightened our sensitivity to the issue of thermocouple depths. We also realized that the actual *effective* thermocouple junction depths were greater than the measured depths, since we measured to the tip of the exposed junction, and the thermocouple bead was about 1 mm in diameter. Thus, the measured depths for the straight thermocouple may be up to 1 mm smaller than the actual depth, and for the bent thermocouple might be as much as 0.5 mm smaller than the actual.

For this reason, we prepared a new thermal pack mold. Part of the drawing for this mold is shown in Figure 9. The key feature of this new instrument pack is the presence of thermocouple positioning holes (seen in the sides of the drawing at the bottom of Figure 9). These molds are packed from above; that is, into the cavity seen looking at Figure 9. The thermocouples are laid from the sides (through the holes shown in the bottom drawing in Figure 9). The use of this mold facilitated more consistent positioning of thermocouples. Figure 10 shows a photograph of a thermocouple in the positioning hole of the new instrument pack mold.

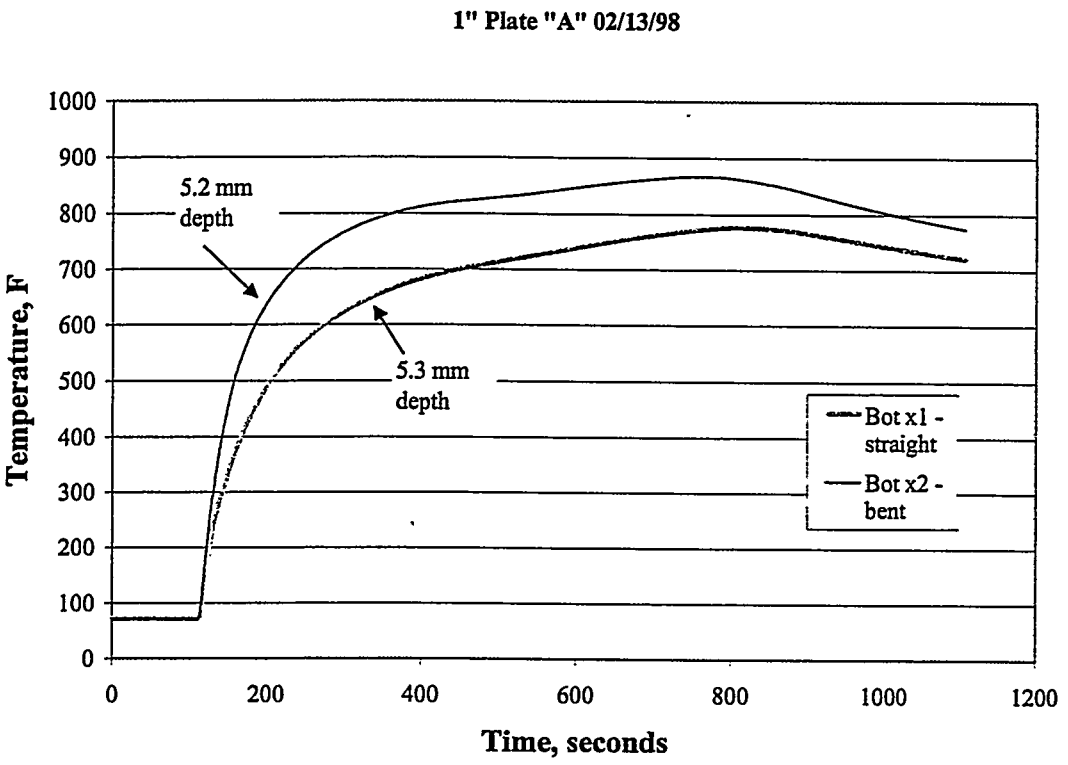

Figure 7. Thermocouple data from bottom of plate, pour0213a

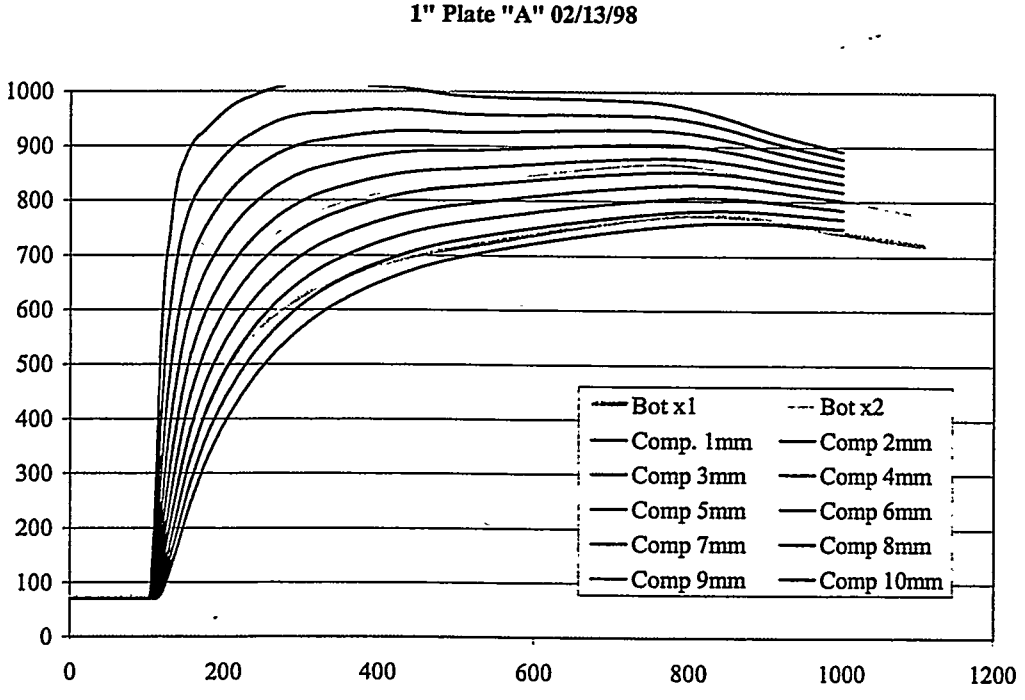

Figure 8. Comparison with computed temperatures

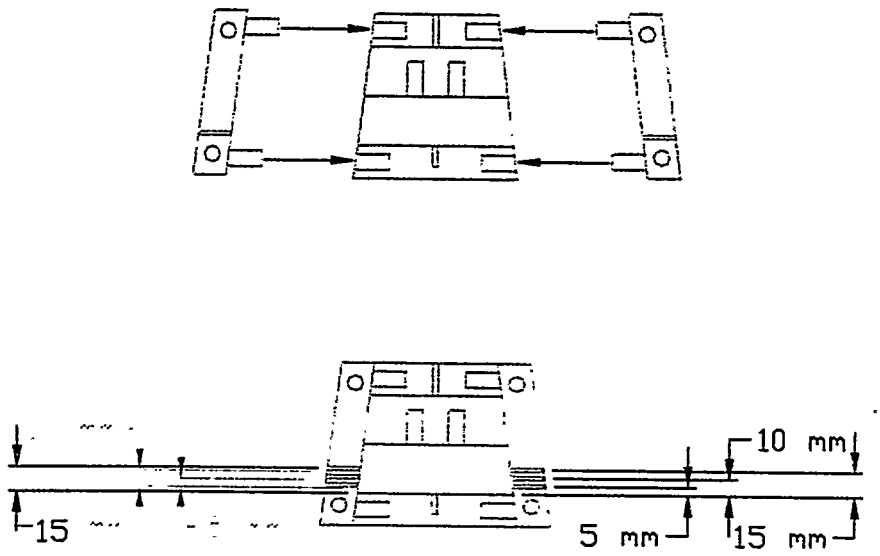

Figure 9 Drawing for new thermocouple instrument pack

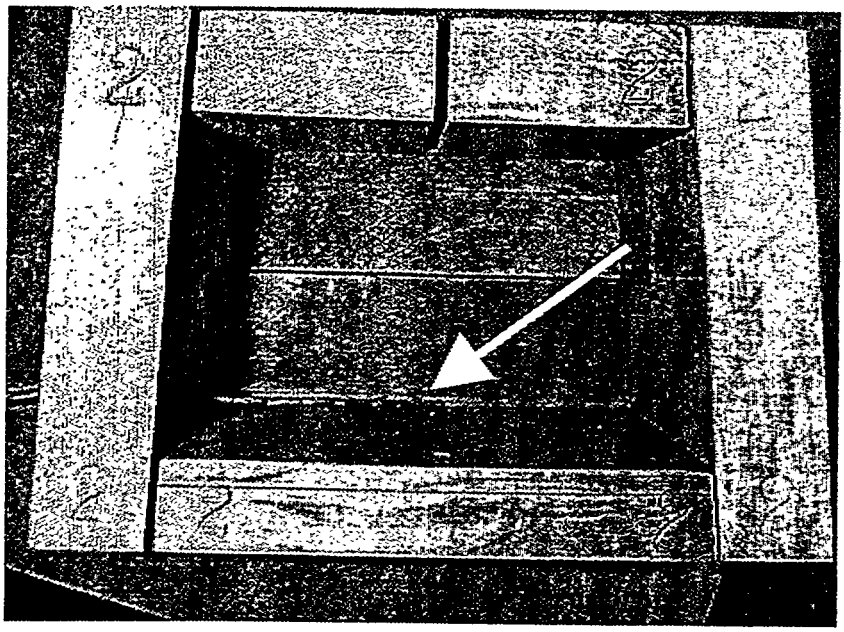

Figure 10. Photo showing placement of thermocouple in instrument pack mold.

We then developed a simple finite element computer model to look at the issue of "bent" versus "straight" thermocouples and possible measurement errors. Our results

from these models contradicted the findings of Mr. Midea. Our model showed that the presence of a small wire in a sand medium could result in a significant error in temperature measurement.

Figure 11 shows a schematic of the model for our simulation. The model consisted of a single wire of constant diameter and thermal properties. The wire had a thin layer of fiberglass insulation and is imbedded in a cylindrical domain filled with sand. This geometry allowed for an axisymmetric formulation. The thermal properties we used were:

	Wire	Insulation	Sand
Thermal Conductivity (W/m-K)	22.8	0.036	1.0
Density*Specific Heat (MJ/m^3-K)	3.85	0.0835	1.4

The properties of the wire corresponded to those of only one leg of the thermocouple pair. Type K wire is Ni90%-Cr10% in one leg and Ni95%-Al2%-Mn2% in the other. The properties of Ni90%-Cr10% were readily available and were taken as representative of the wire. The properties of the sand are typical for silica sand. To combine the two thermocouple wires into one, an effective diameter with the same cross sectional area as the two separate wires was used. This leads to the relation:

$$D_{eff} = SQRT(2)\ d_{wire}$$

where d_{wire} is the diameter of one of the thermocouple lead wires.

We simulated 24 gage thermocouple wire (d_{wire} = 0.0201" = 0.508 mm) with a thickness of 0.320 mm of insulation. 3 mm of insulation was stripped from around the tip of the wire. The wire was set back from the surface of the sand 5.2 mm, and the "cylinder" of sand had an outer radius of 10 mm. The total length of the "cylinder" was 100 mm.

Piecewise linear heat flux was used as the excitation on the surface of the sand. Figure 12 shows this piecewise linear heat flux, and the underlying heat flux history on which it is based. On careful inspection, it can be seen that the model heat flux is a little high in the region from 200 to 300 seconds, and a little low in the region from 500 to 700 seconds.

Figure 13 shows the results from the simulation along with the experimental data from "pour0213". The two long histories, with annotations indicating the measurement positions, are the experimental data. The three shorter ones (truncated at about 600 seconds) are from the simulation. The upper of these three curves is keyed as "sand(F)" in the graph. The data for this curve was extracted from the simulation at the same distance from the surface as the wire, but at the edge of the sand cylinder (near the location labeled "2" in Figure 11). Note that this history closely follows the experimental data for the "bent" thermocouple, but overshoots a bit in the region from 200 to 300 seconds (where the model heat flux is a bit high) and begins to drop below the experimental data at about 500 seconds (where the model heat flux is low).

The second "short" curve in Figure 12 is keyed as "wire (F)". The data for this curve was extracted from the simulation results at the tip and on the centerline of the wire (near the location labeled "1" in Figure 11). Note that this curve is about 40 to 50 F degrees below that for the "sand" and the experimental data. A third "short" curve is shown in Figure 12 and this curve is keyed "wire-1mm". This corresponds to the simulation results on the wire centerline 1 mm from the tip. (This approximates our error in measuring the thermocouple junction location). Note that this results in an additional 5 to 10 F degrees error in temperature over the wire tip.

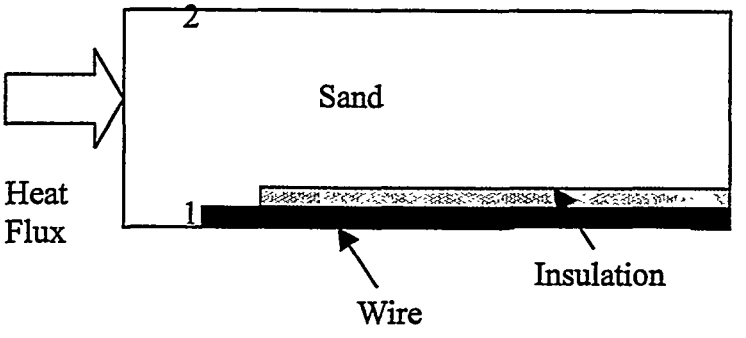

Figure 11. Schematic of Thermocouple Wire for Simulation

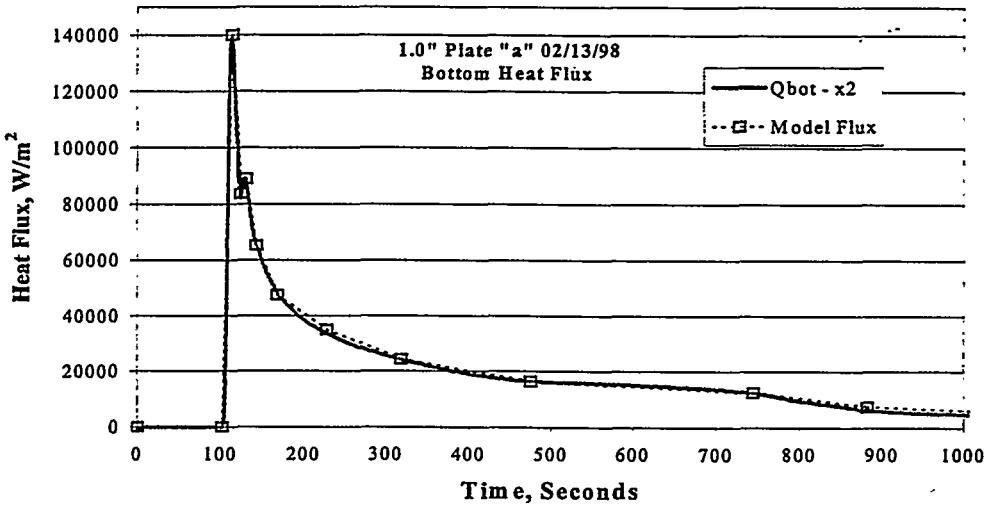

Figure 12. Heat Flux Model from pour0213a

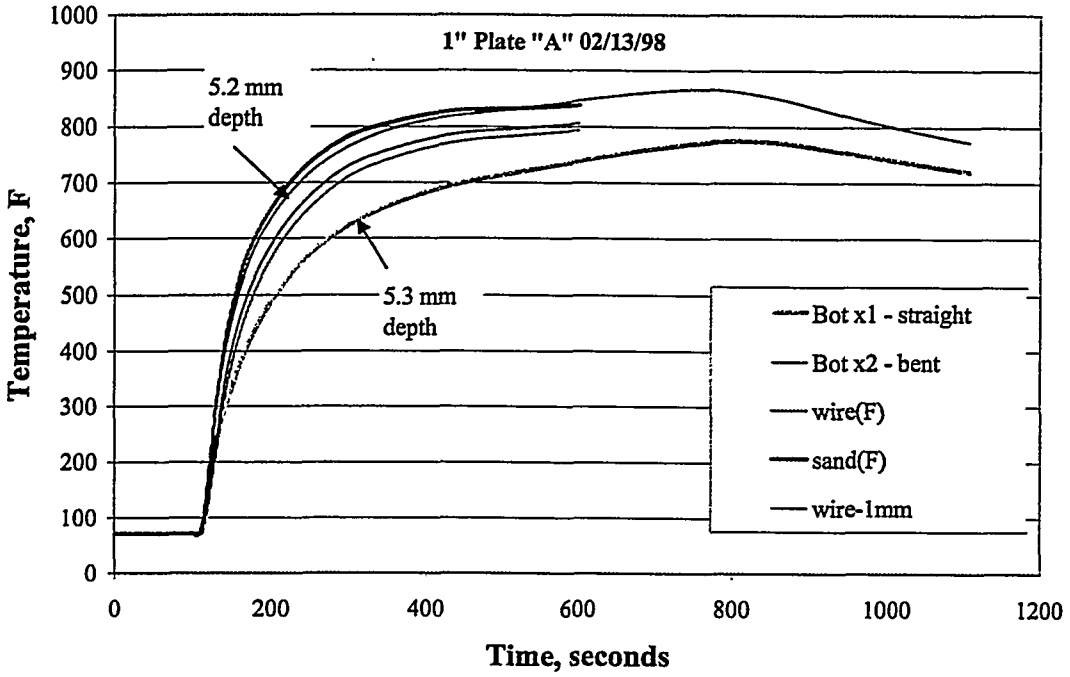

Figure 13. Comparison with computed temperatures

Figure 14 and 15 show composite results from four vertical pours on 1" plates. Figure 15 shows the heat fluxes measured on the "bottom" surface of the casting, while Figure 16 shows that on the "top". (These both refer to the sides of the vertical plate; the "top"/"bottom" designation is used in our data acquisition system.) The results are highly reproduced in the four pours, especially for the "bottom".

We have analyzed several cases for different thermocouple configurations to determine the probable error in a thermocouple reading when the thermocouple is installed perpendicular to a heated surface. The combinations considered are summarized in Table 5. All the cases were simulated using the same parameters and heat flux function as used previously. The results (see Figure 16) indicate that the error in the readings increases for fully sheathed thermocouples (no bare wire exposed). As expected, the error decreases as the depth from the heated surface increases.

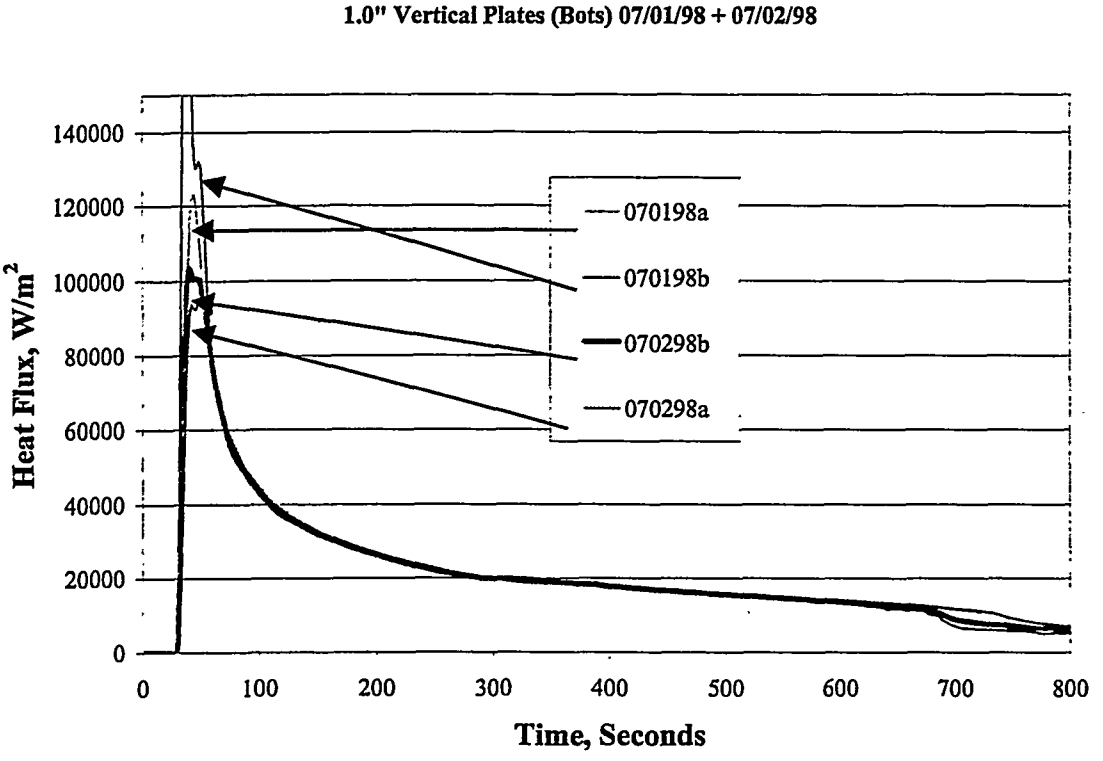

Figure 14. Heat Fluxes from four pours on one face of a vertical 1" plate casting.

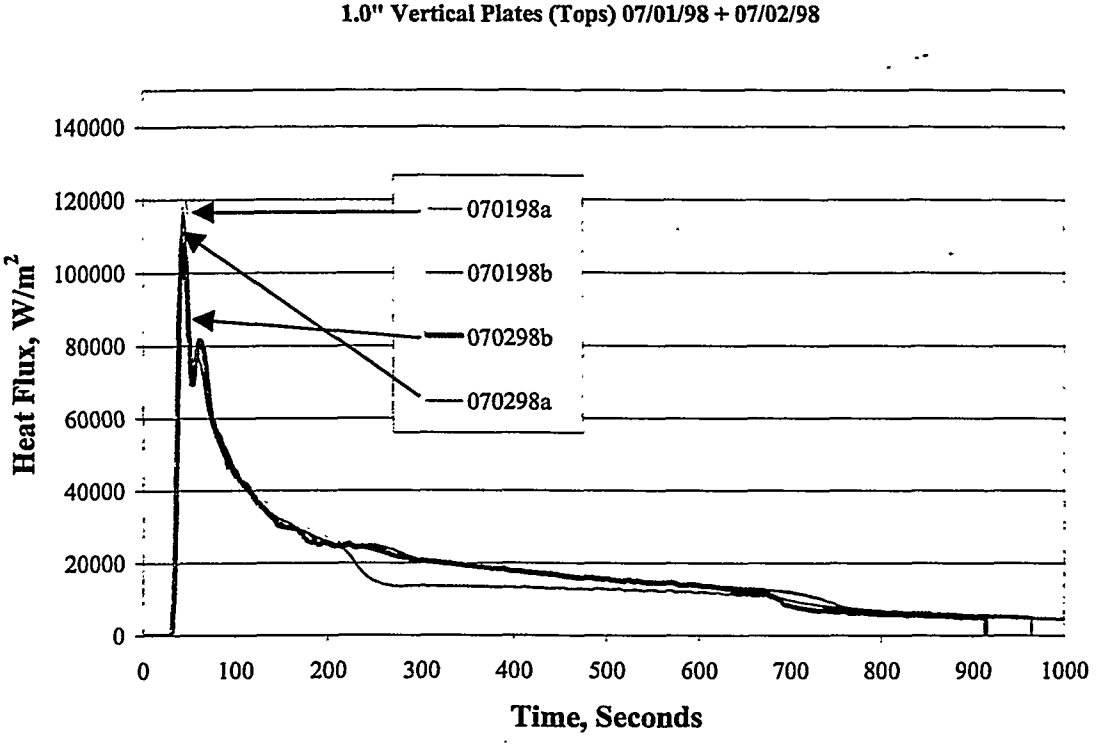

Figure 15. Heat Fluxes from four pours on other face of a vertical 1" plate casting.

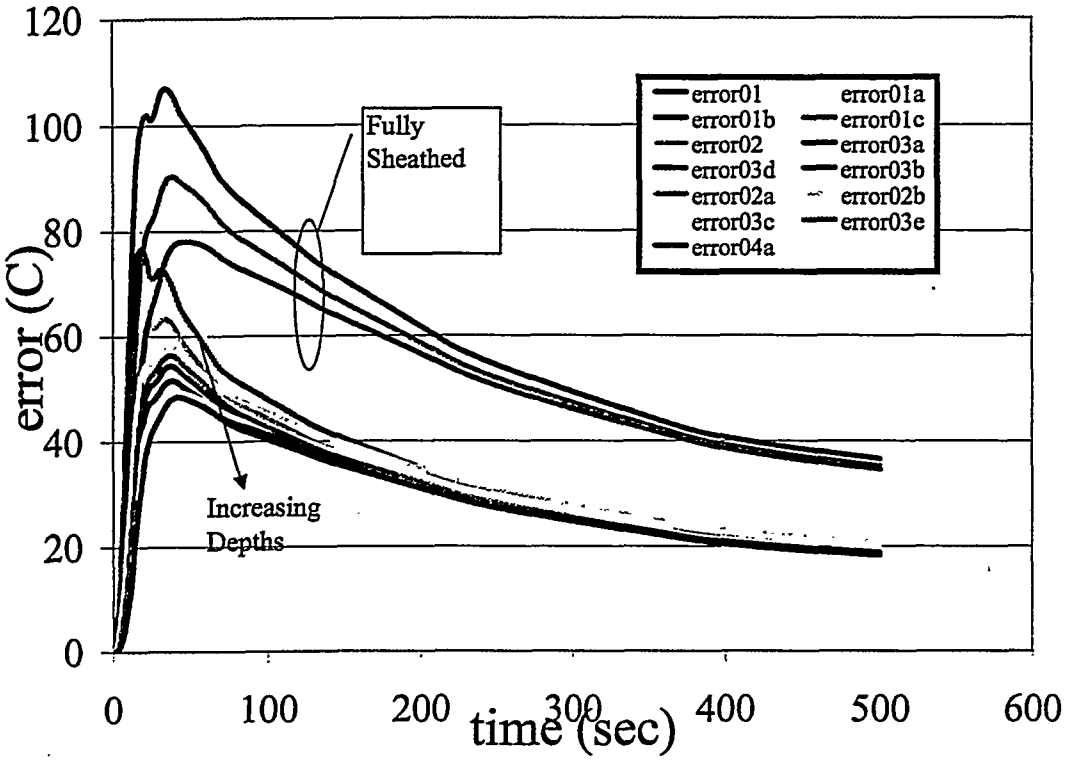

Figure 16. Simulated TC errors for different wire parameters.

Table 3. Cases considered for TC error simulations

NAME	Wire Radius (mm)	Insulation thickness (mm)	TC depth (mm)	bare length (mm)
01	0.3592	0.32	1	3
01A	0.3592	0.32	1	3
01B	0.3592	0.32	1	0
01C	0.3592	0.32	1	2
01D	0.3592	0.32	1	1
02	0.3592	0.32	2	3
02A	0.3592	0.32	2	0
02B	0.3592	0.32	2	1
03A	0.3592	0.32	3	3
03B	0.3592	0.32	3	2
03C	0.3592	0.32	3	1
03D	0.3592	0.32	3	0
03E	0.3592	0.32	3	4
04A	0.3592	0.32	4	4

2.5 Green Sand Algorithm Development

We developed an inverse algorithm to reduce the results from green sand. This algorithm uses the three zone (dry sand, vapor transport, and external) model. The first step in the algorithm development was to compute the sensitivity coefficients for sensors in the green sand.

Figure 17 shows the sensitivity coefficients for sensors in green sand at x=0, 1, 3, 5, and 10 mm below the surface. Also shown are the time histories of the vapor and condensation interfaces (the boundaries of the vapor transport zone). The results in Figure 16 are for a constant and relatively high heat flux (200,000 W/m^2) and can only be taken as a trend; actual sensitivity coefficients will depend on the actual heating rate. The important fact to note from Figure 14 is that for any sensors below the surface, there will be some "dead time" before the measurement can yield any information about the surface disturbance. This time is associated with the vaporization and condensation of the moisture. The closer the sensor is to the surface, the shorter the "dead time" is.

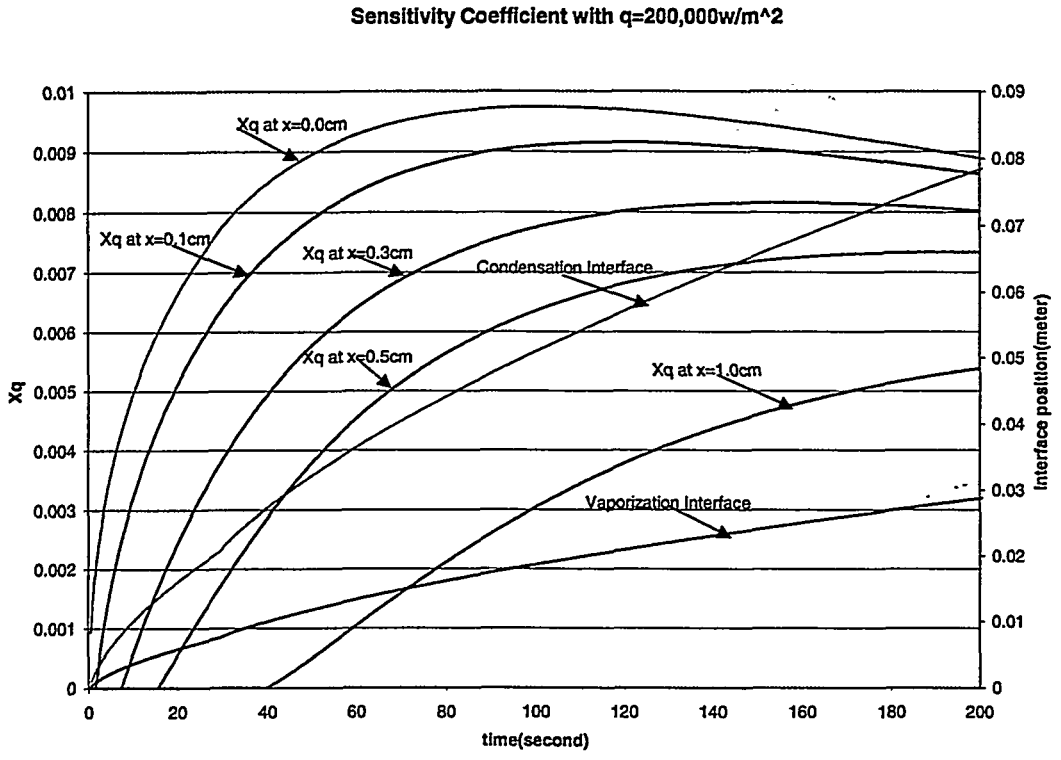

Figure 17. Sensitivity Coefficient for Green Sand.

2.6 Continuing Work

We are in the process of developing an algorithm to determine the interfacial heat transfer coefficient directly from the data. This algorithm will use the measured solidifying metal surface temperature in addition to the subsurface mold temperature responses. Such an algorithm will be able to give the best estimate of the interfacial heat transfer coefficient in response to all available experimental measurements. We continue to look at measurement errors, and are now concerned about the errors induced in the measured solidifying metal surface temperature due to conduction along the wire leads. We will perform some simulations to investigate the magnitude of this error.

We have constructed a WWW page that highlights in words and pictures the work in the foundry. This is targeted for non-foundrymen and is informational for potential new and former students in Mechanical Engineering. The page(s) can be viewed from www.me.ua.edu/research/castingproject.

3.0 Gap Formation Measurements

3.1 Synopsis

The continuing development of an inductive, eddy-current proximity sensor for non-contact measurement of the gap formation has been the focus of the third year of the project. The high temperatures (~1000 °F) encountered during the initial stages of the foundry pours have a significant effect on the output of the sensor. Five different sensor designs have been tested, each with a lower temperature sensitivity. Additional improvements in the sensor electronics allow for measurement of sensor coil resistance (which is a function of temperature only) as well as sensor coil inductance. Other improvements in testing hardware have lead to a "hot plate" test that allows for sensor calibration at elevated temperatures. Some limited results from foundry pours are presented, as well as preliminary results from green sand castings.

3.2 Technical Background

The layout of the experimental setup, used to measure the gap formation using the eddy current technique, is shown in the Figure 18. The eddy current sensor is buried in the sand mold and the molten aluminum is poured into the mold. The sensor initially registers the presence of the metal and gives an output of a particular frequency as a function of distance D_1. As the metal cools, the gap is (potentially) formed between the metal and the mold. The metal moves away from the sensor (denoted by D_2 in Figure 18) and the output of the sensor changes accordingly. The output of the sensor frequency and the time are recorded continuously. These data are correlated to the lab calibration data, and the formation of the air gap as a function of time is calculated. The difference between D_1 and D_2 will be the gap formed. Note that this assumes the only movement between the sensor and the casting is due to gap formation.

The simplest eddy current sensor is nothing but a coil of fine gage wire. Eddy current sensors are radio frequency (RF) inductive devices. A tuned RLC oscillator circuit is formed in part by the inductance of the sensor. Some authors use the term "impedance," which takes into account the resistance, capacitance, and inductance of the coil. When the coil of wire carrying a time-varying current is placed in the proximity of metals, an eddy current is induced in the material. Then there will be a pronounced change in the inductance of the coil, which in turn changes the frequency of oscillation of current. The magnitude of change of inductance depends on the factors like shape and size of the coil, number of turns of the wire wound, and the gage of the wire used.

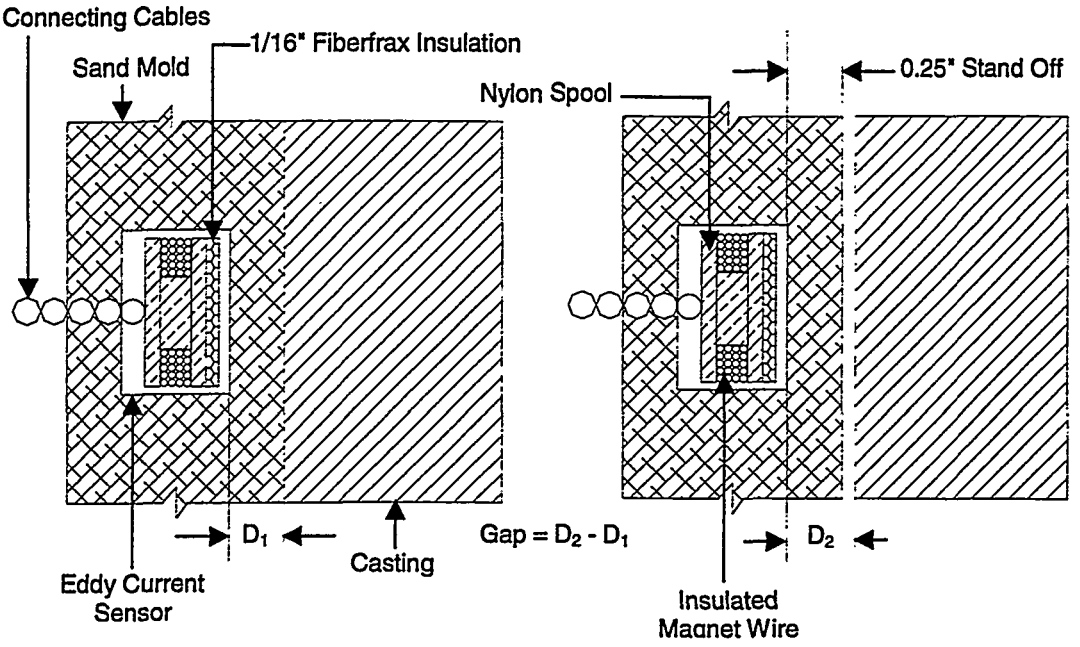

Figure 18. Eddy-Current Sensor Technique for Gap Measurement

The depth of penetration of eddy current on a conductive target is explained by the skin-effect principle, which states that an AC magnetic field penetrates a conductor approximately one skin depth, $\delta = 1/\sqrt{\pi\mu\sigma f}$, where μ is magnetic permeability of the conductor, σ is volume electrical conductivity of the conductor, and f is frequency. For aluminum, the skin depth is evaluated as shown below:

$$\mu_0 = \text{permeability of free space; } \mu_0 = 4\pi \times 10^{-7} \text{ H/m},$$
$$\mu_r = \text{relative permeability of aluminum; } \mu_r = 1,$$
$$\mu = \mu_0 \times \mu_r,$$
$$\sigma = 34.4 \times 10^6 \text{ S/m},$$
$$f = 48 \times 10^3 \text{ Hz}.$$

Substituting these values in the above equation, the skin depth, δ, for aluminum is 0.391 mm, which is nearly equal to 0.015 inch.

When a time-varying current is applied to coiled wire (sensor), a magnetic field is generated. When this sensor is brought near the conductive target, the magnetic field is disrupted. This generates "eddy" currents in the conductive target. These eddy currents generate their own magnetic field, which interacts with the original, modifying the inductance of the originating coil. The oscillation frequency of the RLC is therefore a function of the inductance, which is in turn a function of the distance from the conductive surface. The oscillation frequency of the RLC circuit is measured with a precision 10 MHz counter, and the resulting measurement is correlated to distance from the conductive surface by an extensive calibration process. As described in the previous annual report, a computer controlled, stepper motor driven slide with 0.00019 inch resolution/step is used to calibrate each proximity sensor coil in a repeatable fashion. The calibration test procedure is

1. "zero" the sensor coil by making contact with an aluminum target,
2. move the sensor coil away from the target by 5 to 20 steps (each step is about 0.0048 mm or 0.00019 inch),
3. wait for approximately 1 second, .
4. take 5-10 readings (~50 msec per measurement) from the frequency measuring circuit and record results in a data file,
5. record the actual position of the sensor with a digital dial indicator and record the position results in a data file,
6. repeat steps 2-5 until the sensor has traveled the length of the test range, then
7. repeat steps 2-6 as the sensor is moved back towards the target.

3.3 Proximity Sensor "Hot Plate" Calibration

Previously, all of the proximity sensors were calibrated (frequency vs. position) at room temperature only. Foundry tests have indicated an additional dependence of the sensor output on temperature. We have developed and conducted a "hot plate" calibration procedure. The faint "saw-tooth" waveform occurring within the first 400 samples is the proximity sensor output as it is moved approximately 2 mm (0.050 inch) away from the hot-plate surface in approximately 0.002 inch increments. The setup of the hot-plate calibration system is shown below in Figure 19. Results from one of several tests are shown in Figure 20. The proximity sensor is relatively insensitive to temperature changes up to an internal coil temperature of about 350 °F. Above this temperature, the proximity sensor output increases dramatically. The exact cause of this phenomenon remains unknown, but is believed to be related to the expansion of the copper wire that makes up the coil.

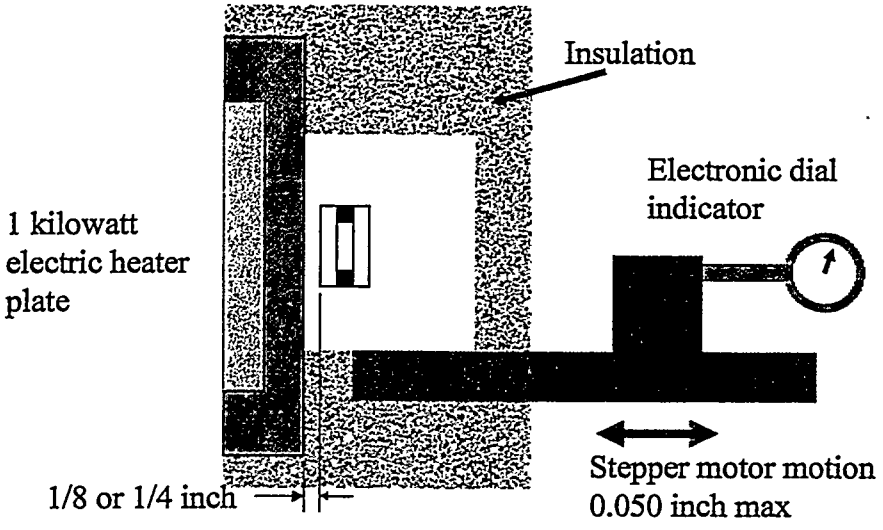

Figure 19. Hot-Plate Calibration Test Setup

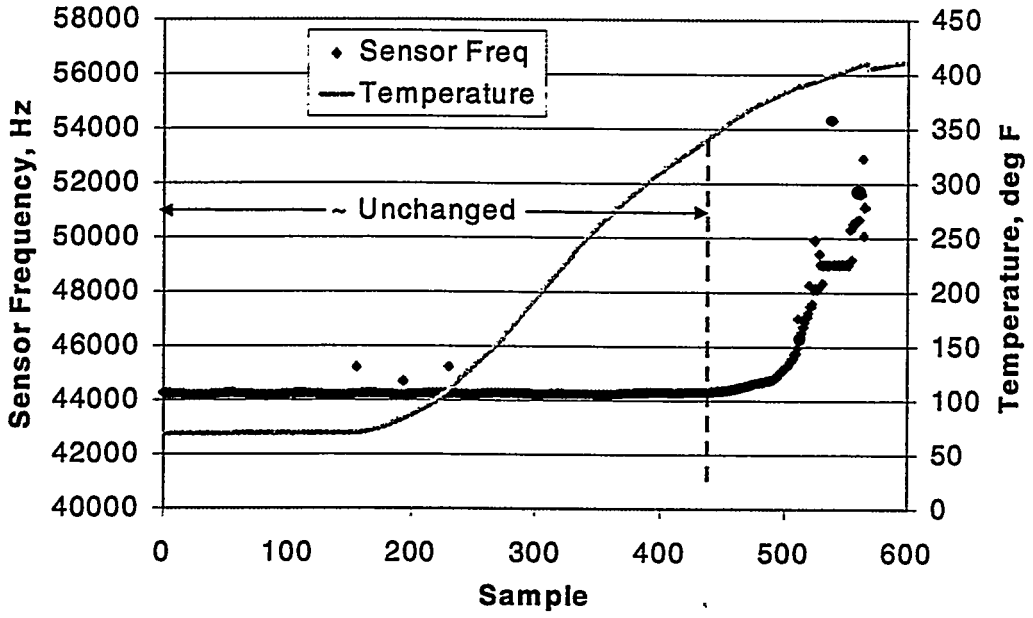

Figure 20. Hot-Plate Calibration Test Results

3.4 Proximity Sensor "Packs"

After several of the early foundry pours, the lab assistants noted that the proximity sensors were frequently found in a slanted or canted position. Since all of the calibrations were done with the sensor face perpendicular to the metal surface, this slant caused a major problem with the sensor operation. Based on this observation, we started installing the proximity sensors in a "sensor pack" similar to the one used to mount the thermocouples. The sensor is mounted uniformly and repeatably at 1/8 inch from the metal/sand interface. All of the proximity sensor tests since mid-December 1997 have used this new sensor pack configuration.

The "sensor pack" is nothing but the sensor surrounded by the sand that is used for making the mold. It is a 3-inch cube made out of sand with the sensor embedded in it. The sensor packs are made using a split wooden box with a bottom plate. The bottom plate is designed in such a way that it has a step of about 0.25 inch. The step fits into the split box. The wooden box can be split in the middle to facilitate easy removal of the sensor pack from it after the sand sets down. The sensor is placed in the split box as shwon in Figure 21. The sand is then put into the box and it is thoroughly packed. The box is then turned over and the bottom plate is then taken off. The sensor is then packed with sand from this side. The sand is then allowed to set for about 10 minutes. The sensor pack is then taken off from the split box, as shown in Figure 22. Now the sensor is ready to be placed in the mold cavity. The finished sensor pack is shown placed in the mold in Figure 23.

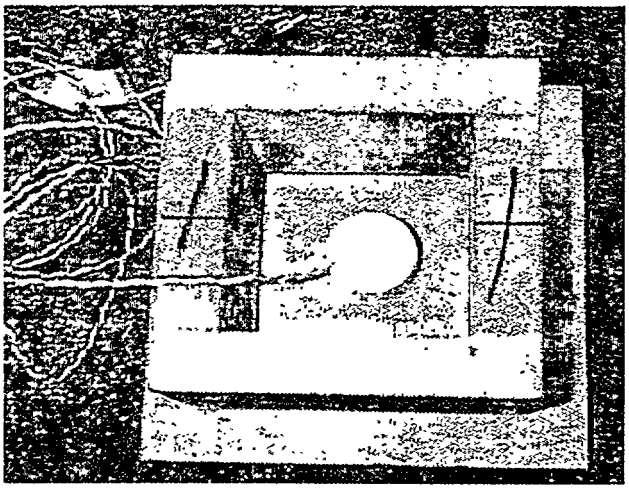

Figure 21. Positioning of the Sensor in the Split Box

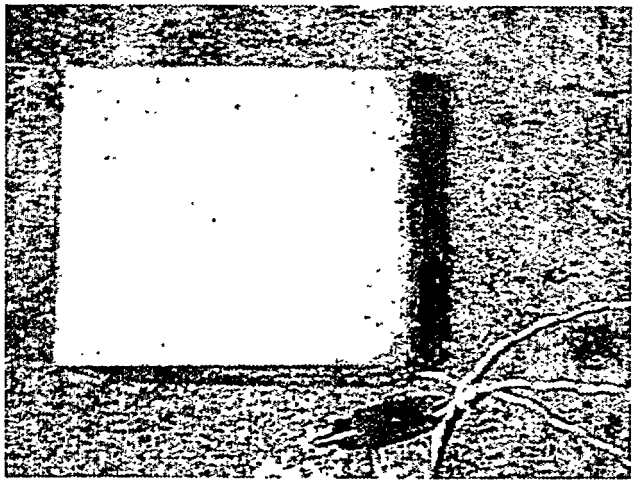

Figure 22. Finished Proximity Sensor Pack

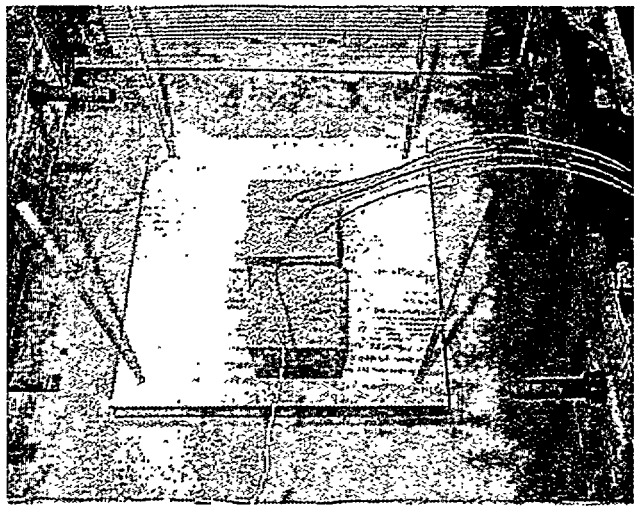

Figure 23. Placing of the Sensor Pack in the Mold

3.5 Proximity Sensor Development

The observed results from several foundry pours clearly indicated a significant temperature effect on the proximity sensor output. This observation has lead to the development of five new sensor designs with lowered temperature sensitivity. The first modification incorporates an insulating air gap between the sensor coil and the ceramic housing, as shown in Figure 24. Results from one of the calibration tests (over a 0.050 inch range) is shown in Figure 25. The hot plate was turned on at about the 150 sample point, and its temperature was increased to 900 °F. The proximity sensor remains relatively insensitive to temperature changes up to an internal coil temperature of about 300 °F. However, there is no drastic change in the sensor output at the 350 °F point, as seen in the earlier foundry results. The air gap appears to be somewhat effective in extending the time frame over which the proximity sensor would work in the foundry pours. Ultimately this approach was abandoned due to the difficulty in fabricating the air gap sensor.

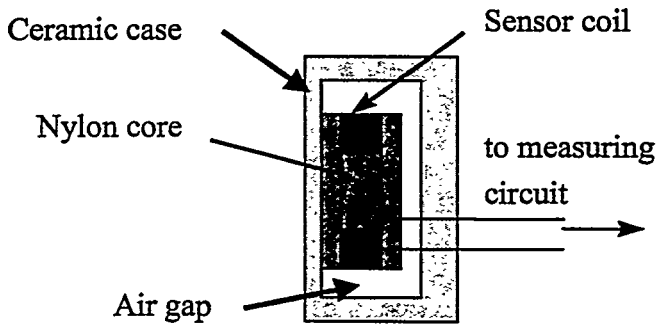

Figure 24. Air Gap Sensor

A second modified proximity sensor design uses 200 turns of 36 gauge wire with a thicker Teflon® insulation rated to 200 °C (the normal sensor uses 500 turns of 34

gauge wire with an insulation rated to 180 °C). The smaller number of turns is due to the increased thickness of the Teflon® insulation. Results from a hot plate calibration test are shown in Figure 26. Note the higher operating frequency of the sensor – this is due to the lower coil inductance created by having only 200 turns of wire on the coil. The calibration test was conducted in a similar fashion to the one discussed above. Note that similar results were obtained in that no large temperature effect on the sensor was observed. This may be due to the fact that the sensor did not reach the critical 350 °C temperature due to the thicker wire insulation. A small temperature effect on the sensor output can be observed in Figure 26. For this sensor, the 0.050 inch calibration "stroke" gives a sensor output change on the order of 400 Hz. The 175 °F internal coil temperature increase gives a sensor output change on the order of 2600 Hz – about 6-7 times that of the calibration stroke. This sensor design was also ultimately abandoned due to the difficulty in fabricating and handling the sensor with the extremely fragile 36 gauge wire.

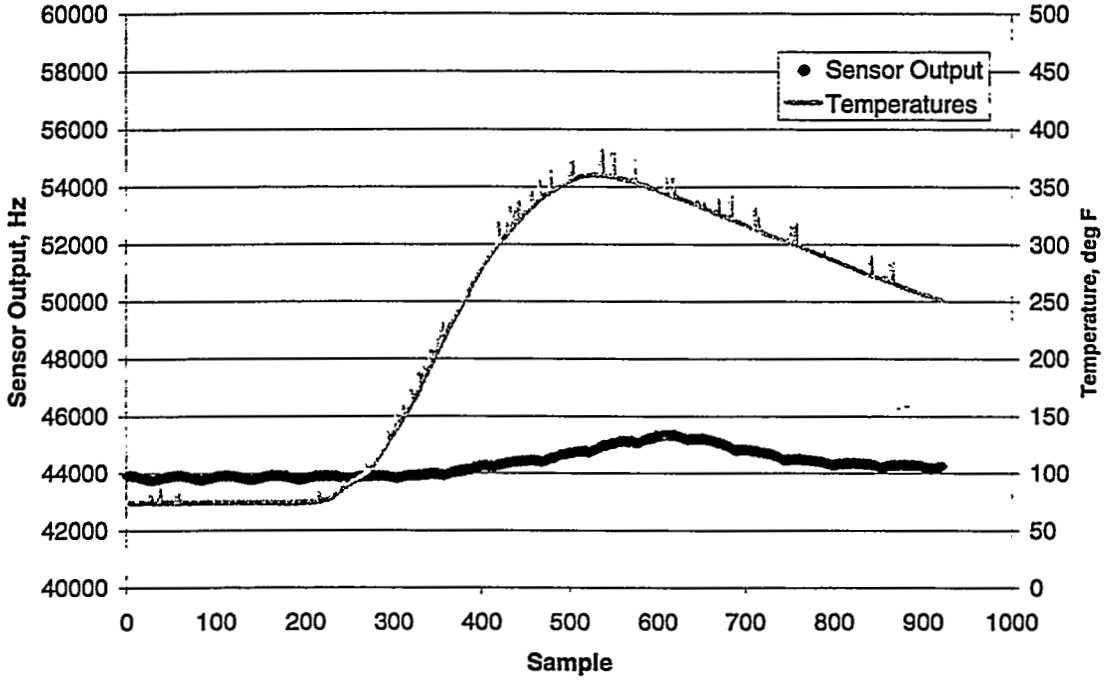

Figure 25. Hot Plate Test - Air Gap Sensor

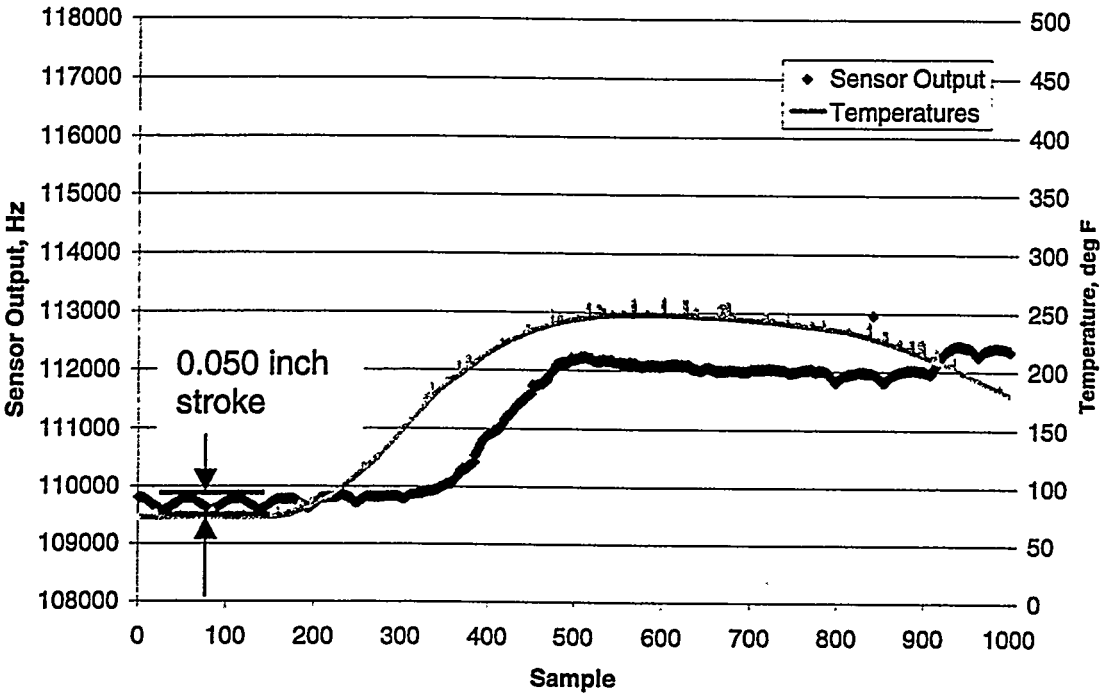

Figure 26. Hot Plate Test – 36 Gauge Sensor

The results from the second sensor design with higher temperature rated insulation looked promising. Three additional types of magnet wire with higher rated insulation were purchased:

- #34 AWG HAPT Class 200C magnet wire (MWS Wire) – rated to 200 °C
- #34 AWG HML Class 220C magnet wire (MWS Wire) – rated to 220 °C
- #33 AWG Heavy Allex magnet wire (Essex Express) – rated to 220 °C.

Proximity sensors were wound and tested from the first two types of magnet wire listed above. The third type of high temeperature wire (#33 AWG Heavy Allex) was not tested extensively. The heavier gauge wire allowed only 275 turns on the standard spool, which greatly reduced the sensor's sensitivity.

Static hot-plate (laboratory) test results for the other two types of wire are shown below in Figures 27 and 28. In this test the hot plate was maintained at 900 °F. A proximity sensor mounted in the sand pack was then placed on the hot plate. The sensor is then heated by the direct contact between the sand pack and the hot plate. As shown in the figures below, both types of wire have greatly extended temperature ranges over the standard 180 °C wire that has previously been used. The 200 °C rated wire allows more turns (500 vs. 450) than the 220 °C rated wire due to the slightly thinner insulation. This larger number of turns gives a better position (gap) sensitivity.

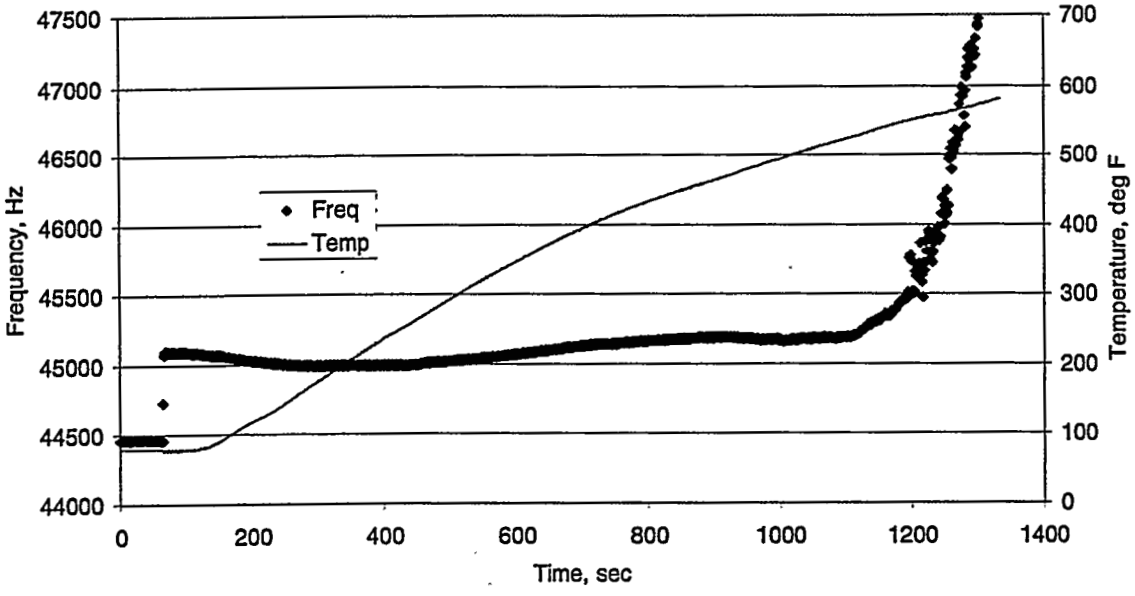

Figure 27. Hot Plate Test Results (34 ga wire, 200 °C Rating)

The fifth (and final) experimental proximity sensor design uses a 1/16 inch (1.6 mm) thick sheet of Cotronics #300-40 ceramic paper inserted between the nylon sensor spool and the face of the ceramic casting of the proximity sensor, shown in Figure 29. This ceramic paper has a rated thermal conductivity of approximately 0.38 – 0.60 Btu/hr-ft^2-°F/in, which is 10% of the Cotronics Rescor 750 ceramic. The ceramic paper insulation is used instead of the air gap insulation, which proved to be too difficult to manufacture repeatably. Figure 30 shows a hot plate test for a proximity sensor made in this configuration. The slope of the temperature line is less than that of Figure 28, which indicates that the ceramic paper is somewhat effective in reducing the temperature rise of the proximity sensor. This is the final proximity sensor design and has been used continuously since May 1998.

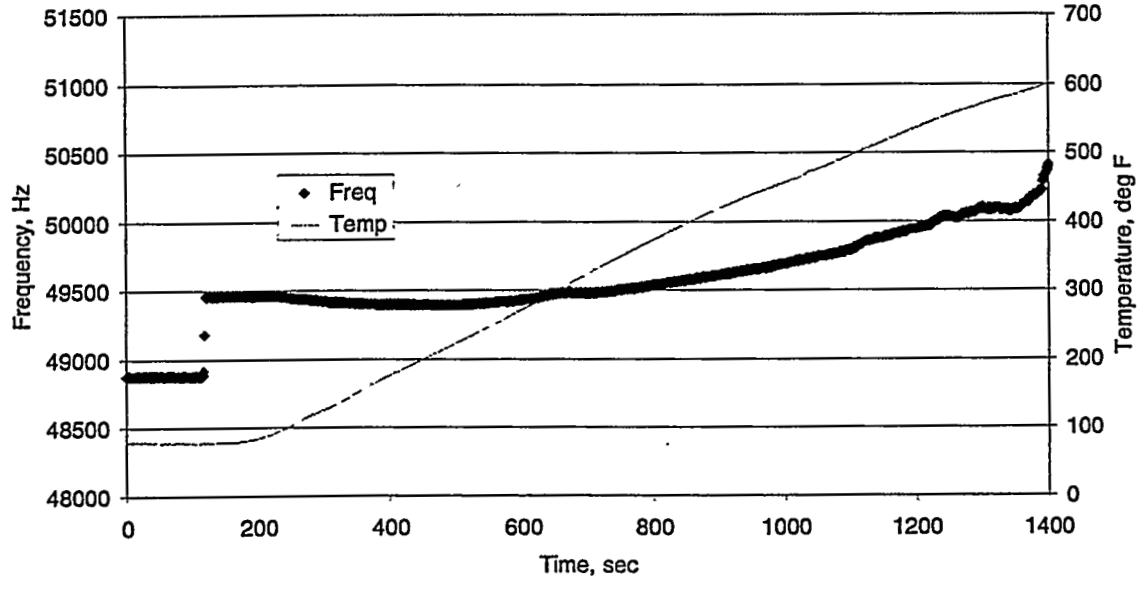

Figure 28. Hot Plate Test Results (34 ga wire, 220 °C Rating)

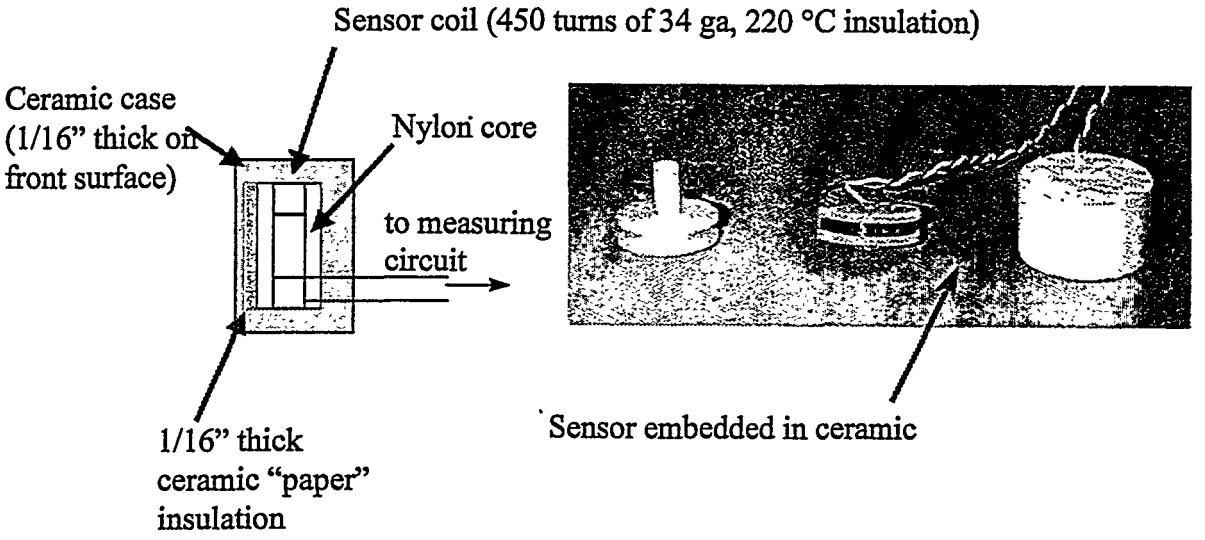

Figure 29. Latest Eddy-Current Proximity Sensor Design

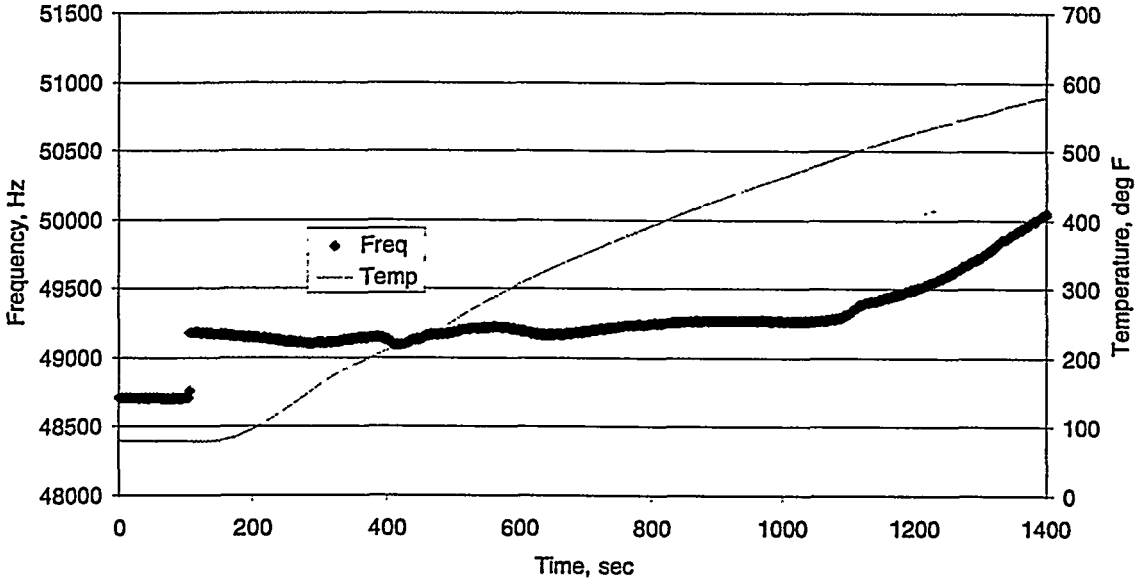

Figure 30. Hot Plate Test Results (34 ga wire, 220 °C Rating, Ceramic Paper Insulation)

In June 1998 a series of laboratory hot plate calibration tests uncovered a phenomenon that had occasionally corrupted our proximity sensor results for several months. A proximity sensor mounted in a sand pack was placed on the hot plate. The sensor was then heated by the direct contact between the sand pack and the hot plate. As shown in Figure 31, on the first test a rapid increase in the sensor output occurred at a sensor temperature of about 200-220 °F. The same sensor pack was tested on the following day (2nd Test), and the sensor output "spike" at these temperatures was not present. We believe that sometimes there is residual moisture in the ceramic material surrounding the proximity sensor coil that causes this output spike. Since this discovery

in early June 1998, we instituted a curing cycle to thoroughly dry the sensors before using them in the lab or the foundry. A representative foundry test (1/2 inch plate thickness, 45 degree angle) is shown in Figure 32. Close observation of the temperature profile indicates that there is a small change in slope just below the 200-220 °F point, which indicates that the sensors were still not entirely dry even after the curing process.

Sensor "curing" tests developed during early June 1998 were conducted with a vent hole present in the sensor. This vent hole allowed moisture from the curing ceramic to escape from the sensor. Thermo-gravimetric testing results for the curing process are shown below in Figure 33. The "unplugged" sensors have the vent hole and are clearly more thoroughly dried than the "plugged" sensors without the vent. The importance of this curing process detail was not communicated adequately to the graduate student that made the sensors used in subsequent foundry tests. All sensors fabricated after the third week of July 1998 have had the curing process conducted in the "unplugged" state.

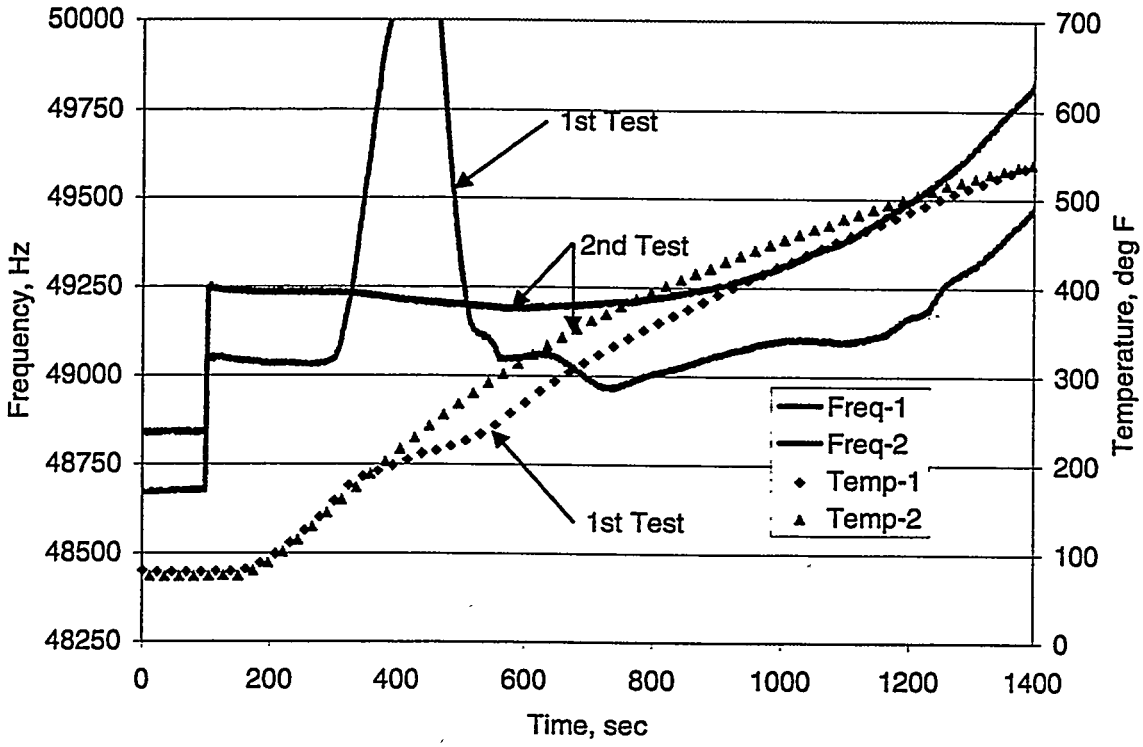

Figure 31. Hot Plate Test Results, Sensor #527-1

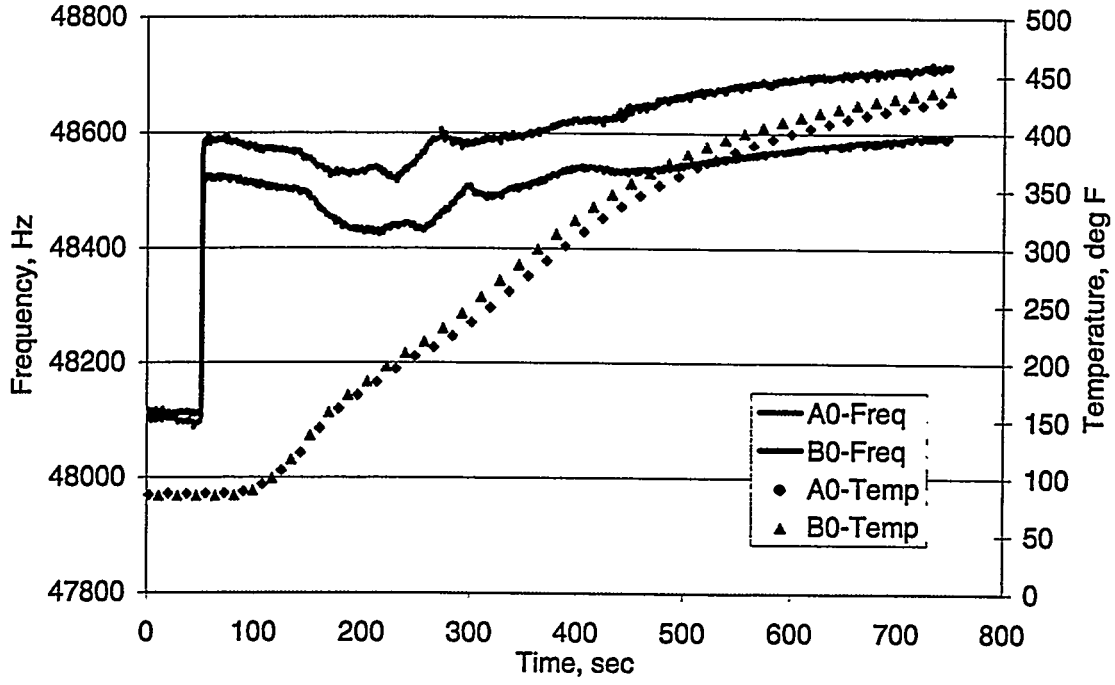

Figure 32. Foundry Test, 6/24/98 (1/2 inch plate, 45 degree angle)

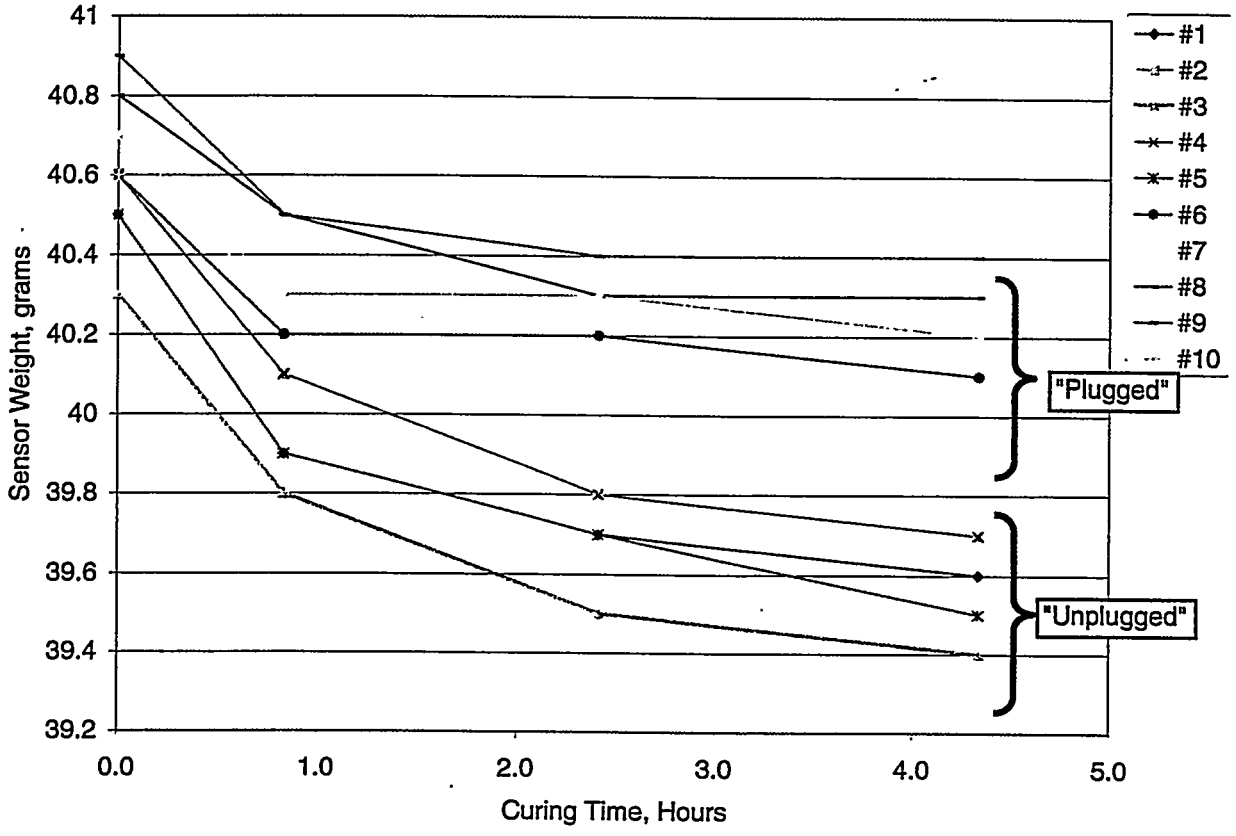

Figure 33. Thermo-gravimetric Testing Results

3.6 Temperature Calibration / Correction

Figures 34 and 35 illustrate the current status of the temperature correction effort with the current ceramic paper insulated proximity sensors. Figure 34 shows a typical hot-plate position calibration test. The saw-tooth waveform is the proximity sensor output as it is moved 0.080 inch away from the hot-plate surface in approximately 0.002 inch increments. Note that the waveform dips slightly as the sensor heats in the 100-200°F range. As the sensor heats further, the output begins to increase gradually. At a coil temperature of approximately 450-475°F, the sensor output begins a large increase.

The sensor data from Figure 34 and several other similar tests were least-squares fitted to a function of the form given below:

$$f = f_0 + p_1 D + p_2 D^2 + ct_1 T_C + ct_2 T_C^2 + hp_1 T_{HP} + hp_2 T_{HP}^2$$

where

f = measured sensor output (Hz),
D = sensor displacement from hot plate surface (inch),
T_C = measured coil temperature (°F), and
T_{HP} = measured hot plate temperature (°F).

The remaining terms in the equation $(f_0, p_1, p_2, ct_1, ct_2, hp_1, hp_2)$ are the coefficients determined by the least-squares curve fit equation. Figure 35 shows the results of applying the curve fit equation to the original data. The fitted data agrees with the original data reasonably well, except at the 400 sample point where the hot plate temperature increased rapidly. Most of the differences are within ± 10Hz.

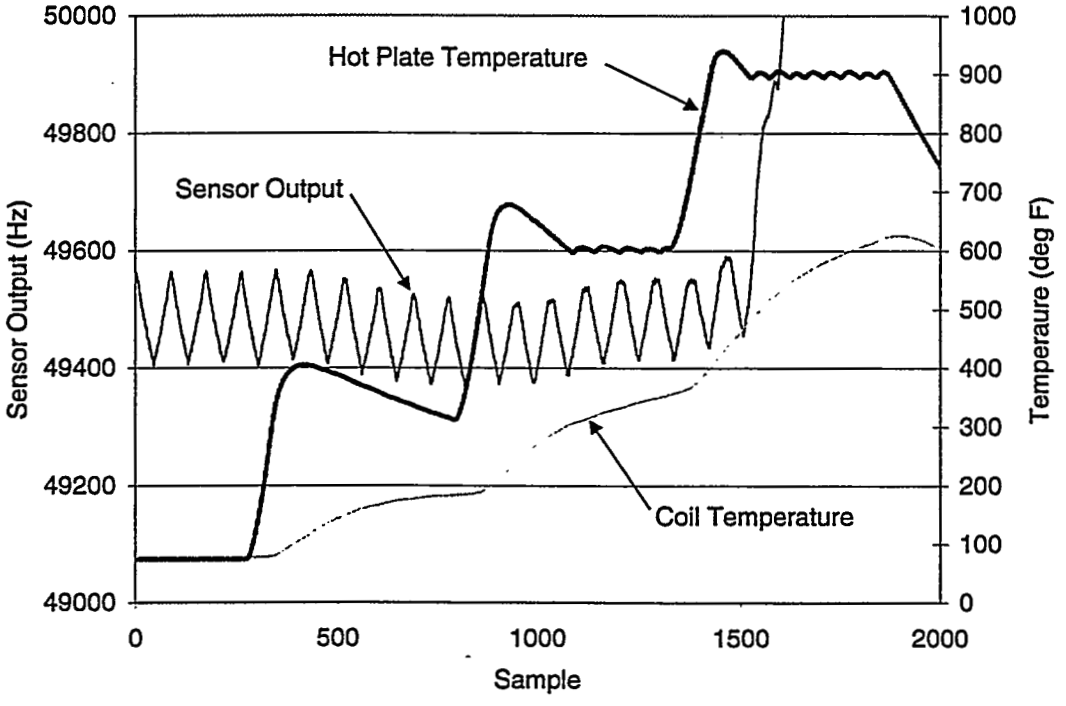

Figure 34. Position-Temperature Calibration, 8/2/98, 1/4" Stand off

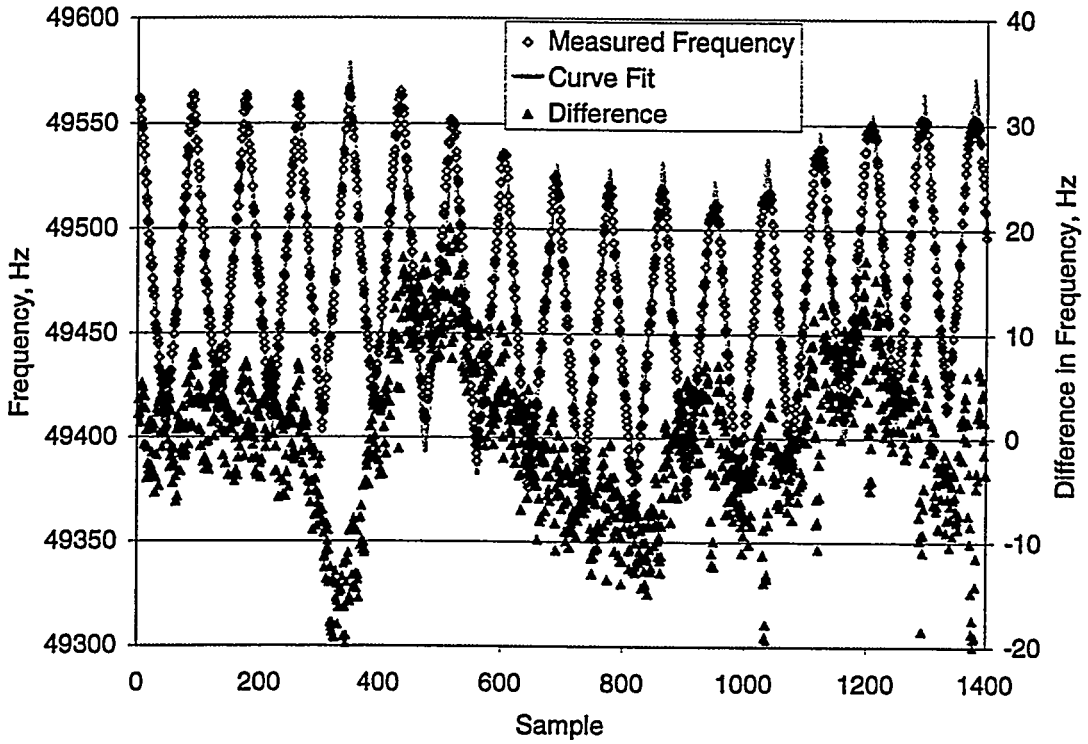

Figure 35. Temperature Correction Curve Fit

3.7 Frequency / Resistance "Switching" Circuit

As discussed in the previous section, temperature has a significant effect on the output of the proximity sensor coil. The resistance of the copper magnet wire used to form the sensor coil has a well-known dependence on temperature. A special sensor coil was instrumented with four thermocouples in order to correlate coil temperature with the wire resistance. An amplified Wheatstone bridge measuring circuit was constructed and used in the testing of the temperature effects on the coil. The Wheatstone bridge converts the small resistance changes in the coil to voltage changes, which are then amplified by a differential op-amp circuit. In this test the instrumented coil was held stationary approximately 3 mm (1/8 inch) away from an electrically heated aluminum plate. The heater was turned off when the plate reached approximately 100 °F. After a few minutes, the heater was again turned on until a temperature of 200 °F at the heater plate surface was reached. The bridge voltage very closely tracked the average temperature measured with the four thermocouples. The results of these tests indicate that measurements of the resistance of the proximity sensor coil can be used to determine the coil's temperature.

The current concept for the proximity sensor system is to measure both inductance (which is a function of the gap and the coil temperature) and the coil's resistance (which is a function of the coil temperature alone). This requires a "switching" circuit which alternately connects the proximity sensor coil to the inductance and resistance measuring circuits A new set of sensor electronics was designed, fabricated, and tested in both the lab and the foundry. The new electronics use much smaller electromechanical relays mounted near the sensors. This arrangement greatly reduced the "crosstalk" between the two sensors mounted in the same casting. It also greatly reduced the noise induced in the temperature readings used for heat flux calculations. A final benefit was that a total of four sensors could be measured simultaneously (up from the previous two), which improved productivity in the foundry pours.

3.8 Gap Formation Results - Foundry Pours

Figure 36 shows the results for both gap formation and heat flux from a typical foundry pour. The gap is determined by subtracting the initial position of the sensor (D_0) from the current position (D_i). The measured gaps were corrected using the average values for the temperature-related coefficients (ct_1, ct_2, hp_1, hp_2) in the least-squares curve fit equation. The gap values are positive ($D_i > D_0$) for the first 250 seconds after the pour, then both become negative. A negative value for the gap ($D_i < D_0$) would mean that the sensor has moved closer to the casting surface. The relatively large maximum gap values of -0.030 inch for the bottom sensor and -0.050 inch for the top sensor do not seem reasonable. Results from several other foundry test pours show the same general trends.

One potential reason for the gap results shown in Figure 36 can be explained by static hot plate test results shown in Figure 37. In this figure the frequency and coil temperatures are plotted for three sensors. Each was installed in the standard sensor pack with a 1/4 inch stand-off distance. The sensor pack was placed on the pre-heated hot plate and then surrounded by insulation. The hot plate temperature was maintained at a relatively constant 900 °F throughout the test.

The output from all three sensors begins to drop essentially immediately after placement on the hot plate. The temperature of the coil does not begin to rise until 50-75 seconds into the test. Since both the hot plate and the coil temperatures are constant during this initial period, the physical expansion of the sand must cause the lower sensor readings. If this is true, then the temperature corrections described above must be modified accordingly.

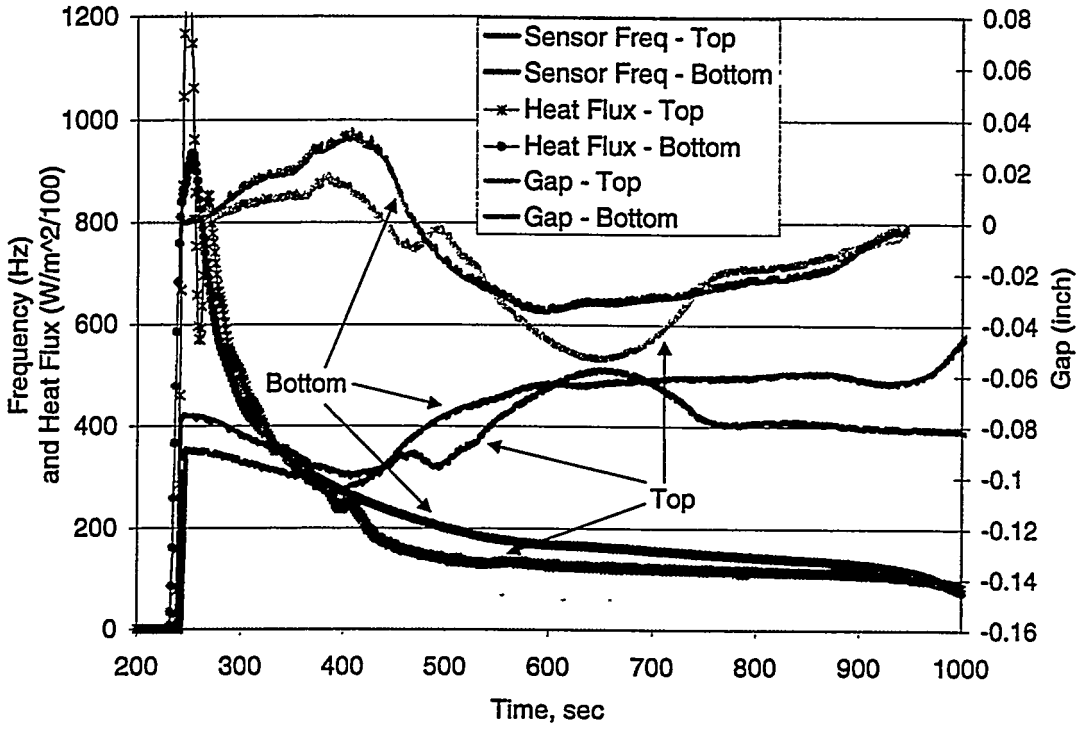

Figure 36. Foundry Test, 8/13/98 (1 inch, Horizontal)

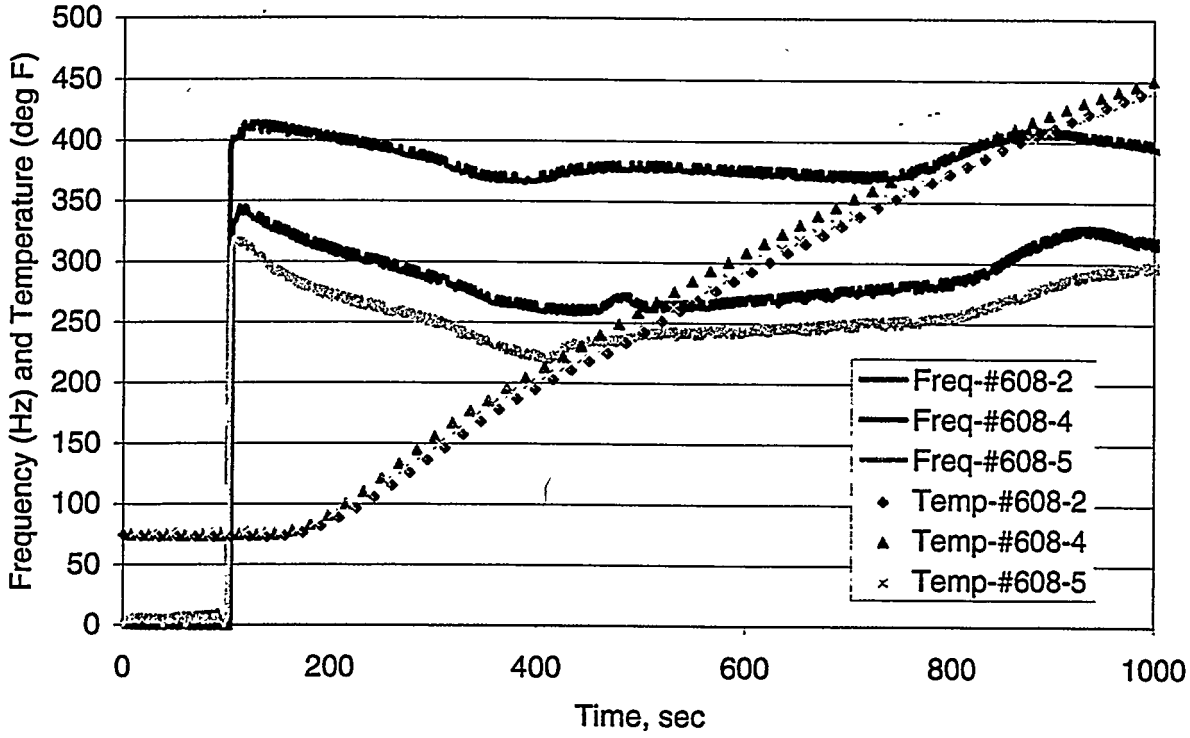

Figure 37. Static Hot Plate Tests

3.9 Green Sand Results

We have also conducted preliminary green sand tests with the proximity sensor. Figure 38 shows the results of a hot-plate calibration test. The green sand shows the same general results as the resin-bonded sand – very little temperature effect up to about 350 °F, then a very large effect.

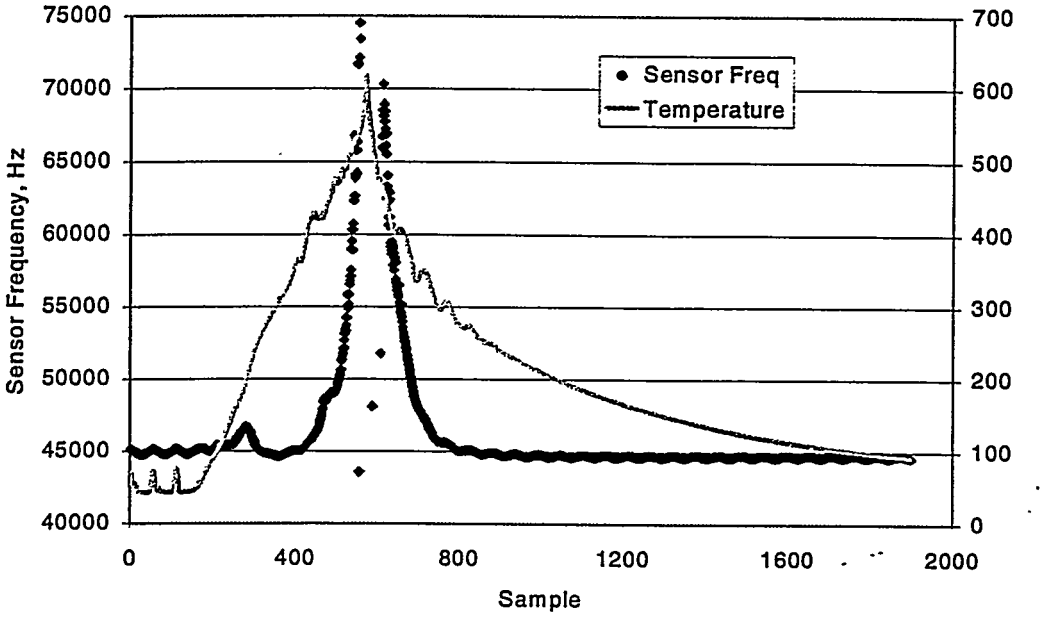

Figure 38. Hot-Plate Calibration Test Results – Green Sand

[1] G. DiSylvestro, "Dimensional Stability of Castings Made in High Density Green Sand Molding: Phase I – Factors Which Affect Dimensional Stability," *AFS Transactions,* vol. 85 (1977), p. 745.
[2] J. Campbell, *Castings*, Butterworth-Heinemann Ltd.,Oxford, UK, 1992, p. 128.
[3] K.A. Woodbury, J.K. Parker, T.S. Piwonka and Y.A. Owusu, "Relationship Between Casting Distortion, Mold Filling and Interfacial Heat Transfer," Report DOE/ID/13363/1, Report DOE/ID/2.
[4] K.A. Woodbury, Y. Chen, J.E. Parker and T.S. Piwonka, "Measurement of Interfacial Heat Transfer Coefficients between Aluminum Castings and Resin-bonded Sand Molds," *AFS Transactions,* vol. 106 (1998), p. 705.
[5] K.A. Woodbury, Y. Chen, and Q. Ke, "Determination of Interfacial Heat Fluxes During Casting of Aluminum in Resin Bonded Sand Molds," *Proceedings of the ASME Heat Transfer Division, Volume 5*, (1998 ASME IMECE), Nov. 1998, p. 153.
[6] J.V. Beck, B. Blackwell and C. St. Clair, *Inverse Heat Conduction: Ill-posed Problems,* Wiley, 1985.

SECOND YEAR REPORT

STATISTICAL ANALYSIS OF GEOMETRIC TOLERANCES OF CASTING PRODUCTS USING POINT CLOUD DATA GENERATED BY COORDINATE MEASUREMENT MACHINE (CMM)

Yaw A. Owusu, PhD
Associate Professor & Fulbright Fellow
Department of Industrial Engineering
FAMU-FSU College of Engineering
Florida A & M University-Florida State University
2525 Pottsdamer Street
Tallahassee, Florida 32310-6046

ABSTRACT

This report presents a statistical method of evaluating geometric tolerances of casting products using point cloud data generated by coordinate measuring machine (CMM) process. The focus of this report is to present a statistical-based approach to evaluate the differences in dimensional and form tolerances of casting products as affected by casting gating system, molding material, casting thickness, and casting orientation at the mold-metal interface. Form tolerances such as flatness, parallelism, and other geometric profiles such as angularity, casting length, and height of casting products were obtained and analyzed from CMM point cloud data.

In order to relate the dimensional and form errors to the factors under consideration such as flatness and parallelism, a factorial analysis of variance and statistical test means methods were performed to identify the factors that contributed to the casting distortion at the mold-metal interface. The results of some of the statistical analyses have been provided, though not conclusive because some more analyses are still been done.

This research work was funded by US Department of Energy (DOE) and American Foundrymen's Society. The research was carried out jointly by University of Alabama in Tascaloosa, Florida A & M University in Tallahassee, General Motors Company, Mercury Marine Company, Willard Industries, and CMI Test Center.

STATISTICAL ANALYSIS OF GEOMETRIC TOLERANCES OF CASTING PRODUCTS USING POINT CLOUD DATA GENERATED BY COORDINATE MEASUREMENT MACHINE (CMM)

1.0 INTRODUCTION

In general, manufactured parts have deviations in size, form and geometrical relations from their nominal design. The designer specifies the zone tolerance within which the feature is contained using standards such as American National Standard Institute (ANSI), and International Standard Organization (ISO).

Form tolerances state how far the actual features are permitted to vary from the designed nominal form. Standard form includes: lines, planes, circles, and cylinders. Non-standard form features include curves and free-form surfaces. The corresponding form tolerances are defined as straightness, flatness, circularity (roundness), cylindricity, and profile of curves or surfaces. To evaluate an error, an ideal feature must first be established from the actual measurements such that deviations of the feature can be obtained. In general, form features and errors can be expressed as follows

$$X(\theta) = N(\theta) + \varepsilon(\theta) \qquad (1)$$

where θ is a set of independent variables, $X(\theta)$ is the measurement value at θ, $N(\theta)$ is the ideal value of the form feature at θ, and $\varepsilon(\theta)$ is the deviation at θ [Menq, 1990]. The ideal form can be the nominal design value or the best least-square fit. For CMM sampling, the

corresponding θ_i for each point is not really known. Therefore, the deviation of a sample point is minimized by

$$|\varepsilon_i| = \min |X_i - N(t,\theta)| \qquad (2)$$

where the point error ε_i is found minimizing the difference between the measured value X_i and the nominal value $N(t,\theta)$, and t represents the tolerance allowed in the design. In this research, the geometrical features of interest for the statistical analysis were: length and height, surface flatness, parallelism of planes, and tapered angles (angularity of a side plane).

2.0 THEORY AND STATISTICAL EVALUATION OF DIMENSIONAL AND TOLERANCES FOR CMM POINT CLOUD DATA

2.1 Linear Dimensions

The Euclidean distance or linear distance between two coordinate points (x_1, y_1, z_1) and (x_2, y_2, z_2) is calculated using the following expression

$$DIST = SQRT[(x_2 - x_1)^2 + (y_2 - y_1)^2 + (y_2 - y_1)^2] \qquad (3)$$

In this expression, DIST is the desired linear distance, SQRT is the square root, X, Y, Z are the coordinates for the points 1 and 2 represented by their subscripts. This formula was used to compute the distances to evaluate the linear dimensions (i.e. length height, thickness, etc.) as well as the tapered angle and the distance between the internal walls of the casting.

2.2 Surface Flatness Evaluation

With sampled inspection, every point on the surface cannot be measured. Therefore, it is necessary to infer the likelihood of a straight surface from the data. In this case if any point is outside the tolerance, the surface is not considered flat since it is assumed that the CMM machine has negligible measurement error. If all the sample points are within the tolerance limit that does not necessarily mean that the surface is flat because only a few sampled points of the feature are taken. Consequently, the variance of the sample points must be examined to see if the variation of the surface is good enough. This examination is based on a hypothesis test:

$$H_0 = \sigma = \sigma_m \tag{4}$$

and

$$H_1 = \sigma = \sigma_t \tag{5}$$

The null hypothesis states that the feature variation, σ, equals the expected variation σ_m of the process in control, while the alternative hypothesis states that the feature error reaches the tolerance limit. Therefore, a critical value (L) must be defined and set up such that if

$$s \leq L \text{ (Accept)}$$

and

$$s > L \text{ (Not Accepted).}$$

The selection of L along with the estimator s (sampled deviation) provides sufficient confidence in the test such that

$$P(s \leq L \mid \sigma = \sigma_m) = 1 - \gamma \quad (6)$$

$$P(s > L \mid \sigma = \sigma_t) = 1 - \delta. \quad (7)$$

where γ is the risk of rejection of a surface that is good and δ is the risk that a bad surface is accepted. Figure 1 illustrates this.

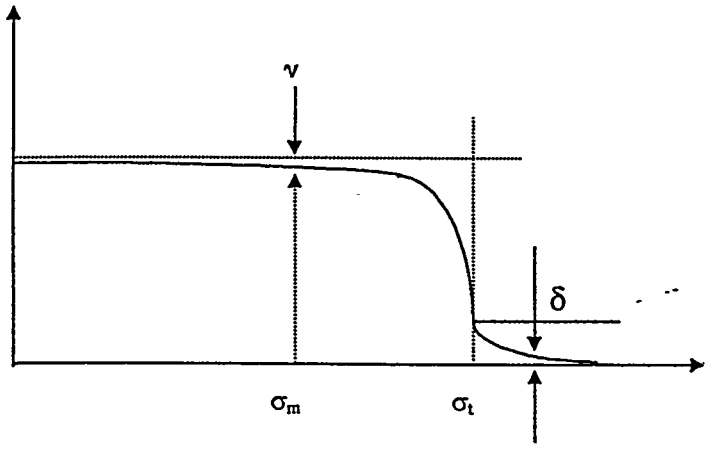

Figure 1. Sampling Plan Based on Operating Characteristic Curve [Menq, 1990].

The relation between the sample variance s^2 and the true variance is given by

$$\chi_n^2 = ns^2/\sigma^2 \quad (8)$$

where χ_n^2 is a chi-square distribution with n degrees of freedom. Therefore the equation (6) becomes

$$P(s^2 \le L^2 \,|\, \sigma = \sigma_m) = P(\chi_n^2 \le L^2 n/\sigma_m^2) = 1 - \gamma \qquad (9)$$

which gives

$$L^2 = (\chi^2_{n:\gamma}\, \sigma^2_m)/n \qquad (10)$$

Similarly equation (7) becomes

$$P(s^2 > L^2 \,|\, \sigma = \sigma_t) = P(\chi_n^2 \le L^2 n/\sigma_t^2) = 1 - \delta \qquad (11)$$

and

$$L^2 = (\chi^2_{n:1-\gamma}\, \sigma^2_t)/n. \qquad (12)$$

Equating equations (10) and (12), the following expression is obtained:

$$(\chi^2_{n:\gamma}/\chi^2_{n:1-\gamma}) = (\sigma_t/\sigma_m). \qquad (13)$$

Knowing that for $n \ge 30$, the quantity $\sqrt{2\chi_n^2}$ is distributed approximately as a normal variable with mean of $\mu = \sqrt{2n}$ and variance of $\sigma^2 =$ unity [Bendat and Piersol, 1983], and

$$\sqrt{2\chi^2} = \sqrt{2n}\frac{s}{\sigma} \rightarrow N(\sqrt{2n},\ 1) \qquad (14)$$

and having

$$z = \frac{s - \sigma}{\sigma/\sqrt{2n}} \qquad (15)$$

and

$$s = \frac{s\sigma}{\sqrt{2n}} + \sigma. \qquad (16)$$

Therefore,

$$P(s^2 \le L^2 \mid \sigma = \sigma_m) = P(z \le \frac{L - \sigma_m}{\sigma_m / \sqrt{2n}}) = 1 - \gamma \quad (17)$$

and

$$L = \frac{z_\gamma \sigma_m}{\sqrt{2n}} + \sigma_m. \quad (18)$$

Let $\sigma_t = k\sigma_m$, $(k > 1)$, where k is the process capability ratio.

$$P(s^2 > L^2 \mid \sigma = \sigma_t) = P(z > \frac{L - k\sigma_m}{k\sigma_m / \sqrt{2n}}) = 1 - \delta \quad (19)$$

and

$$L = \frac{z_{1-\delta} k\sigma_m}{\sqrt{2n}} + k\sigma_m \quad (20)$$

Equating equations (18) and (19), the relationship is obtained between sample size and process capability given that the process is normally distributed, such that

$$n = \frac{1}{2}\left[\frac{kz_{1-\delta} - z_\gamma}{1-k}\right]^2 \quad (21)$$

and the critical value L becomes

$$L = \frac{(1-k)z_\gamma \sigma_m}{kz_{1-\delta} - z_\gamma} + \sigma_m \quad (22)$$

Figure 2 shows the relationship between the sample size and the process capability. When the process capability is high the sample size can be greatly reduced to estimate the value of the form tolerance.

2.3 Evaluation of Parallelism of Geometric Surfaces

The evaluation of parallel surface is accomplished by finding the distance between the points on opposite locations on the planes that are being evaluated. From the measured distances, the difference between the shortest distance and the longest distance gives the parallelism error ($\varepsilon_{parallelism}$). Mathematically, it is expressed as

$$\varepsilon_{parallelism} = \max(dist_{AB}) - \min(dist_{AB}) \tag{23}$$

where $\varepsilon_{parallelism}$ is the difference between the maximum distance between planes A and B. The distance is computed using equation 3. Figure 3 illustrates the parallelism error between two planes.

2.4 Calculation of the Tapered Angle

The casting tapered angle was calculated using the Euclidean distance, equation 3, and the trigonometric relation:

$$\cos\theta = \frac{\sqrt{(x_1 - x_0)^2 + (y_1 - y_0)^2 + (z_1 - z_0)^2}}{\sqrt{(x_4 - x_3)^2 + (y_4 - y_3)^2 + (z_4 - z_3)^2}}. \tag{24}$$

These angles are based on the assumption that the walls of the casting are fairly straight. A tolerance of ± 0.5 degrees was used.

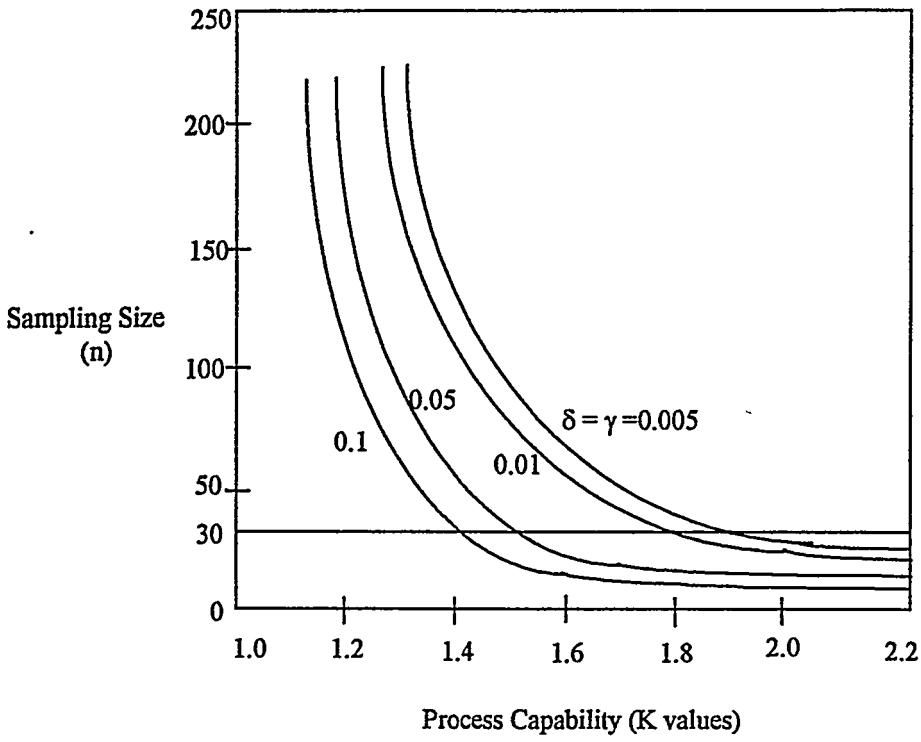

Figure 2. Sampling Size vs. Process Capability [Menq *et al.*, 1990].

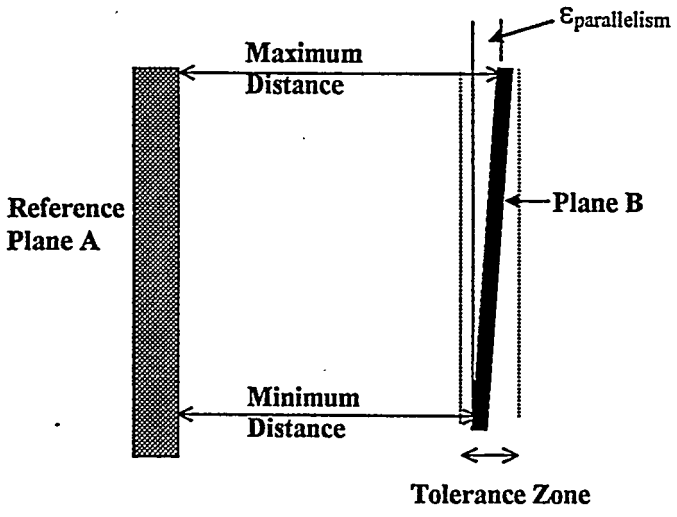

Figure 3. Parallelism Error between Two Planes.

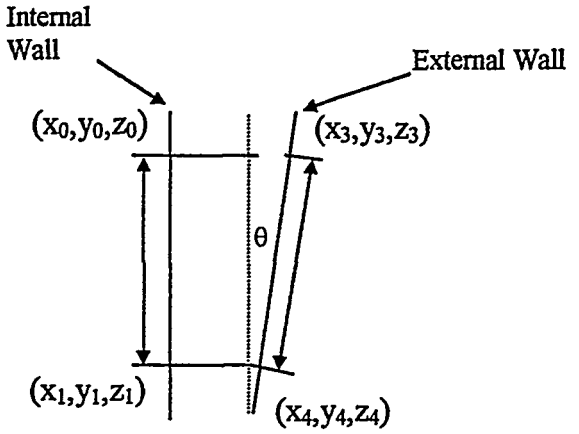

Figure 4. Parameters to Compute Tapered Angle.

2.5 Analysis of Variance

Analysis of variance (ANOVA) procedures separate the variation observable on a response into two basic components: variation due to assignable causes and random or chance variation. Assignable causes refer to known or suspected sources of variation, which could be corrected during the conduct of the experiment. Random or chance variation includes the effects of all other sources that could not be controlled or measured during the experiment except by statistical modeling. Therefore, the statistical model for the sand casting dimensional data are:

$$y_{ijklr} = u_{ijkl} + e_{ijkl,} \qquad (25)$$

In this equation, y_{ijklr} is the measured dimensions of the sand casting due to the different factor level combinations. The number of repeat tests are represented by $r = 1, 2, 3$. The levels for the molding method are represented by $i = 1, 2, 3, 4$. Similarly, $j = 1, 2, 3$; $k = 1, 2, 3$; $l = 1, 2, 3$, represent the levels for the gating system, the casting

orientation and thickness respectively. In this model u_{ijkl} is the effect of the assignable causes and e_{ijkl} is the random error of the experiment.

The assignable cause portion of the model can be further decomposed into terms representing the main effects and the interactions among the four model factors

$$\mu_{ijklr} = \mu + \alpha_i + \beta_j + \gamma_k + \delta_l + (\alpha\beta)_{ij} + (\alpha\gamma)_{jk} + (\alpha\delta)_{kl} + (\beta\gamma)_{ik} + (\beta\delta)_{jl} + (\gamma\delta)_{kl} + (\alpha\beta\gamma)_{ijk} + (\alpha\beta\delta)j_{kl} + (\beta\gamma\delta)_{ikl} + (\alpha\beta\gamma\delta)_{ijkl} \quad . \qquad (26)$$

The subscript i in (26) represents one of the levels of the molding material, the subscript j to one of the levels of the gating system, the subscript k to one of the orientations, the subscript l to one of the levels of the thickness, the r the three repeat tests.

The parameters in (26) having a single subscript represent main effects for the factor identified by the subscript. Two-factor interactions are modeled by the terms having two subscripts, and the three-factor interaction by terms having three subscripts. The first term in the equation (26) represents, the over all response mean.

The interaction components in (26) model joint effects that cannot be suitably accounted for by the main effects. Each interaction effect measures the incremental joint contribution of factors to the response variability over what can be measured by the main effects and lower-order interactions. Thus, a two-factor interaction is present in a model only if the effects of two factors on the response cannot be adequately modeled by the main effects. Similarly, a three-factor interaction is included only if the three main effects and the three two-factor interactions do not satisfactorily model the effects of the factors on the response.

2.6 The F Test

In order to find out if the differences on casting dimensions are due to assignable causes or random error the F test was implemented.

The F-test distribution function tests the hypothesis that a particular main effect or interaction is zero. The corresponding F-ratio should be around 1, since both the numerator and the denominator of the F-statistic are estimating the same quantity, the error variance. On the other hand, if the null hypothesis is false, the numerator mean square will tend to be larger that the error mean square. Thus, large F-ratios lead to rejection of the hypothesis of no factor effects. The F test applies under the assumptions that both sampled populations are normally distributed, and the samples are random and independent.

Mathematically the F ratio is expressed:

$$F = (s_1^2/\sigma_2^2)/(s_2^2/\sigma_1^2) \tag{27}$$

In this equation s^2 is the sample variance and σ^2 is the population variance. This equation is reduced to the ratio of the sample variances because it is assumed that the population variances are equal. Therefore their ratio is unity.

The hypothesis tests procedure is the following:

One tailed test	Two-tailed test	
H_o: $\sigma_2^2 = \sigma_1^2$	H_o: $\sigma_2^2 = \sigma_1^2$	(28)
H_a: $\sigma_1^2 < \sigma_2^2$	H_a: $\sigma_1^2 \neq \sigma_2^2$	(29)
Test statistic:	Test statistic:	
$F = s_1^2/s_2^2$	$F = s_1^2/s_2^2$ when $s_1^2 > s_2^2$	(30)
	$F = s_2^2/s_1^2$ when $s_2^2 > s_1^2$	(31)

Rejection region:

$$F > F_{\alpha}$$

Rejection region:

$$F > F_{\alpha/2} \quad \text{when } s_1^2 > s_2 \tag{32}$$

$$\text{or } F > F_{\alpha/2} \quad \text{when } s_1^2 > s_2 \tag{33}$$

where F_{α} and $F_{\alpha/2}$ are based on ν_1 = numerator degrees of freedom and ν_2 = denominator degrees of freedom; ν_1 and ν_2 are the degrees of freedom for the numerator and denominator sample variances, respectively.

2.7 Duncan's Multiple Range Test

Application of Duncan's multiple-range test requires that the averages be ordered from smallest to largest. Each based on sample size n. They are considered significantly different if

$$\bar{y}_i - \bar{y} > R_p, \tag{34}$$

where

$$R_p = q(\alpha_p; p, \nu)\,(MS_E/n)^{1/2} \tag{35}$$

and $q(\alpha_p; p, \nu)$ is the studentized-range critical point based on comparing the largest and the smallest of p averages, MS_E is the mean squared error based on ν degrees of freedom, and the experimentwise significance level is α_p and n is the number of observations in the treatment being compared. The experimentwise significance level is related to a comparisonwise level α through the equation

$$\alpha_p = 1 - (1 - \alpha)^{p-1}. \tag{36}$$

In this procedure, the two most extreme averages are compared first. The difference between the largest and the smallest of p = k factor-level or interaction

averages is compared using R_k in equation (35) with the experimentwise significance level of α_k. If this averages are not found significantly different with k = p, testing stops and all the averages are declared not significantly different at the $100\alpha_k\%$ significance level. This is equivalent to nonrejection of H_o: $\mu_1 = \mu_2 = ... = \mu_k$. If the two extreme averages are significantly different, testing continues.

The next step is to compare the largest average with the second smallest and the smallest average with the second largest, each test using (35) and (36) with p = k - 1. If neither of these tests is statistically significant, testing ceases and only the two extreme averages are judged significantly different. If one or both of the tests are statistically significant, testing continues with the group(s) of averages for which the two extremes have been declared significantly different. Testing continues in this fashion until no further significant differences are obtained.

2.8 Tukey's Least Significance Difference (TSD)

Tukey's procedure controls the experiment-wise error rate for multiple comparisons when all averages are based on the same number of observations. The stated experiment-wise error rate is very close to the correct value even when the sample sizes are not equal. The critical value used in the TSD formula is the upper $100\alpha\%$ point for the difference between the largest and smallest of k averages. This difference is the range of k averages, and the critical point is obtained from the distribution of range statistic.

In Tukey's procedure, two averages, $\bar{y}_i$ and $\bar{y}_j$, based on n_i and n_j observations respectively, are significantly different if

$$\bar{y}_i - \bar{y}_j > \text{TSD} \qquad (37)$$

where

$$TSD = q(\alpha;p,\nu)\left(MS_E\,[(n_i^{-1} + n_j^{-1})]/2\right)^{1/2}, \tag{38}$$

in which $q(\alpha;p,\nu)$ is the studentized range statistic, k is the number of averages being compared, MS_E is the mean squared error from an ANOVA fit to the data based on ν degrees of freedom, and α is the experimentwise error rate.

2.9 Newman-Keuls Range Test.

The computational steps are the same as Duncan's procedure. However, the values that determine the critical ranges are different.

Application of the Newman-Keuls range test requires that the averages be ordered from smallest to largest. Each based on sample size n. They are considered significantly different if

$$\bar{y}_i - \bar{y}_j > N_p, \tag{39}$$

where

$$N_p = q(\alpha_p;p,\nu)\,(MS_E/n)^{1/2} \tag{40}$$

and $q(\alpha_p;p,\nu)$ is the studentized-range critical point based on comparing the largest and the smallest of p averages, MS_E is the mean squared error based on ν degrees of freedom, and the experiment-wise significance level is α_p and n is the number of observations in the treatment being compared. The experiment-wise significance level is related to a comparison-wise level α through the equation

$$\alpha_p = 1 - (1 - \alpha)^{p-1}. \tag{41}$$

In this procedure, the two most extreme averages are compared first. The difference between the largest and the smallest of p = k factor-level or interaction

averages is compared using N_k in equation (40) with the experiment-wise significance level of α_k. If this averages are not found significantly different with k = p, testing stops and all the averages are declared not significantly different at the $100\alpha_k$% significance level. This is equivalent to non-rejection of H_o: $\mu_1 = \mu_2 = ... = \mu_k$. If the two extreme averages are significantly different, testing continues.

The next step is to compare the largest average with the second smallest and the smallest average with the second largest, each test using (40) and (41) with p = k - 1. If neither of these tests is statistically significant, testing ceases and only the two extreme averages are judged significantly different. If one or both of the tests are statistically significant, testing continues with the group(s) of averages for which the two extremes have been declared significantly different. Testing continues in this fashion until no further significant differences are obtained.

2.10 Scheffe's Test.

The Scheffe's test is similar to the Tukey's test in that a single critical difference value is computed regardless of whether the means to be compared are immediately adjacent, or if several other means fall between those being compared. The major computational difference is that Scheffe's test makes use of the F table versus the studentized range tables for the other tests. The Scheffe's test is also more stringent than Tukey's test and thus the probability of Type I error is lower.

Two means are considered significantly different if

$$\bar{y}_i - \bar{y}_j > S_p \qquad (42)$$

where

$$S_p = [(N-1)F_{kv}]^{1/2} [2MS_E / n] \qquad (43)$$

in which N is the number of groups and F is the F value for k degrees of freedoms within the group, (N-1), and v is the degrees of freedom of the error in the analysis of variance. MS_E is the mean square error and n is the number of observations.

3.0 THEORETICAL EXPERIMENTATION AND RESULTS

3.1 Flatness Evaluation

Data taken using a coordinate measurement machine (CMM) represent a sample of the total surface that is going to be analyzed. Therefore, to test for form tolerances, a sampling plan has to be devised that allows certain confidence level that the points being sampled are representative of the entire population. Menq *et al.* proved that the sample size depends on the tolerance desired and the manufacturing process capability [Menq 1990]. He came out with the following expression to estimate the number of samples required to measure form tolerances within a predefined confidence interval, (equation 21)

$$n = \tfrac{1}{2}\,[(kz_{1-\delta} - z_{\gamma})/(1-k)]^2$$

where n is the number of samples, k is the process capability and z is the critical value from the normal distribution with probability 1 - δ that the sample points will be within the range and γ the probability they will be outside the desired tolerance.

Based on this formula, it was estimated that a process with 1.33 process capability will require only nine sample points for values of $\delta = 0.025$ and $\gamma = 0.025$. A 1.33 process capability is the minimum value usually accepted for a manufacturing process [Pyzdek, 1989].

In order to test if the variation of the feature is good enough, meaning that there is a probability that all the points are going to be within the tolerance limits, the following hypothesis test is employed (4) and (5)

$$H_o : \sigma = \sigma_m$$

and

$$H_o : \sigma = \sigma_t$$

The null hypothesis states that the feature variation equals σ_m which is the standard deviation of the process under no drift and no sudden changes. In this case the confidence interval was 95%. In the case of casting σ_m is equal to 0.03937 inches. This is found using the following expression

$$6\sigma_m = T \qquad (44)$$

where T represents the tolerance range which is 0.23622 inches for sand castings and σ_m is the standard deviation for the casting process. Therefore, the maximum form error T_A is half the tolerance range. That is $T_A = \pm 0.11811$.

The critical value to test the feature variation is found using equation 22. It is found to be L = 0.044946. The values of δ and γ are both set at 0.025, giving a 95% confidence level that all the points sampled will be within the tolerance limit.

Table 1 shows the data generated to simulate plane 1. The coordinates X and Y are the positions of the probe with respect to the origin, while the Z value represents the surface variation. Table 2 shows the data generated to simulate plane 2. The coordinates X and Y are the positions of the probe with respect to the origin, while the Z value represents the surface variation.

In order to decide if the planes were flat enough, the standard deviation of the sampled point deviations or flatness error (s) was calculated and compared to the critical value L = 0.044946. In addition, the maximum measured form error was compared to the maximum expected flatness error T_A. The result of the comparisons showed that plane 1 was not flat enough because s = 0.0507 > L = 0.044946 feature variance even though all the nine points were within the tolerance limit. The maximum sampled flatness error $\varepsilon_{flatness} = 0.1056 < T_A = 0.11811$. Figure 1 shows this lack of flatness. However plane 2 was flat enough because s = 0.0289 < L = 0.044946 and $\varepsilon_{flatness} = 0.0333 < 0.11811$. There is only one point that differs in the two planes. This shows the sensitivity of this approach.

3.1 Evaluation of Parallelism

The parallelism between the internal walls of the casting was evaluated by calculating the distances between the opposite points of the casting. The parallelism error was calculated using equation 23, and this was compared to the expected error. The standard deviation for parallelism error of the internal walls was found using

$$\sigma_{parallelwalls} = \sqrt{\sigma^2_{planeA} + \sigma^2_{planeB}} \quad . \tag{44}$$

For both planes, the value of the standard deviation $\sigma_{plane} = 0.03937$. Therefore, the standard deviation allowed was equal to 0.05568. This value was used to calculate the expected tolerance range for the parallelism error. This value was set at $6\sigma_{parallelism}$ =0.33408. In the first case planes A and B meet the specification as shown on Table 3. Table 4 shows these results for planes C and D.

Table 1. Flatness Evaluation for Plane 1.

X	Y	Z	Predicted Z' value*	Flatness Error**
0	0	-0.0276	0.000177804	-0.027777804
0	5	0.1351655	0.112943225	0.022222275
0	10	0.197931	0.225708646	-0.027777646
2.5	0	-0.021528525	-0.027084054	0.005555529
2.5	5	0.041236975	0.085681367	-0.044444392
2.5	10	0.304002	0.198446787	0.105555212
5	0	-0.01545705	-0.054345912	0.038888862
5	5	0.04730845	0.058419508	-0.011111058
5	10	0.11007395	0.171184929	-0.061110979
Minimum	-0.06110			
Maximum	0.1056			
Std deviation of Flatness Error	0.0507			
L value	0.044946			
Maximum Expected Form Error (T_A)	±0.11811			

* Predicted value from the least square fitted plane

** Difference between the predicted Z' and the measured Z

Table 2. Flatness Evaluation for Plane 2.

X	Y	Z	Predicted Z' value*	Flatness Error**
0	0	-0.0276	0.00573336	-0.03333336
0	5	0.1351655	0.101832114	0.033333386
0	10	0.197931	0.197930868	1.31944E-07
2.5	0	-0.021528525	-0.021528499	-2.63889E-08
2.5	5	0.041236975	0.074570256	-0.033333281
2.5	10	0.204002	0.17066901	0.03333299
5	0	-0.01545705	-0.048790357	0.033333307
5	5	0.04730845	0.047308397	5.27778E-08
5	10	0.11007395	0.143407151	-0.033333201
Minimum	-0.0333			
Maximum	0.0333			
Std deviation of Flatness Error	0.0289			
t value	0.044946			
Maximum Expected Flatness Error (T_A)	±0.11811			

* Predicted value from the least square fitted plane
** Difference between the predicted Z' and the measured Z

The planes were also tested for flatness but none of them was found to be flat enough. This shows that flatness and parallelism are two independent measures.

The value of the ratio when the angle is seven degrees ($\cos 7° = 0.9925$) was used as the nominal value. The computed ratios were subtracted from this value to find the angular deviation. It was considered that the angle was acceptable if it was between $\cos 6.5°$ and $\cos 7.5°$.

3.2 Calculation of Casting Dimensions

The wall thickness was calculated using equation 3. It was assumed that the points taken on the external walls of the casting were exactly on the opposite side of the points taken on the internal walls. Therefore, the Euclidean distance between these points would yield the thickness of the casting. On the case of the side-wall thickness, the average of the calculated thickness along the same horizontal line was averaged to find the thickness at that position of the casting. The same procedure was applied to find the thickness at the top the casting and other dimensions such as height and length.

3.3 Factorial Analysis of Variance

The computed values of thickness, length, parallelism error, width, flatness error, and casting tapered angle were input into an analysis of variance (ANOVA) table. In this way, it is possible to verify whether or not factors under study cause casting distortion or if the differences are due only to random or chance error.

Table 3. Parallelism Evaluation Between Planes A and B.

XA	YA	ZA	XB	YB	ZB	$(XB-XA)^2$	$(YB-YA)^2$	$(ZB-ZA)^2$	$DIST_{AB}$ (XYZ)	$DIST_{AB}$ - 10
0	0	0.0667263	0	0	9.8452952	0	0	95.620408	9.77856885	-0.2214311
0	5	0.0978258	0	5	10.005832	0	0	98.168590	9.9080063	-0.0919936
0	10	-0.1519998	0	10	9.9495459	0	0	102.041227	10.101545	0.1015457
2.5	0	0.0007589	2.5	0	10.099269	0	0	101.97992	10.0985109	0.09851090
2.5	5	-0.0696830	2.5	5	10.040451	0	0	102.21481	10.1101343	0.11013435
2.5	10	0.05807778	2.5	10	9.93647825	0	0	97.5827957	9.87840046	-0.1215995
5	0	-0.0115955	5	0	9.9828189	0	0	99.888322	9.9944145	-0.0055854
5	5	0.0799590	5	5	9.9308286	0	0	97.039632	9.8508696	-0.1491303
5	10	0.0135286	5	10	10.002647	0	0	99.782491	9.9891186	-0.0108813
Sample size (N)									9	9
Minimum									9.77856885	-0.2214311
Maximum									10.1101343	0.11013435
Parallelism Error									0.33156545	0.33156545
Expected Parallelism Error	0.33408									

Table 4 . Parallelism Evaluation Between Planes C and D.

XC	YC	ZC	XD	YD	ZD	$(XD-XC)^2$	$(YD-YC)^2$	$(ZD-ZC)^2$	$DIST_{CD}$ (XYZ)	$DIST_{CD}$ - 10
0	0	-0.3792431	0	0	8.70884538	0	0	82.593353	9.0880885	-0.9119114
0	5	-0.1548023	0	5	10.1168047	0	0	105.505911	10.2716070	0.27160705
0	10	-0.2883725	0	10	9.1587542	0	0	89.248204	9.4471267	-0.5528732
2.5	0	0.3486356	2.5	0	10.419572	0	0	101.42377	10.0709371	0.07093717
2.5	5	-0.941163	2.5	5	9.7260572	0	0	113.78960	10.667220	0.6220854
2.5	10	1.2345304	2.5	10	10.068310	0	0	78.035676	8.833780	-1.1662195
5	0	-0.9221277	5	0	9.15611718	0	0	101.571020	10.0782449	0.07824492
5	5	-0.5681899	5	5	9.09532845	0	0	93.383588	9.6635184	-0.3364815
5	10	-0.6753710	5	10	10.794023	0	0	131.54700	11.469394	1.4693941
Sample size (N)									9	9
Num missings									0	0
Minimum									8.83378041	-1.1662195
Maximum									11.4693941	1.46939411
Parallelism Error									2.63561361	2.63561361
Expected Parallelism Error	0.38408									

4.0 EXPERIMENTAL DATA AND ANALYSIS OF CMM POINT CLOUD DATA

The design of experiment and point cloud data collected on the experimental castings using CMM are given in Tables 1 to 13. Table 1 provides data for the entire casting made by GM, Mercury Marine Casting Company, and Willard Industries. Table 2 gives a sample point cloud data as measured by the coordinate measuring machine (CMM). Table 3 shows sample preprocessed data from the point cloud data generated by CMM. Table 4 gives a sample of parallelism index calculation. Table 5 shows sample values for calculated parallelism indices for GM data and those of Mercury Marine. Tables 7 and 8 show sample tapered angle calculation and the tapered angle indices, respectively. Table 9 provides the indices of casting length and thickness.

Tables 10 to 13 give the results of sample statistical factorial analysis of variance (ANOVA) for parallelism and casting tapered angle. No conclusions on the results have been drawn yet, until all the data are analyzed. The casting data from Willard Industries is yet to preprocessed and analyzed.

Table 1
Experimental Design of the Project
(castings received)

		Green Sand(M1)			Resin Bonded Sand (M2)			Lost Foam Silica (M3)			Lost Foam low expansion (M4)		
		Gating			Gating			Gating			Gating		
		G1	G2	G3	G1	G2	G3	G1	G2	G3	G4	G5	G6
Orientation (O1)	Thickness (T1)				W	X		VIII	VI	I	UT25	UB25	
	Thickness (T2)				O	P					UT50	UB50	US50
	Thickness (T3)				G	H					UT75	UB75	US75
Orientation (O2)	Thickness (T1)				R	Q		VII	IX	II	DT25	DB25	DS25
	Thickness (T2)				J	I					DT50	DB50	DS50
	Thickness (T3)				B	A					DT75	DB75	DS75
Orientation (O3)	Thickness (T1)				S	T		IV	II	V	LT25	LB25	LS25
	Thickness (T2)				K	L					LT50	LB50	LS50
	Thickness (T3)				C	D					LT75	LB75	LS75

Table 2
Sample Raw Point Cloud Data

Part Program	mlbx75							
Inspector	JS							
AFSWS								
MLBX								
Nominal	-0.4627	2.46322	-0.3597	0	2.15707	8.41401	-0.7663	0
#NAME?	0	0	0	0.5	0	0	0	0.5
#NAME?	0	0	0	0.5	0	0	0	0.5
Seq# Datatype	1X	1Y	1Z	1DS	2X	2Y	2Z	2DS
6/10/97 20:08	-0.4651	2.46556	-0.3405	0.01952	2.15495	8.41613	-0.7489	0.01764
6/10/97 20:35	-0.4659	2.46634	-0.3341	0.02595	2.14717	8.42386	-0.686	0.08151
6/10/97 20:54	-0.4665	2.46696	-0.3291	0.03104	2.15177	8.41929	-0.7232	0.04371

Table 3
Preprocessed Point Cloud Data

edge points		
-0.46513	2.465612	-0.34006
2.200353	8.546066	-1.11587
6.483783	2.484127	-0.18931
right flange		
7.254267	0.149203	-0.5555
8.138394	0.106273	-0.5555
8.146027	0.044122	-3.9739
7.263708	0.072332	-3.9739
7.276548	-0.03222	-7.8922
8.158006	-0.05342	-7.7922
outer right wall		
6.659669	2.007031	-7.0329
6.467828	3.50893	-7.0329
6.277329	5.011005	-7.0329
6.295413	5.013226	-5.2653
6.492089	3.511909	-5.2653
6.688878	2.010618	-5.2653
6.719912	2.01443	-2.7177
6.524567	3.515898	-2.7177
6.323491	5.016674	-2.7177
ridge points		
3.040553	8.742195	-2.9394
3.040199	8.712707	-5.1914
3.03994	8.69106	-7.0434
outer left wall		
-0.38724	5.024503	-7.0329
-0.55802	3.520006	-7.0329
-0.73763	2.016605	-7.0329
-0.74389	2.017375	-5.2653
-0.5657	3.520949	-5.2653
-0.39501	5.025457	-5.2653
-0.40217	5.026337	-2.7177
-0.56968	3.521438	-2.7177
-0.73999	2.016896	-2.7177
left flange		
-1.26426	0.067862	-0.5555
-2.15032	0.009148	-0.5555
-2.14813	0.026976	-3.9739
-1.26498	0.062017	-3.9739
-1.26837	0.034394	-7.7922
-2.1506	0.006876	-7.7922
back edge points		
-0.41235	0.483633	-8.49066
2.270453	8.42499	-7.5739
6.389046	0.460499	-8.3023
inner right wall		
5.917741	1.2689	-7.0344
5.902407	2.9099	-7.0344
5.886802	4.5508	-7.0344
5.893762	4.5508	-5.2896
5.914546	2.9099	-5.2896
5.930889	1.2689	-5.2896
5.943654	1.2689	-2.6448
5.934176	2.9099	-2.6448
5.914089	4.5508	-2.6448
inner wall ridge		
3	8.519236	-1.1863
3	8.476131	-5.1958
3	8.459043	-7.0706
left inner wall		
0.00172	4.5508	-7.0344
0.002348	2.9099	-7.0344
0.001354	1.2689	-7.0344
-0.00174	1.2689	-5.2896
0.00139	2.9099	-5.2896
-0.00131	4.5508	-5.2896
-0.01652	4.5508	-2.6448
-0.00649	2.9099	-2.6448
0.002983	1.2689	-2.6448

edge points		
-0.46513	2.465612	-0.34006
2.200353	8.546066	-1.11587
6.483783	2.484127	-0.18931
right flange		
7.254267	0.149203	-0.5555
8.138394	0.106273	-0.5555
8.146027	0.044122	-3.9739
7.263708	0.072332	-3.9739
7.276548	-0.03222	-7.8922
8.158006	-0.05342	-7.7922
outer right wall		
6.659669	2.007031	-7.0329
6.467828	3.50893	-7.0329
6.277329	5.011005	-7.0329
6.295413	5.013226	-5.2653
6.492089	3.511909	-5.2653
6.688878	2.010618	-5.2653
6.719912	2.01443	-2.7177
6.524567	3.515898	-2.7177
6.323491	5.016674	-2.7177
ridge points		
3.040553	8.742195	-2.9394
3.040199	8.712707	-5.1914
3.03994	8.69106	-7.0434
outer left wall		
-0.38724	5.024503	-7.0329
-0.55802	3.520006	-7.0329
-0.73763	2.016605	-7.0329
-0.74389	2.017375	-5.2653
-0.5657	3.520949	-5.2653
-0.39501	5.025457	-5.2653
-0.40217	5.026337	-2.7177
-0.56968	3.521438	-2.7177
-0.73999	2.016896	-2.7177
left flange		
-1.26426	0.067862	-0.5555
-2.15032	0.009148	-0.5555
-2.14813	0.026976	-3.9739
-1.26498	0.062017	-3.9739
-1.26837	0.034394	-7.7922
-2.1506	0.006876	-7.7922
back edge points		
-0.41235	0.483633	-8.49066
2.270453	8.42499	-7.5739
6.389046	0.460499	-8.3023
inner right wall		
5.917741	1.2689	-7.0344
5.902407	2.9099	-7.0344
5.886802	4.5508	-7.0344
5.893762	4.5508	-5.2896
5.914546	2.9099	-5.2896
5.930889	1.2689	-5.2896
5.943654	1.2689	-2.6448
5.934176	2.9099	-2.6448
5.914089	4.5508	-2.6448
inner wall ridge		
3	8.519236	-1.1863
3	8.476131	-5.1958
3	8.459043	-7.0706
left inner wall		
0.00172	4.5508	-7.0344
0.002348	2.9099	-7.0344
0.001354	1.2689	-7.0344
-0.00174	1.2689	-5.2896
0.00139	2.9099	-5.2896
-0.00131	4.5508	-5.2896
-0.01652	4.5508	-2.6448
-0.00649	2.9099	-2.6448
0.002983	1.2689	-2.6448

edge points		
-0.46586	2.466332	-0.3342
2.200071	8.546346	-1.1136
6.461872	2.462378	-0.36639
right flange		
7.255554	0.138725	-0.5555
8.137665	0.112212	-0.5555
8.13846	0.105738	-3.9739
7.258021	0.11864	-3.9739
7.262684	0.080671	-7.8922
8.142553	0.072408	-7.7922
outer right wall		
6.625074	2.002783	-7.0329
6.423624	3.503501	-7.0329
6.234811	5.005784	-7.0329
6.306179	5.014548	-5.2653
6.502677	3.513209	-5.2653
6.706587	2.012793	-5.2653
6.814501	2.026046	-2.7177
6.61503	3.527007	-2.7177
6.405235	5.026713	-2.7177
ridge points		
3.040293	8.720469	-2.9394
3.040489	8.736859	-5.1914
3.040694	8.75395	-7.0434
outer left wall		
-0.39594	5.025572	-7.0329
-0.5685	3.521293	-7.0329
-0.74069	2.016981	-7.0329
-0.74402	2.017391	-5.2653
-0.56853	3.521296	-5.2653
-0.39245	5.025144	-5.2653
-0.38662	5.024427	-2.7177
-0.5634	3.520667	-2.7177
-0.7367	2.016491	-2.7177
left flange		
-1.26603	0.053454	-0.5555
-2.15074	0.005736	-0.5555
-2.14902	0.019721	-3.9739
-1.26601	0.053575	-3.9739
-1.26756	0.040964	-7.7922
-2.15028	0.009534	-7.7922
back edge points		
-0.41256	0.483837	-8.49231
2.276677	8.418812	-7.5236
6.416174	0.487427	-8.52155
inner right wall		
5.874819	1.2689	-7.0344
5.848669	2.9099	-7.0344
5.829417	4.5508	-7.0344
5.894061	4.5508	-5.2896
5.918674	2.9099	-5.2896
5.946097	1.2689	-5.2896
6.044599	1.2689	-2.6448
6.026441	2.9099	-2.6448
5.998692	4.5508	-2.6448
inner wall ridge		
3	8.478096	-1.1863
3	8.504062	-5.1958
3	8.525895	-7.0706
left inner wall		
-0.00524	4.5508	-7.0344
-0.00366	2.9099	-7.0344
0.001366	1.2689	-7.0344
-0.00065	1.2689	-5.2896
-0.001	2.9099	-5.2896
0.000933	4.5508	-5.2896
-0.00426	4.5508	-2.6448
-0.00356	2.9099	-2.6448
0.002984	1.2689	-2.6448

Table 4
Sample Parallelism Calculation

x	y	z	x	y	z	xdiff sq	ydiff sq	zdiff sq	distance
5.917741	1.2689	-7.0344	0.001354	1.2689	-7.0344	35.0036351	0	0	**5.916387**
5.930889	1.2689	-5.2896	-0.00174	1.2689	-5.2896	35.1960869	0	0	**5.932629**
5.943654	1.2689	-2.6448	0.002983	1.2689	-2.6448	35.2915719	0	0	**5.940671**
5.902407	2.9099	-7.0344	0.002348	2.9099	-7.0344	34.8106962	0	0	**5.900059**
5.914546	2.9099	-5.2896	0.00139	2.9099	-5.2896	34.9654139	0	0	**5.913156**
5.934176	2.9099	-2.6448	-0.006486	2.9099	-2.6448	35.291465	0	0	**5.940662**
5.886802	4.5508	-7.0344	0.00172	4.5508	-7.0344	34.6341901	0	0	**5.885082**
5.893762	4.5508	-5.2896	-0.001305	4.5508	-5.2896	34.7518149	0	0	**5.895067**
5.914089	4.5508	-2.6448	-0.01652	4.5508	-2.6448	35.1721231	0	0	**5.930609**
x	y	z	x	y	z	xdiff sq	ydiff sq	zdiff sq	distance
5.984187	1.2689	-7.0344	-0.000575	1.2689	-7.0344	35.8173762	0	0	**5.984762**
6.000494	1.2689	-5.2896	-0.003289	1.2689	-5.2896	36.0454103	0	0	**6.003783**
6.018234	1.2689	-2.6448	0.000346	1.2689	-2.6448	36.214976	0	0	**6.017888**
5.970617	2.9099	-7.0344	-0.001003	2.9099	-7.0344	35.6602454	0	0	**5.97162**
5.983752	2.9099	-5.2896	-0.001014	2.9099	-5.2896	35.8174241	0	0	**5.984766**
6.005671	2.9099	-2.6448	-0.006583	2.9099	-2.6448	36.1471982	0	0	**6.012254**
5.950331	4.5508	-7.0344	0.001281	4.5508	-7.0344	35.3911959	0	0	**5.94905**
5.960258	4.5508	-5.2896	0.001726	4.5508	-5.2896	35.5041036	0	0	**5.958532**
5.981824	4.5508	-2.6448	-0.009927	4.5508	-2.6448	35.90108	0	0	**5.991751**
x	y	z	x	y	z	xdiff sq	ydiff sq	zdiff sq	distance
5.874819	1.2689	-7.0344	0.001366	1.2689	-7.0344	34.4974501	0	0	**5.873453**
5.946097	1.2689	-5.2896	-0.000645	1.2689	-5.2896	35.3637404	0	0	**5.946742**
6.044599	1.2689	-2.6448	0.002984	1.2689	-2.6448	36.5011118	0	0	**6.041615**
5.848669	2.9099	-7.0344	-0.003663	2.9099	-7.0344	34.2497898	0	0	**5.852332**
5.918674	2.9099	-5.2896	-0.001	2.9099	-5.2896	35.0425403	0	0	**5.919674**
6.026441	2.9099	-2.6448	-0.003563	2.9099	-2.6448	36.3609482	0	0	**6.030004**
5.829417	4.5508	-7.0344	-0.005243	4.5508	-7.0344	34.0432573	0	0	**5.83466**
5.894061	4.5508	-5.2896	0.000933	4.5508	-5.2896	34.7289576	0	0	**5.893128**
5.998692	4.5508	-2.6448	-0.00426	4.5508	-2.6448	36.0354327	0	0	**6.002952**

replicate	max dist	min dist	parallelism
1	5.940671	5.885082	**0.055589**
2	6.017888	5.94905	**0.068838**
3	6.041615	5.83466	**0.206955**

Table 5
Calculated Parallelism Indices

Parallelism		
Replicate 1	Replicate 2	Replicate 3
	GM castings	
0.103218	0.088817	0.086813
0.088361	0.070649	0.064923
0.055758	0.066823	0.058323
0.058025	0.065111	0.089883
0.047846	0.038634	0.033706
0.088041	0.072947	0.094816
0.062106	0.114386	0.104709
0.098669	0.115578	0.076238
0.069784	0.121687	0.066812
0.125735	0.11001	0.121124
0.053597	0.070561	0.058717
0.042429	0.062069	0.098399
0.240118	0.311214	0.422158
0.035822	0.042532	0.038115
0.124225	0.065333	0.465808
0.077295	0.09655	0.052821
0.104812	0.08911	0.050288
0.044177	0.071758	0.335876
	Mercury Marine Castings	
0.057523	0.076893	0.052071
0.064642	0.04391	0.090435
0.047223	0.06407	0.030405
0.055375	0.039051	0.090944
0.036412	0.053795	0.067654
0.03839	0.072665	0.016217
0.05927	0.050278	0.141063
0.027215	0.022399	0.096454
0.140749	0.07201	0.061333
0.019257	0.024674	0.032919
0.077216	0.053802	0.069645
0.117974	0.063625	0.063145
0.058892	0.091607	0.148055
0.055589	0.068838	0.206955
0.066196	0.136093	0.104868
0.066662	0.050121	0.034129
0.123302	0.093492	0.087263
0.12346	0.132314	0.140834

Table 7
Sample Tapered Angle Calculation

Casting Angle
Replicate 1

outer right wall			inner right wall						Casting angle
6.659669	2.007031	-7.0329	5.917741	1.2689	-7.0344	5.917741	1.2689	-7.0344	**10.10517**
6.467828	3.50893	-7.0329	5.902407	2.9099	-7.0344	5.889638	4.25	-7.0344	
6.277329	5.011005	-7.0329	5.886802	4.5508	-7.0344				
6.295413	5.013226	-5.2653	5.893762	4.5508	-5.2896	5.930889	1.2689	-5.2896	**10.10635**
6.492089	3.511909	-5.2653	5.914546	2.9099	-5.2896	5.897165	4.25	-5.2896	
6.688878	2.010618	-5.2653	5.930889	1.2689	-5.2896				
6.719912	2.01443	-2.7177	5.943654	1.2689	-2.6448	5.943654	1.2689	-2.6448	**10.11648**
6.524567	3.515898	-2.7177	5.934176	2.9099	-2.6448	5.916799	4.25	-2.6448	
6.323491	5.016674	-2.7177	5.914089	4.5508	-2.6448				

outer left wall			inner left wall						
-0.38724	5.024503	-7.0329	0.00172	4.5508	-7.0344	0.001354	1.2689	-7.0344	**10.12264**
-0.55802	3.520006	-7.0329	0.002348	2.9099	-7.0344	0.001686	4.25	-7.0344	
-0.73763	2.016605	-7.0329	0.001354	1.2689	-7.0344				
-0.74389	2.017375	-5.2653	-0.00174	1.2689	-5.2896	-0.00174	1.2689	-5.2896	**10.12358**
-0.5657	3.520949	-5.2653	0.00139	2.9099	-5.2896	-0.00134	4.25	-5.2896	
-0.39501	5.025457	-5.2653	-0.00131	4.5508	-5.2896				
-0.40217	5.026337	-2.7177	-0.01652	4.5508	-2.6448	0.002983	1.2689	-2.6448	**10.12809**
-0.56968	3.521438	-2.7177	-0.00649	2.9099	-2.6448	-0.01473	4.25	-2.6448	
-0.73999	2.016896	-2.7177	0.002983	1.2689	-2.6448				

Replicate 2

outer right wall			inner right wall						
6.73596	2.0164	-7.0329	5.984187	1.2689	-7.0344	5.984187	1.2689	-7.0344	**10.10576**
6.543164	3.518182	-7.0329	5.970617	2.9099	-7.0344	5.953434	4.25	-7.0344	
6.34777	5.019656	-7.0329	5.950331	4.5508	-7.0344				
6.366982	5.022015	-5.2653	5.960258	4.5508	-5.2896	6.000494	1.2689	-5.2896	**10.10747**
6.568532	3.521297	-5.2653	5.983752	2.9099	-5.2896	5.963946	4.25	-5.2896	
6.765449	2.020022	-5.2653	6.000494	1.2689	-5.2896				
6.79764	2.023975	-2.7177	6.018234	1.2689	-2.6448	6.018234	1.2689	-2.6448	**10.11727**
6.600958	3.525279	-2.7177	6.005671	2.9099	-2.6448	5.985161	4.25	-2.6448	
6.394398	5.025382	-2.7177	5.981824	4.5508	-2.6448				

outer left wall			inner left wall						
-0.38659	5.024423	-7.0329	0.001281	4.5508	-7.0344	-0.00058	1.2689	-7.0344	**10.12087**
-0.56147	3.52043	-7.0329	-0.001	2.9099	-7.0344	0.001111	4.25	-7.0344	
-0.7396	2.016847	-7.0329	-0.00058	1.2689	-7.0344				
-0.74571	2.017598	-5.2653	-0.00329	1.2689	-5.2896	-0.00329	1.2689	-5.2896	**10.119**
-0.56664	3.521065	-5.2653	-0.00101	2.9099	-5.2896	0.001266	4.25	-5.2896	
-0.3897	5.024805	-5.2653	0.001726	4.5508	-5.2896				
-0.39196	5.025083	-2.7177	-0.00993	4.5508	-2.6448	0.000346	1.2689	-2.6448	**10.123**
-0.56652	3.52105	-2.7177	-0.00658	2.9099	-2.6448	-0.00899	4.25	-2.6448	
-0.7396	2.016847	-2.7177	0.000346	1.2689	-2.6448				

Table 8
Tapered Angle Indices

Tapered Angle					
Left Walls			Right Walls		
replicate 1	replicate 2	replicate 3	replicate 1	replicate 2	replicate 3
GM Castings					
10.096	10.0978	10.1254	10.109	10.1148	10.0973
10.1014	10.0939	10.1016	10.1209	10.1308	10.1209
10.1103	10.1146	10.1143	10.1313	10.1311	10.1114
10.1078	10.112	10.1116	10.1239	10.1104	10.108
10.126	10.1275	10.131	10.1443	10.1419	10.1498
10.1028	10.1102	10.106	10.1224	10.1178	10.1292
10.1097	10.1062	10.1104	10.1211	10.0962	10.1104
10.1008	10.101	10.1015	10.1263	10.1041	10.1262
10.1047	10.1134	10.1111	10.1123	10.0758	10.1114
10.1083	10.1083	10.1103	10.077	10.0958	10.1043
10.1141	10.097	10.129	10.1087	10.1366	10.0978
10.1133	10.1079	10.1078	10.1215	10.1073	10.1043
10.1108	10.1063	10.1183	9.82847	9.87729	10.021
10.1458	10.1168	10.1178	10.1217	10.116	10.1144
10.127	10.1231	10.1355	10.0819	10.102	9.89926
10.1244	10.1217	10.1197	10.0773	10.071	10.1349
10.139	10.112	10.123	10.0866	10.1104	10.1119
10.1163	10.1104	10.0995	10.1284	10.1239	9.63611
Mercury Marine Castings					
10.1161	10.1162	10.1166	10.1116	10.1059	10.1179
10.1143	10.1151	10.1127	10.105	10.1219	10.1071
10.1171	10.1148	10.1163	10.1087	10.1136	10.1156
10.1158	10.117	10.1168	10.1315	10.114	10.0991
10.1137	10.1103	10.1103	10.1159	10.1171	10.1096
10.1171	10.1159	10.1162	10.1134	10.1246	10.1166
10.1173	10.116	10.1162	10.1163	10.1273	10.0678
10.1177	10.1156	10.1177	10.116	10.1218	10.1169
10.1162	10.1168	10.1164	10.0689	10.1185	10.1366
10.1191	10.1174	10.1162	10.1142	10.1143	10.1155
10.1156	10.1148	10.1156	10.1108	10.1499	10.1163
10.116	10.1154	10.117	10.1512	10.1179	10.106
10.1183	10.1267	10.1395	10.1006	10.0614	10.1578
10.1248	10.121	10.1233	10.1093	10.1102	10.1001
10.145	10.1175	10.1276	10.1134	10.1657	10.1346
10.1186	10.1189	10.12	10.1052	10.114	10.18
10.1295	10.1241	10.1173	10.1309	10.1441	10.1678
10.134	10.137	10.1274	10.0897	10.0798	10.1409

Table 9
Length Height and Thickness Indices

Length Of Castings			Height of Castings			Thickness of Castings		
replicate 1	replicate 2	replicate 3	replicate 1	replicate 2	replicate 3	replicate 1	replicate 2	replicate 3
				GM Castings				
7.74428	7.78166	7.81487	8.89013	8.88787	8.88858	0.788787	0.823342	0.791793
7.74045	7.82117	7.73034	8.93448	8.9308	8.90909	0.842067	0.842453	0.821847
7.75902	7.77516	7.83668	8.88784	8.88054	8.87908	0.799894	0.902336	0.815124
7.79932	7.74668	7.78374	8.86854	8.90138	8.9152	0.813682	0.813068	0.812071
7.76134	7.74285	7.77129	8.88254	8.87914	8.89237	0.794271	0.793885	0.804197
7.78135	7.74826	7.78722	8.87986	8.86713	8.88103	0.807568	0.799756	0.809167
7.84652	7.79045	7.77857	8.86413	8.85883	8.87911	0.543689	0.549846	0.54482
7.78009	7.82135	7.78789	8.88458	8.90428	8.90067	0.550003	0.546673	0.528449
7.79883	7.83353	7.81967	8.87143	8.84753	8.87356	0.515331	0.53454	0.526249
7.80787	7.81948	7.82259	8.86489	8.85834	8.85159	0.544487	0.53861	0.524877
7.73455	7.79363	7.74115	8.87679	8.84603	8.87313	0.507401	0.509267	0.54191
7.79589	7.80871	7.82006	8.87683	8.87345	8.87654	0.533668	0.529316	0.55986
7.77436	7.76044	7.73036	8.86249	8.84664	8.83254	0.295548	0.393033	0.306139
7.79213	7.74685	7.75721	8.90779	8.91187	8.91201	0.29188	0.310805	0.299936
7.77386	7.82105	7.72069	8.90608	8.92214	8.89351	0.31566	0.31137	0.286473
7.79284	7.80655	7.78458	8.90012	8.89001	8.92253	0.318492	0.296932	0.310054
7.74744	7.75073	7.7709	8.86877	8.85554	8.85747	0.29856	0.26478	0.270593
7.7667	7.78162	7.75732	8.9069	8.92281	8.83153	0.294941	0.629715	0.264975
				Mercury Marine Castings				
6.47751	6.479	6.4698	8.69983	8.70662	8.67157	0.825732	0.833644	0.782362
6.45505	6.48754	6.48192	8.57764	8.63234	8.61574	0.746713	0.754534	0.753857
6.48152	6.48448	6.46096	8.62326	8.62136	8.60829	0.754529	0.755723	0.749055
6.46381	6.46754	6.48163	8.61108	8.61253	8.59045	0.751347	0.75304	0.749131
6.48429	6.46174	6.46035	8.61632	8.6144	8.60648	0.751952	0.750862	0.747761
6.46408	6.46303	6.46726	8.65981	8.64378	8.65812	0.779826	0.777401	0.77159
6.49647	6.48472	6.49377	8.67335	8.76563	8.68764	0.519775	0.619979	0.583527
6.4802	6.47868	6.49882	8.64463	8.63189	8.63616	0.535164	0.520522	0.507219
6.47864	6.47183	6.4773	8.5857	8.59619	8.6527	0.511792	0.502861	0.514936
6.48532	6.4749	6.47753	8.63906	8.62537	8.63683	0.506563	0.510305	0.519201
6.4517	6.44926	6.44254	8.58265	8.61672	8.57555	0.503234	0.509625	0.510766
6.46997	6.47161	6.46394	8.61792	8.77844	8.61671	0.547126	0.639958	0.501949
6.42452	6.42102	6.42656	8.6958	8.65844	8.71002	0.318272	0.257897	0.248105
6.45803	6.45803	6.41	8.65639	8.65639	8.65609	0.230517	0.230517	0.234408
6.45217	6.41587	6.4332	8.69753	8.67697	8.67167	0.239492	0.239351	0.242738
6.44183	6.4364	6.438	8.66935	8.66715	8.66813	0.227066	0.238594	0.232
6.39634	6.39185	6.41721	8.59836	8.63806	8.60944	0.23735	0.245826	0.229104
6.41934	6.41938	6.41842	8.61016	8.64259	8.84082	0.255123	0.308953	0.39296

Table 10
Factorial Analysis of Variance
(parallelism index of GM castings)

Number of Factors = 3

Number of Replicates = 3

Factor	Levels
G = Gating System	2
O = Orientation	3
T = Thickness	3

Source	SS	DF	MS	F	P	F 0.01	significant?	F 0.05	significant?
GOT	0.05493522	4	0.01373381	2.86890464	0.03676204	3.890306743	FALSE	2.63353428	TRUE
GO	0.04454312	2	0.02227156	4.65238768	0.0159534	5.247898116	FALSE	3.25944427	TRUE
GT	0.05320418	2	0.02660209	5.55700704	0.00788394	5.247898116	TRUE	3.25944427	TRUE
G	0.01298621	1	0.01298621	2.71273736	0.10825303	7.395556167	FALSE	4.113161367	FALSE
OT	0.00535544	4	0.00133886	0.27967925	0.88919495	3.890306743	FALSE	2.63353428	FALSE
O	0.01410773	2	0.00705386	1.47350731	0.24261066	5.247898116	FALSE	3.25944427	FALSE
T	0.05994014	2	0.02997007	6.26055692	0.00464185	5.247898116	TRUE	3.25944427	TRUE
Error	0.1723365	36	0.00478713						
Total	0.41740854	53							

Table 11
Factorial Analysis of Variance
(parallelism index for Mercury Marine castings)

Number of Factors = 3

Number of Replicates = 3

Factor	Levels
G = Gating System	2
O = Orientation	3
T = Thickness	3

Source	SS	DF	MS	F	P	F 0.01	significant?	F 0.05	significant?
GOT	0.01036425	4	0.00259106	0.52762087	0.71611095	3.890306743	FALSE	2.63353428	FALSE
GO	0.00126259	2	0.00063129	0.12855113	0.87977044	5.247898116	FALSE	3.25944427	FALSE
GT	0.01283305	2	0.00641652	1.30660421	0.28326897	5.247898116	FALSE	3.25944427	FALSE
G	0.00064683	1	0.00064683	0.13171399	0.71878378	7.395556167	FALSE	4.113161367	FALSE
OT	0.00753923	4	0.00188481	0.38380544	0.81874141	3.890306743	FALSE	2.63353428	FALSE
O	0.00101008	2	0.00050504	0.10284192	0.9025337	5.247898116	FALSE	3.25944427	FALSE
T	0.0494638	2	0.0247319	5.03618553	0.01179003	5.247898116	FALSE	3.25944427	TRUE
Error	0.17679023	36	0.00491084						
Total	0.25991005	53							

Table 12
Factorial Analysis of Variance
(parallelsim index of GM and Mercury Marine Castings)

Number of Factors = 4

Number of Replicates = 3

Factor	Levels
G = Gating System	2
O = Orientation	3
T = Thickness	3
M = Sand Casting	2

Source	SS	DF	MS	F	P	F 0.01	significant?	F 0.05	significant?
GOTM	0.03786541	4	0.00946635	1.95223489	0.11104187	3.59148089	FALSE	2.498921958	FALSE
GOT	0.02743406	4	0.00685851	1.4144234	0.237885	3.59148089	FALSE	2.498921958	FALSE
GOM	0.01721401	2	0.00860701	1.77501286	0.17681686	4.912692475	FALSE	3.123901138	FALSE
GO	0.0285917	2	0.01429585	2.94821641	0.05879459	4.912692475	FALSE	3.123901138	FALSE
GTM	0.05688805	2	0.02844403	5.86597844	0.004364	4.912692475	TRUE	3.123901138	TRUE
GT	0.00914917	2	0.00457459	0.94341139	0.3940562	4.912692475	FALSE	3.123901138	FALSE
GM	0.00971476	1	0.00971476	2.0034646	0.16125116	7.000494406	FALSE	3.973894991	FALSE
G	0.00391827	1	0.00391827	0.80806123	0.37169056	7.000494406	FALSE	3.973894991	FALSE
OTM	0.00989205	4	0.00247301	0.51000632	0.72852271	3.59148089	FALSE	2.498921958	FALSE
OT	0.00300262	4	0.00075065	0.15480668	0.9602366	3.59148089	FALSE	2.498921958	FALSE
OM	0.00744727	2	0.00372363	0.76792079	0.46773887	4.912692475	FALSE	3.123901138	FALSE
O	0.00767054	2	0.00383527	0.79094318	0.45731648	4.912692475	FALSE	3.123901138	FALSE
TM	0.00034513	2	0.00017257	0.0355883	0.96505448	4.912692475	FALSE	3.123901138	FALSE
T	0.1090588	2	0.0545294	11.24553512	5.62E-05	4.912692475	TRUE	3.123901138	TRUE
M	0.01088143	1	0.01088143	2.24406523	0.13849953	7.000494406	FALSE	3.973894991	FALSE
Error	0.34912674	72	0.00484898						
Total	0.68820003	107							

Table 13
Factorial Analysis of Variance
(left casting angle index of GM castings)

Number of Factors = 3

Number of Replicates = 3

Factor	Levels
G = Gating System	2
O = Orientation	3
T = Thickness	3

Source	SS	DF	MS	F	P	F 0.01	significant?	F 0.05	significant?
GOT	0.00062537	4	0.00015634	2.29249722	0.07834108	3.890306743	FALSE	2.63353428	FALSE
GO	0.00046634	2	0.00023317	3.41908114	0.04370087	5.247898116	FALSE	3.25944427	TRUE
GT	0.00016631	2	8.32E-05	1.21935665	0.30733064	5.247898116	FALSE	3.25944427	FALSE
G	0.00044239	1	0.00044239	6.48695117	0.01528517	7.395556167	FALSE	4.113161367	TRUE
OT	0.00053181	4	0.00013295	1.94952476	0.12331034	3.890306743	FALSE	2.63353428	FALSE
O	0.00048216	2	0.00024108	3.53505534	0.03965311	5.247898116	FALSE	3.25944427	TRUE
T	0.00144519	2	0.00072259	10.59564652	0.00024072	5.247898116	TRUE	3.25944427	TRUE
Error	0.0024551	36	6.82E-05						
Total	0.00661468	53							

APPENDIX

This appendix contains all the available heat flux results from the second sequence of pours. These results were obtained using the analysis program "heat4" which does not consider the measured plate temperature directly in the computation. In most cases, only one of the two measured mold temperatures was used to compute the results.

1.0" Plates Poured at 45 Degrees (Bots) 07/01/98 + 07/02/98

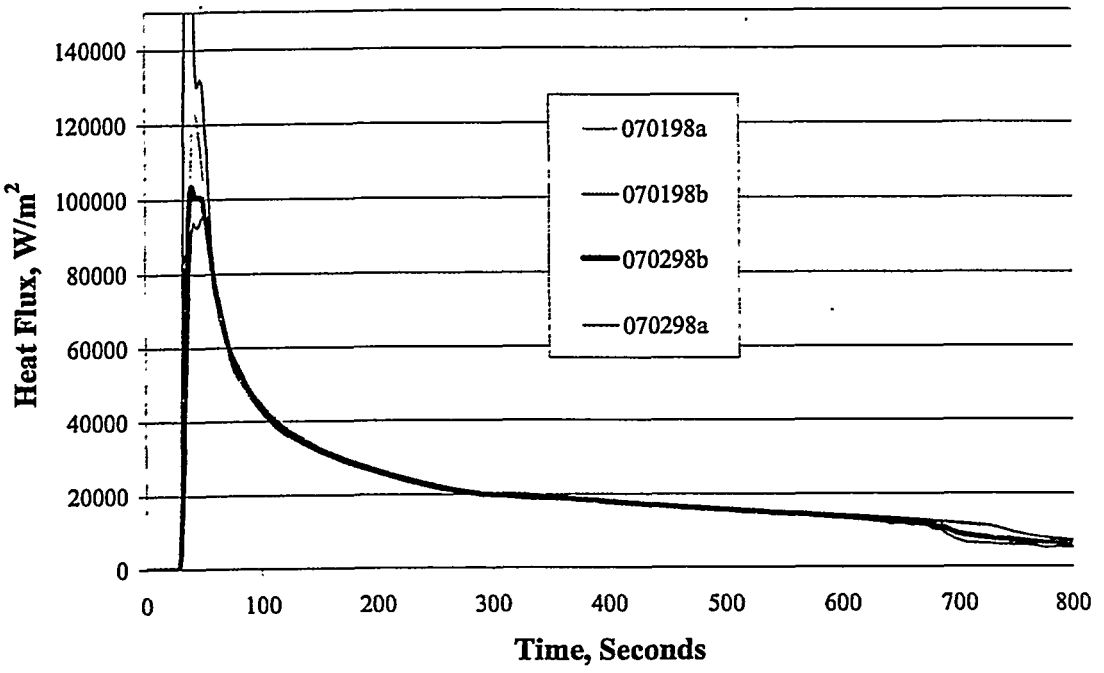

1.0" Plates Poured at 45 Degrees (Tops) 07/01/98 + 07/02/98

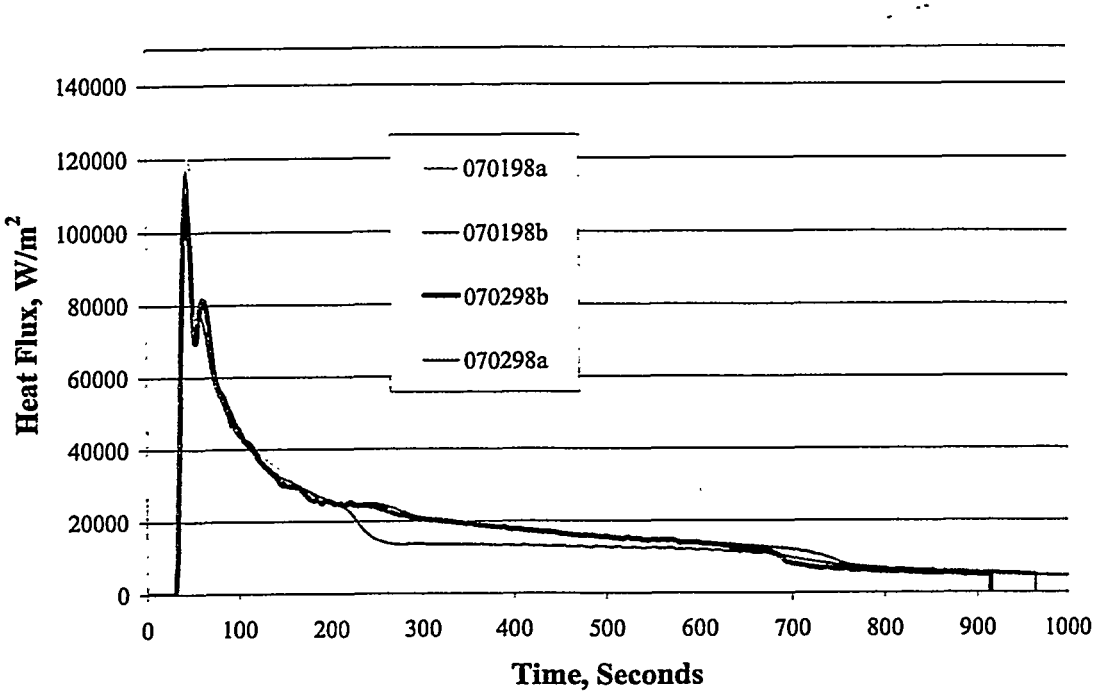

0.25" Vertical Plates (Bots) 07/15/98 + 07/17/98

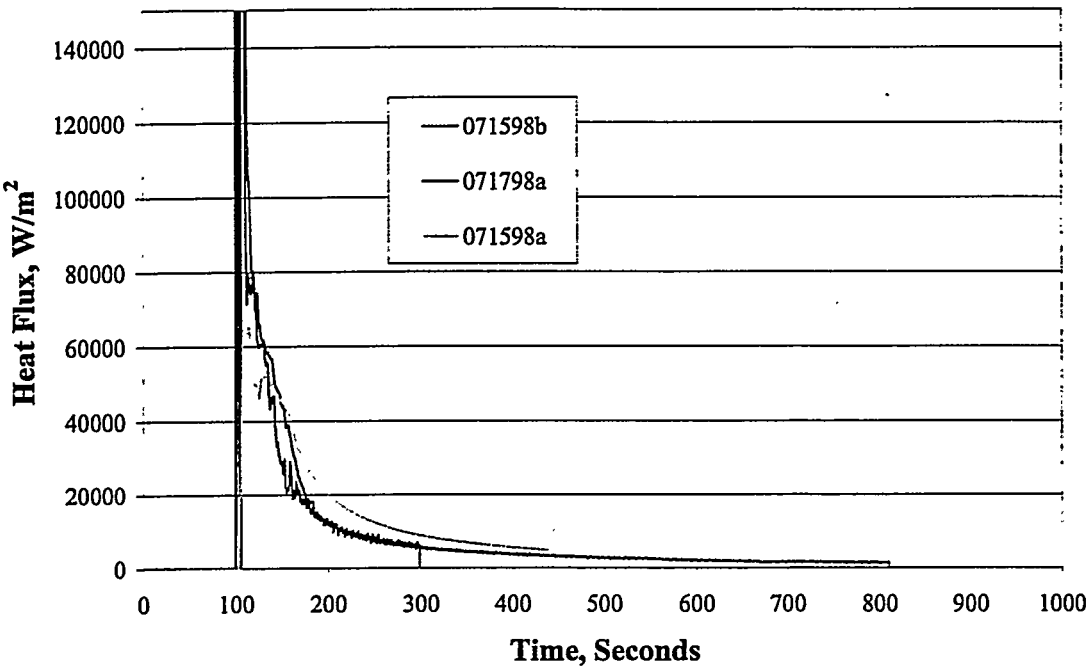

0.25" Vertical Plates (Tops) 07/15/98 + 07/17/98

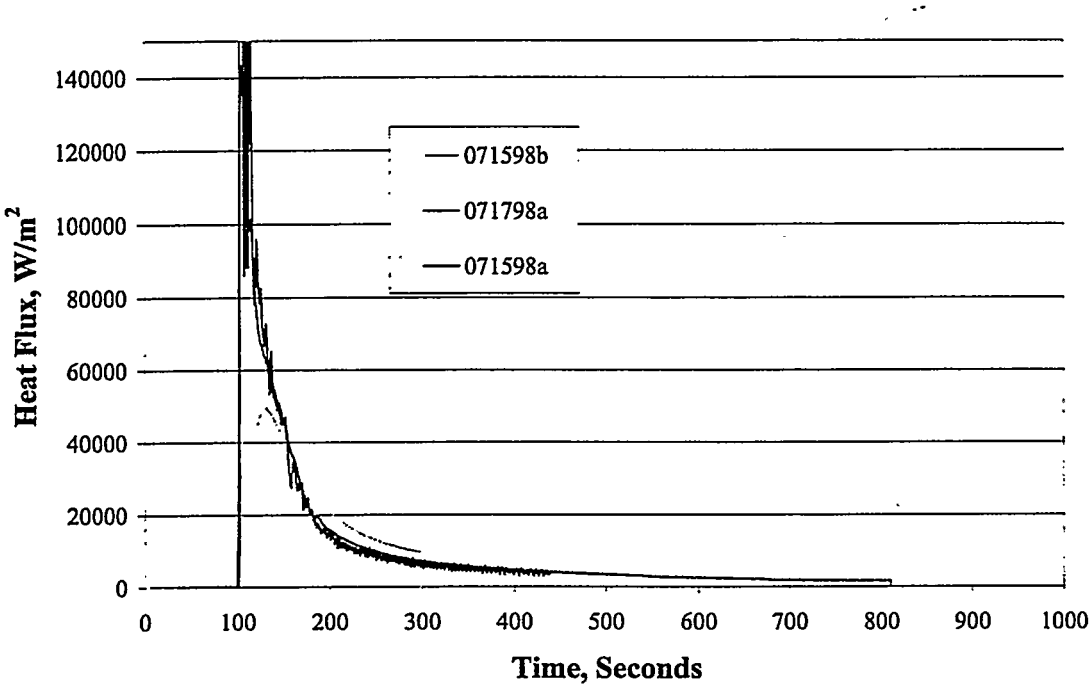

0.5" Vertical Plates (Bots) 07/15/98 + 07/17/98

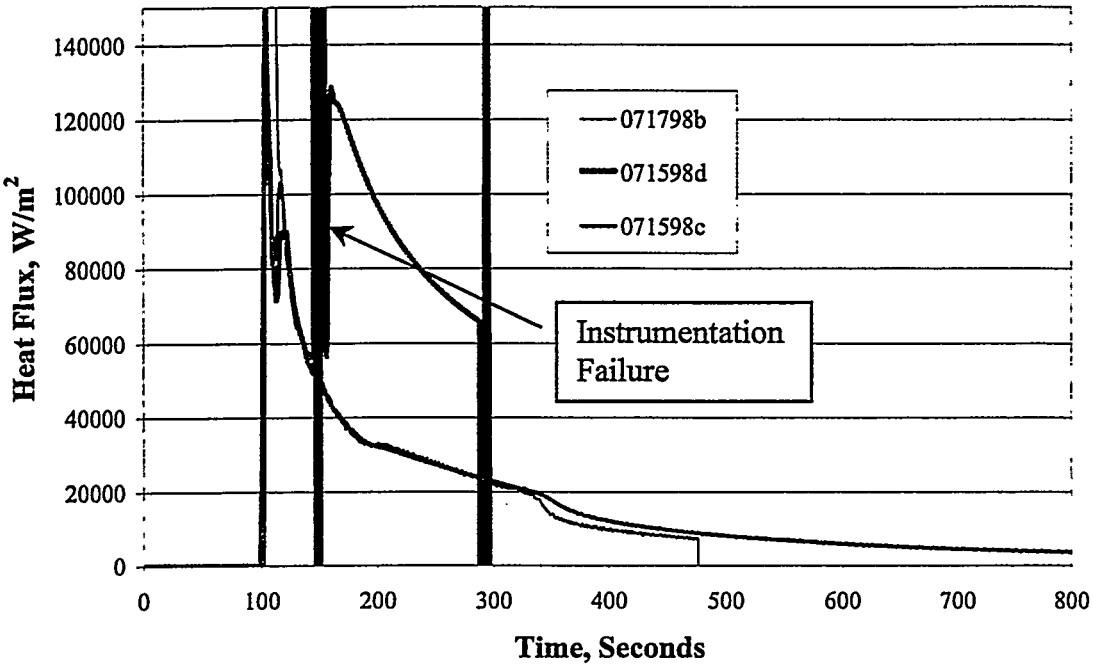

0.5" Vertical Plates (Tops) 07/15/98 + 07/17/98

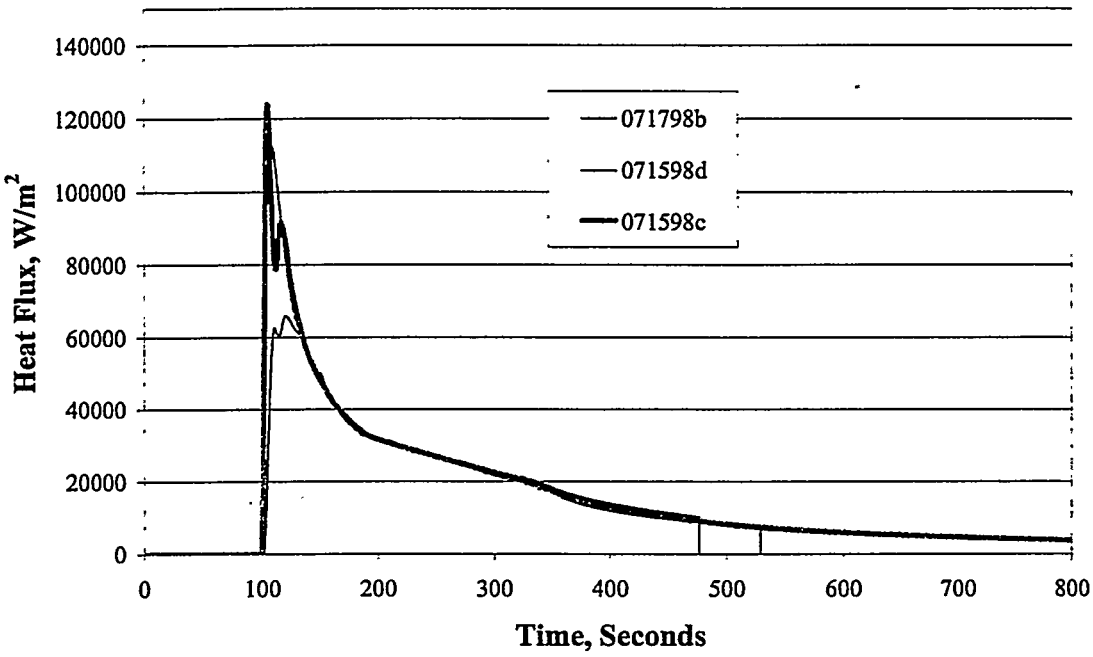

1.0" Vertical Plates (Bots) 07/23/98 + 07/24/98

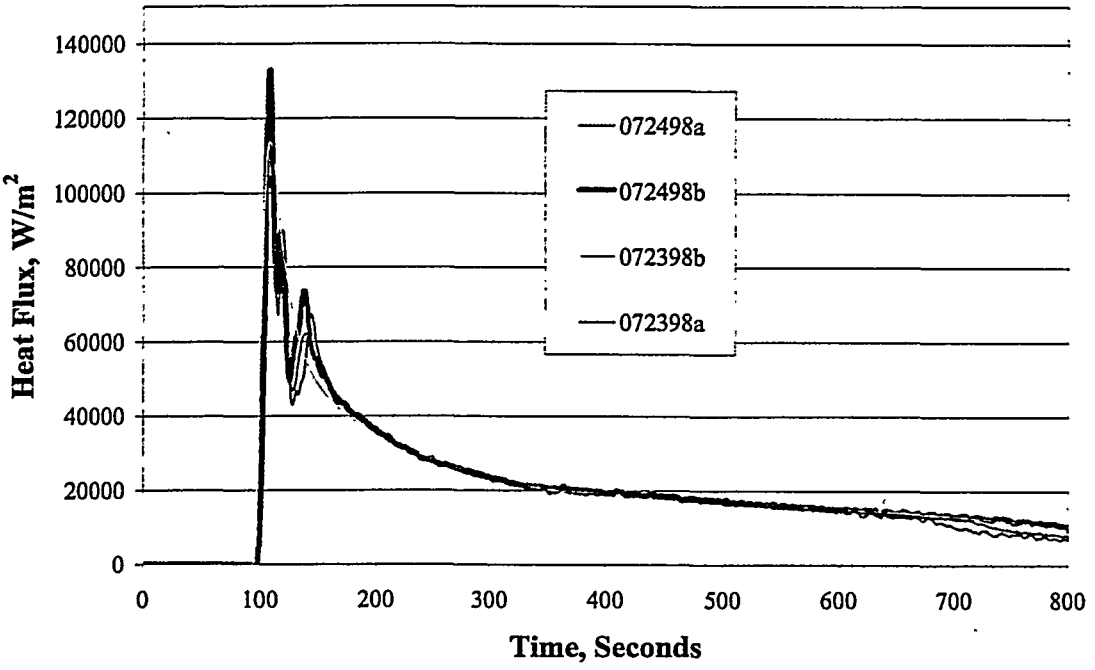

1.0" Vertical Plates (Tops) 07/23/98 + 07/24/98

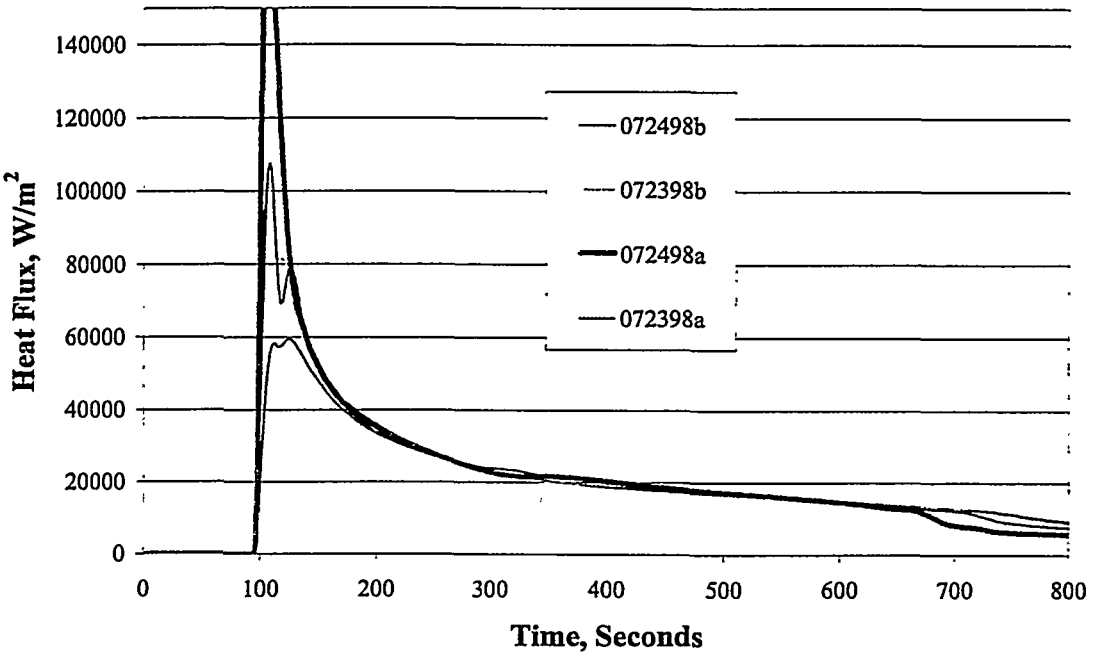

0.25" Horizontal Plates (Bots) 07/29/98 + 07/30/98 + 08/24/98

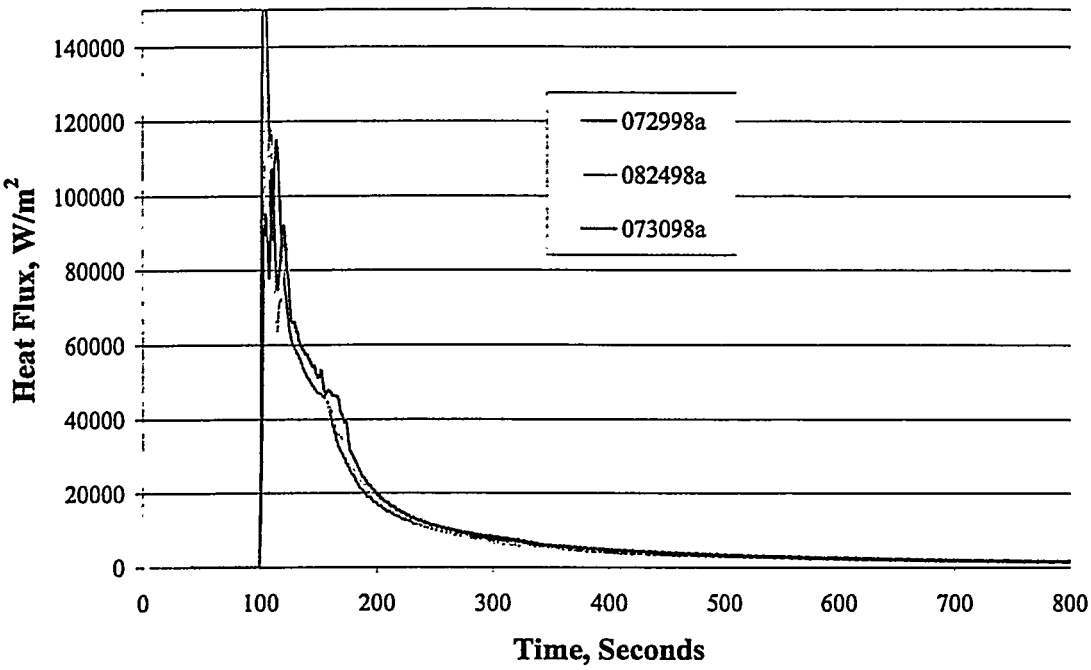

0.25" Horizontal Plates (Tops) 07/29/98 + 07/30/98 + 08/24/98

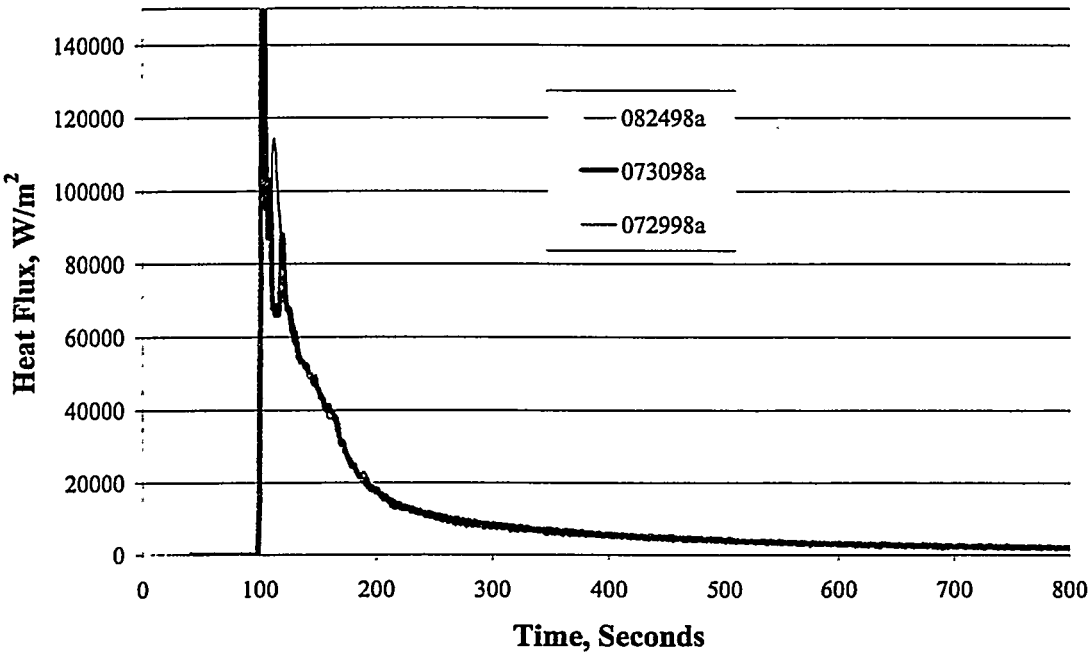

0.50" Horizontal Plates (Bots) 07/29/98 + 07/30/98 + 08/24/98

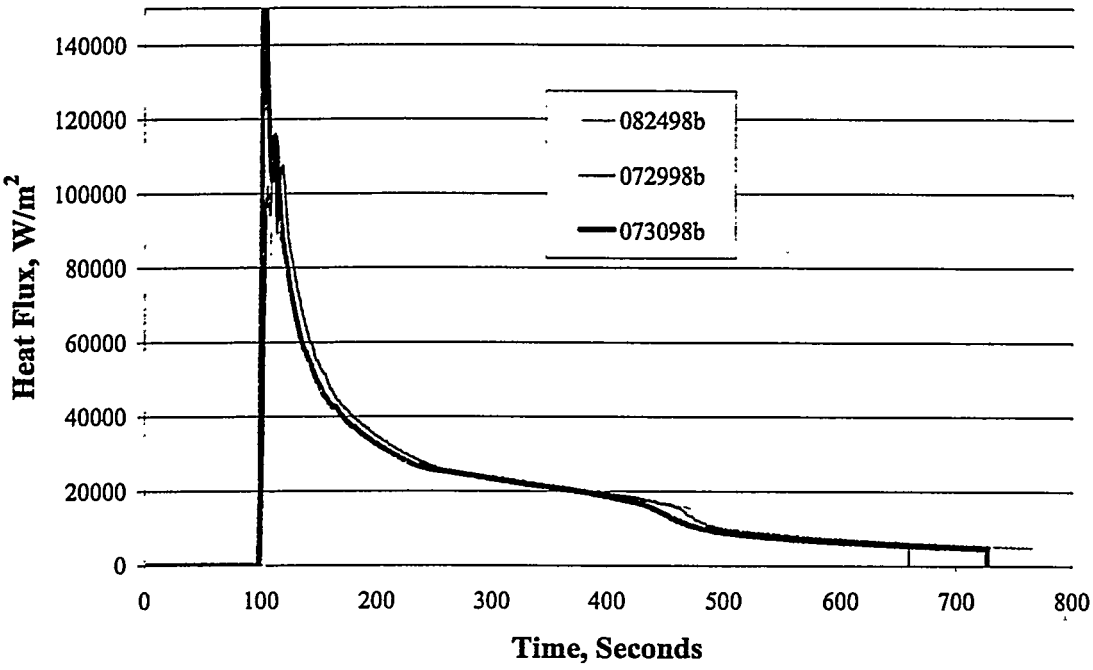

0.50" Horizontal Plates (Tops) 07/29/98 + 07/30/98 + 08/24/98

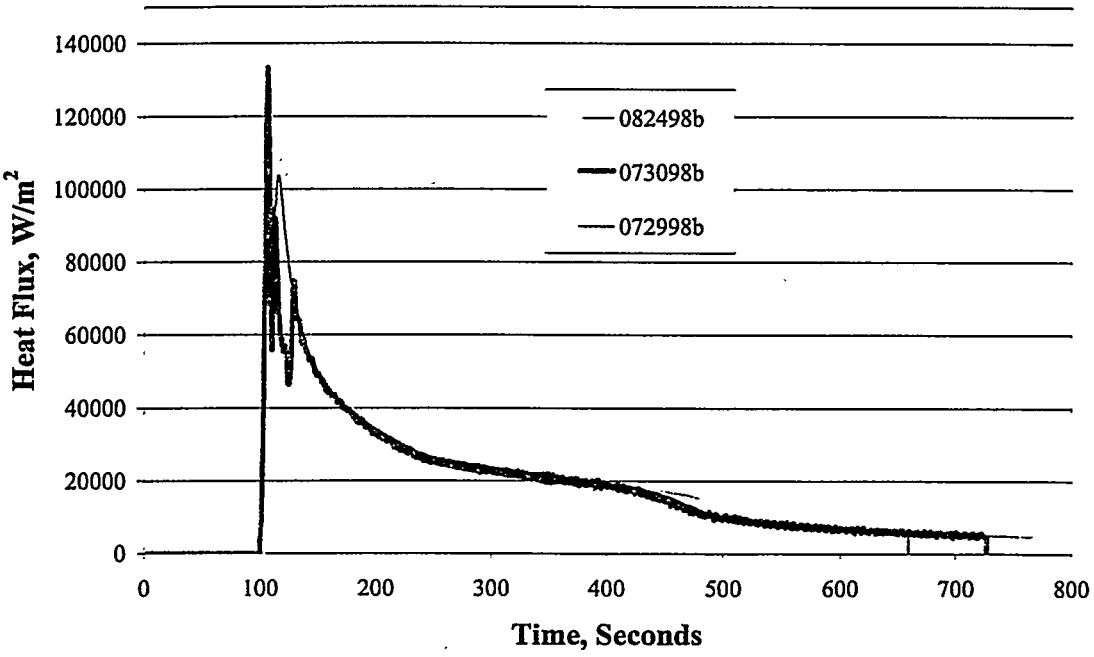

1.0" Horizontal Plates (Bots) 08/13/98 + 08/25/98

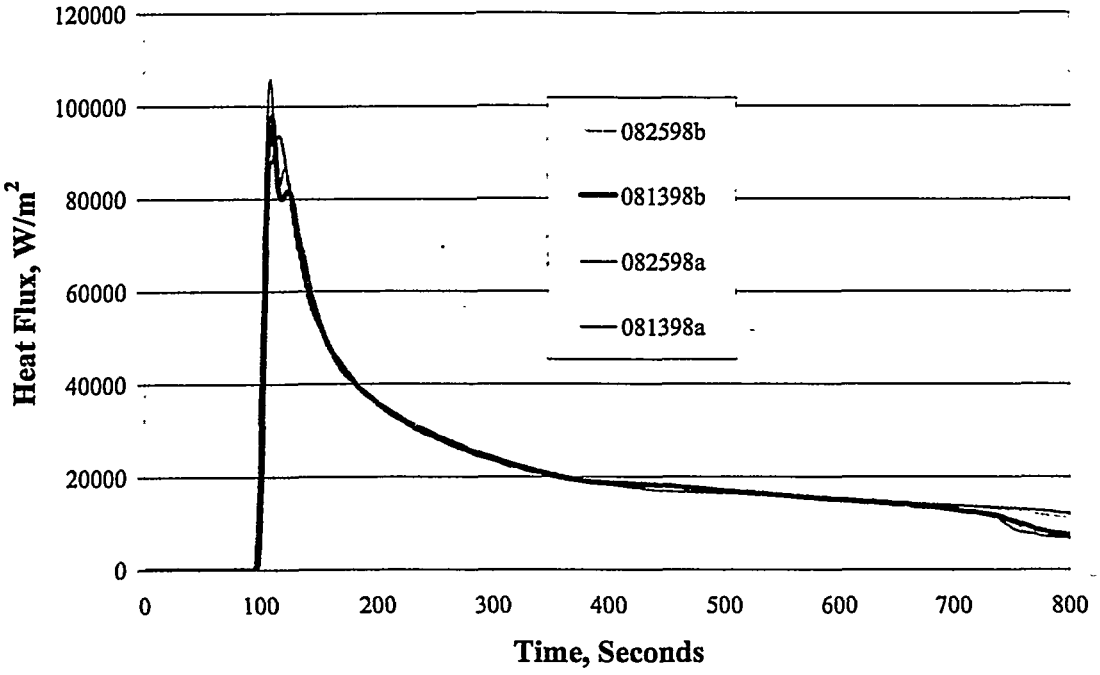

1.0" Horizontal Plates (Tops) 08/13/98 + 08/25/98